

TOWARDS THE MOLECULAR ORIGINS OF FRICTION AT ICE-I<sub>h</sub>/WATER  
INTERFACES

A Dissertation

Submitted to the Graduate School  
of the University of Notre Dame  
in Partial Fulfillment of the Requirements  
for the Degree of

Doctor of Philosophy

by  
Patrick B. Louden

---

J. Daniel Gezelter, Director

Graduate Program in Chemistry and Biochemistry

Notre Dame, Indiana

July 2017

© Copyright by

Patrick B. Louden

2017

All Rights Reserved

TOWARDS THE MOLECULAR ORIGINS OF FRICTION AT ICE-I<sub>h</sub>/WATER  
INTERFACES

Abstract

by

Patrick B. Louden

Here is where my abstract will go.

## CONTENTS

FIGURES . . . . .	iv
TABLES . . . . .	x
ACKNOWLEDGMENTS . . . . .	xi
CHAPTER 1: SIMULATIONS OF SOLID-LIQUID FRICTION AT ICE-I <sub>h</sub> /WATER INTERFACES . . . . .	
1.1 Introduction . . . . .	1
1.2 Methodology . . . . .	3
1.2.1 Stable ice I <sub>h</sub> / water interfaces under shear . . . . .	3
1.2.2 Shearing ice / water interfaces without bulk melting . . . . .	6
1.2.3 Computational Details . . . . .	8
1.3 Results and discussion . . . . .	9
1.3.1 Interfacial width . . . . .	9
1.3.1.1 Orientational Dynamics . . . . .	13
1.3.2 Coefficient of Friction of the Interface . . . . .	19
1.4 Conclusion . . . . .	23
CHAPTER 2: The different facets of ice have different hydrophilicities:	
Friction at water / ice-I <sub>h</sub> interfaces . . . . .	24
2.1 Introduction . . . . .	24
2.2 Methodology . . . . .	27
2.2.1 Construction of the Ice / Water interfaces . . . . .	27
2.3 Droplet Simulations . . . . .	28
2.4 Shearing Simulations (Interfaces in Bulk Water) . . . . .	29
2.5 Results . . . . .	31
2.5.1 Ice - Water Contact Angles . . . . .	31
2.5.2 Solid-liquid friction of the interfaces . . . . .	33
2.5.3 Structural measures of interfacial width under shear . . . . .	35
2.5.4 Dynamic measures of interfacial width under shear . . . . .	37
2.6 Conclusions . . . . .	38
2.7 The Advancing Contact Angle . . . . .	40
2.8 Interfacial widths using structural information . . . . .	42
2.9 Interfacial widths using dynamic information . . . . .	44

CHAPTER 3: Friction at ice-I <sub>h</sub> / water interfaces . . . . .	54
3.1 Introduction . . . . .	54
3.2 Methodology . . . . .	57
3.2.1 Construction of Ice / Water interfaces . . . . .	57
3.2.2 Creating shear in molecular simulations . . . . .	59
3.2.2.1 Shearing at ice / water interfaces . . . . .	60
3.3 Results . . . . .	61
3.3.1 Structural measures of interfacial width under shear . . . . .	61
3.3.2 Solid-liquid friction at ice/water interfaces . . . . .	67
3.3.3 Dynamic measures of interfacial width under shear . . . . .	71
3.4 Discussion . . . . .	76
3.4.0.1 Solid-liquid hydrogen bond density . . . . .	77
3.4.0.2 Surface corrugation . . . . .	78
3.5 Conclusions . . . . .	81
3.6 Fitting velocity profiles . . . . .	82
 APPENDIX A: A Single-Site Model for Water: Parameterized for the Reproduction of the Melting Point of Ice I <sub>h</sub> . . . . .	91
A.1 Introduction . . . . .	91
A.2 TIP1P/Ice . . . . .	95
A.2.1 Gas Phase Dimer . . . . .	95
A.2.1.1 Testing Electrostatic Cutoff . . . . .	97
A.2.1.2 Varying Lennard-Jones Parameters . . . . .	98
A.2.1.3 Varying Damping $\alpha$ . . . . .	100
A.2.1.4 Varing the Quadrupole: Introduction of Q <sub>xx</sub> . . . . .	101
A.2.2 TIP1P/Ice 2.0 . . . . .	106
A.2.3 Bulk Properties . . . . .	110
A.2.4 Basal Ice I <sub>h</sub> /water Coexistence . . . . .	111
 BIBLIOGRAPHY . . . . .	112

## FIGURES

1.1 The basal interface with a shear rate of $1.3 \text{ ms}^{-1}$ . Lower panel: the local tetrahedral order parameter, $q(z)$ , (black circles) and the hyperbolic tangent fit (red line). Middle panel: the imposed thermal gradient required to maintain a fixed interfacial temperature. Upper panel: the transverse velocity gradient that develops in response to an imposed momentum flux. The vertical dotted lines indicate the locations of the midpoints of the two interfaces. . . . .	11
1.2 The prismatic interface with a shear rate of $2.0 \text{ ms}^{-1}$ . Panel descriptions match those in figure 3.9 . . . . .	12
1.3 The width of the ice water interfaces (as measured by Eq. 3.3) exhibits no dependence on the applied shear rate between the ice and water regions. . . . .	14
1.4 The three decay constants of the orientational time correlation function, $C_2(t)$ , for water as a function of distance from the center of the ice slab. The dashed line indicates the location of the basal face (as determined from the tetrahedrality order parameter) and the black and red lines are fits of Eq. 3.9. The moderate and long time contributions slow down close to the interface which would be expected under reorganizations that involve large motions of the molecules (e.g. frame-reorientations and jumps). The observed speed-up in the short time contribution is surprising, but appears to reflect the restricted motion of librations closer to the interface. . . . .	16
1.5 Decay constants for $C_2(t)$ at the prismatic interface. Panel descriptions match those in figure 1.4. . . . .	17
1.6 Determining the (negative) slip length ( $\delta$ ) for the ice-water interfaces (which have decidedly non-slip behavior). This length is the difference between the structural edge of the ice (determined by the tetrahedrality profile) and the location where the projected velocity of the bulk liquid (dashed red line) intersects the solid phase velocity (solid black line). The dotted line indicates the location of the ice as determined by the tetrahedrality profile. This example is taken from the basal-face simulation with an applied shear rate of $3.0 \text{ ms}^{-1}$ . . . . .	22

2.1	Computational model of a droplet of liquid water spreading over the prismatic $\{10\bar{1}0\}$ facet of ice, before (left) and 2.6 ns after (right) being introduced to the surface. The contact angle ( $\theta$ ) shrinks as the simulation proceeds, and the long-time behavior of this angle is used to estimate the hydrophilicity of the facet. . . . .	40
2.2	Computational model of a slab of ice being sheared through liquid water. In this figure, the ice is presenting two copies of the prismatic $\{10\bar{1}0\}$ facet towards the liquid phase. The RNEMD simulation exchanges both linear momentum (indicated with arrows) and kinetic energy between the central box and the box that spans the cell boundary. The system responds with weak thermal gradient and a velocity profile that shears the ice relative to the surrounding liquid. . . . .	41
2.3	The dynamic contact angle of a droplet after approaching each of the four ice facets. The decay to an equilibrium contact angle displays similar dynamics. Although all the surfaces are hydrophilic, the long-time behavior stabilizes to significantly flatter droplets for the basal and pyramidal facets. This suggests a difference in hydrophilicity for these facets compared with the two prismatic facets. . . . .	45
2.4	Properties of the pyramidal interface being sheared through water at $3.8 \text{ ms}^{-1}$ . Lower panel: the local tetrahedral order parameter, $q(z)$ , (circles) and the hyperbolic tangent fit (turquoise line). Middle panel: the imposed thermal gradient required to maintain a fixed interfacial temperature of 225 K. Upper panel: the transverse velocity gradient that develops in response to an imposed momentum flux. The vertical dotted lines indicate the locations of the midpoints of the two interfaces.	46
2.5	The secondary prism interface with a shear rate of $3.5 \text{ ms}^{-1}$ . Panel descriptions match those in figure 3.8. . . . .	47
2.6	The basal interface with a shear rate of $1.3 \text{ ms}^{-1}$ . Panel descriptions match those in figure 3.8. . . . .	48
2.7	The prismatic interface with a shear rate of $2 \text{ ms}^{-1}$ . Panel descriptions match those in figure 3.8. . . . .	49
2.8	The three decay constants of the orientational time correlation function, $C_2(z, t)$ , for water as a function of distance from the center of the ice slab. The vertical dashed line indicates the edge of the pyramidal ice slab determined by the local order tetrahedral parameter. The control (circles) and sheared (squares) simulations were fit using shifted-exponential decay (see Eq. 9 in Ref. ? ). . . . .	50
2.9	Decay constants for $C_2(z, t)$ at the secondary prism face. Panel descriptions match those in 2.8. . . . .	51
2.10	Decay constants for $C_2(z, t)$ at the basal face. Panel descriptions match those in 2.8. . . . .	52

2.11 Decay constants for $C_2(z, t)$ at the prismatic face. Panel descriptions match those in 2.8. . . . .	53
3.1 In the hydrodynamic regime, the friction felt by a slider on an ice surface is mediated by a quasi-liquid layer (QLL) that forms on the surface of the ice. There can be many contributions to this friction: capillary bridges between the material and the QLL (red), viscous drag in the liquid (yellow), and solid-liquid friction between the ice and the liquid film (green). This study concerns the last of the three contributions, the drag contributed by the ice-liquid interface. . . . .	56
3.2 Computational model of a slab of ice being sheared through liquid water. The ice presents two copies of the prismatic $\{10\bar{1}0\}$ facet towards the liquid phase. The RNEMD simulation exchanges both linear momentum (indicated with arrows) and kinetic energy between the central box and the box that spans the cell boundary. The system responds with weak thermal gradient and a velocity profile that shears the ice relative to the surrounding liquid. . . . .	62
3.3 Properties of the secondary prism interface being sheared through water at $8.6 \text{ ms}^{-1}$ . Lower panel: the local tetrahedral order parameter, $q(z)$ , (circles) and the hyperbolic tangent fit (turquoise line). Middle panel: the imposed thermal gradient required to maintain a fixed interfacial temperature of 225 K. Upper panel: the transverse velocity gradient (squares) that develops in response to an imposed momentum flux, along with the fit (green line). The vertical dotted lines indicate the locations of the Gibbs dividing surfaces of the two interfaces. . . . .	65
3.4 Transverse velocity profiles, $v_x(z)$ , for interfaces in slip (top), no-slip (middle), and negative slip boundary conditions (bottom). The location of the interface is defined by a Gibbs dividing surface at $z_0$ . Under negative slip conditions, the 10-90 interfacial width, $w_{10-90}$ , provides locations that are unambiguously on the liquid and solid sides of the interface. . . . .	69
3.5 $C_2(z, t)$ collected in 1 Å bins across the secondary prism ice/water interface. The band that experiences very little decay represents water molecules in the ice, while the band that decays quickly corresponds to bins in the liquid. The correlation function presents a continuous distribution of decay behaviors across the interface between ice and liquid water. . . . .	73

3.6 Decay times (left) for $C_2(z, t)$ at the secondary prism interface, and their fractional contributions to the overall decay (right) fit using Eq. (3.8). The local decay constants are plotted as a function of distance from the center of the ice slab. The vertical dashed line indicates the Gibbs dividing surface determined using the local tetrahedral order parameter. Results are shown for a quiescent system with no applied kinetic or momentum flux (black), an interface with an imposed kinetic energy flux (red), and a sheared simulation (blue) with both kinetic and momentum fluxes. . . . .	75
3.7 Distribution of hydrogen bonds at a prismatic interface showing the tetrahedralities of donor ( $q_D$ ) and acceptor ( $q_A$ ) molecules (lower panel). Distributions of tetrahedralities in bulk ice and liquid phases are shown in the upper panel, and the value of $q$ at the Gibbs dividing surface is indicated with dashed lines. Hydrogen bonds between ice molecules are represented by the upper right square, while those between liquid molecules are in the lower left. Hydrogen bonds that bridge the ice-liquid interface exist primarily in the vertical and horizontal strips that remain. . . . .	79
3.8 Properties of the pyramidal interface being sheared through water at $7.6 \text{ ms}^{-1}$ . Lower panel: the local tetrahedral order parameter, $q(z)$ , (circles) and the hyperbolic tangent fit (turquoise line). Middle panel: the imposed thermal gradient required to maintain a fixed interfacial temperature of 225 K. Upper panel: the transverse velocity gradient (squares) that develops in response to an imposed momentum flux, along with the fit (green line). The vertical dotted lines indicate the locations of the Gibbs dividing surfaces of the two interfaces. . . . .	84
3.9 Properties of the basal interface being sheared through water at $3.2 \text{ ms}^{-1}$ . Panel descriptions are the same as in Fig. 3.8. . . . .	85
3.10 Properties of the prismatic interface being sheared through water at $6.0 \text{ ms}^{-1}$ . Panel descriptions are the same as in Fig. 3.8. . . . .	86
3.11 Decay times (left) for $C_2(z, t)$ at the pyramidal interface, and their fractional contributions to the overall decay (right) fit using Eq. (8). The local decay constants are plotted as a function of distance from the center of the ice slab. The vertical dashed line indicates the Gibbs dividing surface determined using the local tetrahedral order parameter. Results are shown for a quiescent system with no applied kinetic or momentum flux (black), an interface with with an imposed kinetic energy flux (red), and a sheared simulation (blue) with both kinetic and momentum fluxes. . . . .	87
3.12 $C_2(z, t)$ time constants for the basal interface. Panel descriptions are the same as in Fig. 3.11. . . . .	88

3.13	$C_2(z, t)$ time constants for the prismatic interface. Panel descriptions are the same as in Fig. 3.11.	89
3.14	Solid-liquid friction coefficients by the surface density of hydrogen bonds. Linear regression gives a slope of 2.1772 (amu fs <sup>-1</sup> ) and a y-intercept of 0.0777 (amu Å <sup>-2</sup> fs <sup>-1</sup> ).	90
A.1	Melting point for ice I <sub>h</sub> of several popular water models as a function of the QBar for the model. We see a strong correlation between a more accurate melting point and a larger value of QBar. We estimate that a QBar of approximately 2.8 DÅ will result in the experimental melting point of 273.15 K. A linear regression of the data resulted in an equation of best fit of $y = 158.89x - 166.83$ . From this, we have predicted an optimal QBar to be 2.7690 DÅ.	94
A.2	Melting point for ice I <sub>h</sub> of several popular water models as a function of the trace of the quadrupole tensor for the model. We see a strong correlation between a more accurate melting point and a larger value of the trace. We estimate that a trace of approximately 2.3 DÅ will result in the experimental melting point of 273.15 K.	95
A.3	The gas phase water dimer geometry.	97
A.4	Damping $\alpha$ set to 0.05 Å <sup>-1</sup> and the simulation box was 300 × 300 × 300 Å.	98
A.5	The Lennard-Jones parameter $\sigma$ was varied while holding the other parameters of the TIP1P/Ice model constant.	99
A.6	The Lennard-Jones parameter $\epsilon$ was varied while holding the other parameters of the TIP1P/Ice model constant.	100
A.7	Damping $\alpha$ was varied while holding the other parameters of the TIP1P/Ice model constant.	101
A.8	The Q <sub>xx</sub> components of the traced quadrupole tensor were varied while simultaneously adjusting the Q <sub>yy</sub> component such that the Q <sub>T</sub> value for the TIP1P/Ice model was held constant. All other parameters were also held constant and equal to the TIP1P/Ice parameters during this test. This means that Tr(Q) varied since the Q <sub>zz</sub> component was not adjusted as Q <sub>xx</sub> was varied.	102
A.9	The same data as plotted in Figure A.8, now plotted as a function of the TrQ.	103
A.10	The Q <sub>xx</sub> components of the traced quadrupole tensor were varied while simultaneously adjusting the Q <sub>yy</sub> component such that the Q <sub>T</sub> value for the TIP1P/Ice model was held constant. The Q <sub>zz</sub> component of the quadrupole tensor was also varied in such a way as to keep the Tr(Q) held constant to the TIP1P/Ice value. We see here that the angles cross over one another as in Figure A.8.	104

A.11 Setting $\sigma$ to 3.2668 Å , vary $Q_{xx}$ while simultanesouly adjusting $Q_{yy}$ and $Q_{zz}$ to conserve $Q_T$ and $TrQ$ . . . . .	104
A.12 Setting $\sigma$ to 3.2268 Å , vary $Q_{xx}$ while simultaneously adjusting $Q_{yy}$ and $Q_{zz}$ to conserve $Q_T$ and $TrQ$ . . . . .	105
A.13 Here $Q_{xx}$ and $Q_{yy}$ are varied simulatneously to conserve the value of $Q_T$ . $\mu$ is scaled as $0.996Q_T$ , thus the ratio of $\mu$ to $Q_T$ is conserved for each Test of $Q_T$ . The $TrQ$ is fixed to a set value, thus $Q_{zz}$ varies as the other components do. . . . .	105
A.14 . . . . .	106
A.15 $Q_{xx} = -0.1$ , QBar set to the TIP4P/Ice QBar value of 2.8141, $Q_{zz}$ was modified to keep this constant as $Q_{yy}$ changed. . . . .	107
A.16 $Q_{yy} = -0.1$ , $Q_{zz}$ was varied to keep QBar constant and equal to the TIP4P/Ice model's value of 2.8141. . . . .	108
A.17 $Q_{xx}$ and $Q_{yy}$ varied while holding $Q_T$ constant, $Q_{zz}$ varied in order to keep $TrQ$ constant. Both $Q_T$ and $TrQ$ were set to the TIP4P/Ice model value. . . . .	108
A.18 $Q_{xx} = -0.1$ , $Q_{yy} = -0.1$ , $Q_{zz} = 1.3701$ which ensures QBar is set to the TIP4P/Ice model value of 2.8141 DÅ . . . . .	109
A.19 $Q_{xx}$ and $Q_{zz}$ are set to the TIP4P/Ice value, as well as the Lennard-Jones parameters.The left most data point is the parameter set of the TIP4P/Ice model. . . . .	109
A.20 $Q_{yy}$ and $Q_{zz}$ are set to the TIP4P/Ice value,as well as the Lennard-Jones parameters.The left most data point is the parameter set of the TIP4P/Ice model. . . . .	110
A.21 $Q_{xx}$ and $Q_{yy}$ are set to the TIP4P/Ice value, as well as the Lennard-Jones parameters.The left most data point is the parameter set of the TIP4P/Ice model. . . . .	111

## TABLES

1.1	Mapping between the Miller indices of four facets of ice in the $P6_3/mmc$ crystal system to the orthorhombic $P2_12_12_1$ system in reference ? . . . . .	3
1.2	Fractional coordinates for water in the orthorhombic $P2_12_12_1$ system for ice $I_h$ in reference ? . . . . .	5
1.3	Solid-liquid friction coefficients (measured in amu fs <sup>-1</sup> ) . . . . .	21
2.1	Sizes of the droplet and shearing simulations. Cell dimensions are measured in Å. . . . .	42
2.2	Structural and dynamic properties of the interfaces of Ice- $I_h$ with water. . . . .	43
3.1	Sizes of the ice/water shearing simulations. . . . .	59
3.2	Structural and dynamic properties of the interfaces of Ice- $I_h$ with water. . . . .	67
3.3	Surface features of Ice- $I_h$ facets. . . . .	80
A.1	Traced quadrupole tensors for the water models investigated by Abasca and Vega. All elements of the tensors are in units of DÅ , melting temperatures are reported in Kelvin. . . . .	93
A.2	Geometric parameters of the TIP4P/Ice and TIP1P/Ice models. . . . .	96
A.3	Lennard-Jones and charge parameters of the TIP4P/Ice and TIP1P/Ice models. . . . .	96
A.4	Dipole and quadrupole parameters for the TIP4P/Ice and TIP1P/Ice models. . . . .	96
A.5	Geometric parameters of the TIP4P/Ice and TIP1P/Ice gas phase wa- ter dimer. Ab initio and Expt. values were taken from another source? . . . . .	98

## ACKNOWLEDGMENTS

So many thanks, much wow.

## CHAPTER 1

### SIMULATIONS OF SOLID-LIQUID FRICTION AT ICE-I<sub>h</sub> /WATER INTERFACES

We have investigated the structural and dynamic properties of the basal and prismatic facets of the ice I<sub>h</sub> / water interface when the solid phase is drawn through the liquid (i.e. sheared relative to the fluid phase). To impose the shear, we utilized a velocity-shearing and scaling (VSS) approach to reverse non-equilibrium molecular dynamics (RNEMD). This method can create simultaneous temperature and velocity gradients and allow the measurement of transport properties at interfaces. The interfacial width was found to be independent of the relative velocity of the ice and liquid layers over a wide range of shear rates. Decays of molecular orientational time correlation functions gave similar estimates for the width of the interfaces, although the short- and longer-time decay components behave differently closer to the interface. Although both facets of ice are in “stick” boundary conditions in liquid water, the solid-liquid friction coefficients were found to be significantly different for the basal and prismatic facets of ice.

#### 1.1 Introduction

Understanding the ice/water interface is essential for explaining complex processes such as nucleation and crystal growth,<sup>?</sup> ? ? ? crystal melting,<sup>?</sup> ? ? ? and some fascinating biological processes, such as the behavior of the antifreeze proteins found in winter flounder,<sup>?</sup> ? and certain terrestrial arthropods.<sup>?</sup> ? There has been significant progress on understanding the structure and dynamics of quiescent

ice/water interfaces utilizing both theory and experiment. Haymet *et al.* have done extensive work on ice I<sub>h</sub>, including characterizing and determining the width of the ice/water interface for the SPC,<sup>?</sup> SPC/E,<sup>?</sup> CF1,<sup>?</sup> and TIP4P<sup>?</sup> models for water. More recently, Haymet *et al.* have investigated the effects cations and anions have on crystal nucleation.<sup>?</sup> Nada *et al.* have also studied ice/water interfaces,<sup>?</sup> and have found that the differential growth rates of the facets of ice I<sub>h</sub> are due to the the reordering of the hydrogen bonding network.<sup>?</sup>

The movement of liquid water over the facets of ice has been less thoroughly studied than the quiescent surfaces. This process is potentially important in understanding transport of large blocks of ice in water (which has important implications in the earth sciences), as well as the relative motion of crystal-crystal interfaces that have been separated by nanometer-scale fluid domains. In addition to understanding both the structure and thickness of the interfacial regions, it is important to understand the molecular origin of friction, drag, and other changes in dynamical properties of the liquid in the regions close to the surface that are altered by the presence of a shearing of the bulk fluid relative to the solid phase.

In this work, we apply a recently-developed velocity shearing and scaling approach to reverse non-equilibrium molecular dynamics (VSS-RNEMD). This method makes it possible to calculate transport properties like the interfacial thermal conductance across heterogeneous interfaces,<sup>?</sup> and can create simultaneous temperature and velocity gradients and allow the measurement of friction and thermal transport properties at interfaces. This has allowed us to investigate the width of the ice/water interface as the ice is sheared through the liquid, while simultaneously imposing a weak thermal gradient to prevent frictional heating of the interface. In the sections that follow, we discuss the methodology for creating and simulating ice/water interfaces under shear and provide results from both structural and dynamical correlation functions. We also show that the solid-liquid interfacial friction coefficient depends

sensitively on the details of the surface morphology.

## 1.2 Methodology

### 1.2.1 Stable ice I<sub>h</sub> / water interfaces under shear

The structure of ice I<sub>h</sub> is well understood; it crystallizes in a hexagonal space group P6<sub>3</sub>/mmc, and the hexagonal crystals of ice have two faces that are commonly exposed, the basal face {0 0 0 1}, which forms the top and bottom of each hexagonal plate, and the prismatic {1 0 1 0} face which forms the sides of the plate. Other less-common, but still important, faces of ice I<sub>h</sub> are the secondary prism, {1 1 2 0}, and pyramidal, {2 0 2 1}, faces. Ice I<sub>h</sub> is normally proton disordered in bulk crystals, although the surfaces probably have a preference for proton ordering along strips of dangling H-atoms and Oxygen lone pairs.?

TABLE 1.1

Mapping between the Miller indices of four facets of ice in the *P*6<sub>3</sub>/mmc crystal system to the orthorhombic *P*2<sub>1</sub>2<sub>1</sub>2<sub>1</sub> system in reference ? .

crystal face	hexagonal (P6 <sub>3</sub> /mmc)	orthorhombic (P2 <sub>1</sub> 2 <sub>1</sub> 2 <sub>1</sub> )
	Miller indices	equivalent
basal	{0 0 0 1}	{0 0 1}
prism	{1 0 1 0}	{1 0 0}
secondary prism	{1 1 2 0}	{1 3 0}
pyramidal	{2 0 2 1}	{2 0 1}

For small simulated ice interfaces, it is useful to work with proton-ordered, but zero-dipole crystal that exposes these strips of dangling H-atoms and lone pairs. When placing another material in contact with one of the ice crystalline planes, it is also quite useful to have an orthorhombic (rectangular) box. Recent work by Hirsch and Ojamäe describes a number of alternative crystal systems for proton-ordered bulk ice I<sub>h</sub> using orthorhombic cells.?

In this work, we are using Hirsch and Ojamäe's structure 6 which is an orthorhombic cell ( $P2_12_12_1$ ) that produces a proton-ordered version of ice I<sub>h</sub>. Table 1.1 contains a mapping between the Miller indices of common ice facets in the P6<sub>3</sub>/mmc crystal system and those in the Hirsch and Ojamäe  $P2_12_12_1$  system.

Structure 6 from the Hirsch and Ojam  e paper has lattice parameters  $a = 4.49225$    ,  $b = 7.78080$    ,  $c = 7.33581$     and two water molecules whose atoms reside at fractional coordinates given in table 1.2. To construct the basal and prismatic interfaces, these crystallographic coordinates were used to construct an orthorhombic unit cell which was then replicated in all three dimensions yielding a proton-ordered block of ice I<sub>h</sub>. To expose the desired face, the orthorhombic representation was then cut along the (001) or (100) planes for the basal and prismatic faces respectively. The resulting block was rotated so that the exposed faces were aligned with the  $z$ -axis normal to the exposed face. The block was then cut along two perpendicular directions in a way that allowed for perfect periodic replication in the  $x$  and  $y$  axes, creating a slab with either the basal or prismatic faces exposed along the  $z$  axis. The slab was then replicated in the  $x$  and  $y$  dimensions until a desired sample size was obtained.

Our ice / water interfaces were created using a box of liquid water that had the same dimensions (in  $x$  and  $y$ ) as the ice block. Although the experimental solid/liquid coexistence temperature under atmospheric pressure is close to 273 K, Haymet *et al.*

TABLE 1.2

Fractional coordinates for water in the orthorhombic  $P2_12_12_1$  system for ice  
 $I_h$  in reference ? .

atom type	x	y	z
O	0.7500	0.1667	0.4375
H	0.5735	0.2202	0.4836
H	0.7420	0.0517	0.4836
O	0.2500	0.6667	0.4375
H	0.2580	0.6693	0.3071
H	0.4265	0.7255	0.4756

have done extensive work on characterizing the ice/water interface, and find that the coexistence temperature for simulated water is often quite a bit different.? ? ? ? ? They have found that for the SPC/E water model,? which is also used in this study, the ice/water interface is most stable at  $225 \pm 5$  K.? This liquid box was therefore equilibrated at 225 K and 1 atm of pressure in the NPAT ensemble (with the  $z$  axis allowed to fluctuate to equilibrate to the correct pressure). The liquid and solid systems were combined by carving out any water molecule from the liquid simulation cell that was within 3 Å of any atom in the ice slab. The resulting basal system was  $23.87 \times 35.83 \times 98.64$  Å with 900 SPC/E molecules in the ice slab, and 1846 in the liquid phase. Similarly, the prismatic system was  $36.12 \times 36.43 \times 86.10$  Å with 1000 SPC/E molecules in the ice slab and 2684 in the liquid.

Molecular translation and orientational restraints were applied in the early stages of equilibration to prevent melting of the ice slab. These restraints were removed during NVT equilibration, well before data collection was carried out.

### 1.2.2 Shearing ice / water interfaces without bulk melting

As a solid is dragged through a liquid, there is frictional heating that will act to melt the interface. To study the behavior of the interface under a shear stress without causing the interface to melt, it is necessary to apply a weak thermal gradient in combination with the momentum gradient. This can be accomplished using the velocity shearing and scaling (VSS) variant of reverse non-equilibrium molecular dynamics (RNEMD), which utilizes a series of simultaneous velocity exchanges between two regions within the simulation cell.<sup>?</sup> One of these regions is centered within the ice slab, while the other is centrally located in the liquid region. VSS-RNEMD provides a set of conservation constraints for creating either a momentum flux or a thermal flux (or both simultaneously) between the two slabs. Satisfying the constraint equations ensures that the new configurations are sampled from the same NVE ensemble as before the VSS move.

The VSS moves are applied periodically to scale and shift the particle velocities ( $\mathbf{v}_i$  and  $\mathbf{v}_j$ ) in two slabs ( $H$  and  $C$ ) which are separated by half of the simulation box,

$$\begin{array}{rcccl} & \text{shearing} & & \text{scaling} & \\ \hline \mathbf{v}_i & \leftarrow & \mathbf{a}_c & + & c \cdot (\mathbf{v}_i - \langle \mathbf{v}_c \rangle) + \langle \mathbf{v}_c \rangle \\ \mathbf{v}_j & \leftarrow & \mathbf{a}_h & + & h \cdot (\mathbf{v}_j - \langle \mathbf{v}_h \rangle) + \langle \mathbf{v}_h \rangle. \end{array}$$

Here  $\langle \mathbf{v}_c \rangle$  and  $\langle \mathbf{v}_h \rangle$  are the center of mass velocities in the  $C$  and  $H$  slabs, respectively. Within the two slabs, particles receive incremental changes or a “shear” to their velocities. The amount of shear is governed by the imposed momentum flux,  $\mathbf{j}_z(\mathbf{p})$

$$\mathbf{a}_c = -\mathbf{j}_z(\mathbf{p})\Delta t/M_c \quad (1.1)$$

$$\mathbf{a}_h = +\mathbf{j}_z(\mathbf{p})\Delta t/M_h \quad (1.2)$$

where  $M_{\{c,h\}}$  is the total mass of particles within each of the slabs and  $\Delta t$  is the

interval between two separate operations.

To simultaneously impose a thermal flux ( $J_z$ ) between the slabs we use energy conservation constraints,

$$K_c - J_z \Delta t = c^2(K_c - \frac{1}{2}M_c\langle \mathbf{v}_c \rangle^2) + \frac{1}{2}M_c(\langle \mathbf{v}_c \rangle + \mathbf{a}_c)^2 \quad (1.3)$$

$$K_h + J_z \Delta t = h^2(K_h - \frac{1}{2}M_h\langle \mathbf{v}_h \rangle^2) + \frac{1}{2}M_h(\langle \mathbf{v}_h \rangle + \mathbf{a}_h)^2. \quad (1.4)$$

Simultaneous solution of these quadratic formulae for the scaling coefficients,  $c$  and  $h$ , will ensure that the simulation samples from the original microcanonical (NVE) ensemble. Here  $K_{\{c,h\}}$  is the instantaneous translational kinetic energy of each slab. At each time interval, it is a simple matter to solve for  $c$ ,  $h$ ,  $\mathbf{a}_c$ , and  $\mathbf{a}_h$ , subject to the imposed momentum flux,  $j_z(\mathbf{p})$ , and thermal flux,  $J_z$ , values. Since the VSS operations do not change the kinetic energy due to orientational degrees of freedom or the potential energy of a system, configurations after the VSS move have exactly the same energy (and linear momentum) as before the move.

As the simulation progresses, the VSS moves are performed on a regular basis, and the system develops a thermal and/or velocity gradient in response to the applied flux. In a bulk material, it is quite simple to use the slope of the temperature or velocity gradients to obtain either the thermal conductivity or shear viscosity.

The VSS-RNEMD approach is versatile in that it may be used to implement thermal and shear transport simultaneously. Perturbations of velocities away from the ideal Maxwell-Boltzmann distributions are minimal, as is thermal anisotropy. This ability to generate simultaneous thermal and shear fluxes has been previously utilized to map out the shear viscosity of SPC/E water over a wide range of temperatures (90 K) with a single 1 ns simulation.?

For this work, we are using the VSS-RNEMD method primarily to generate a shear between the ice slab and the liquid phase, while using a weak thermal gradient

to maintain the interface at the 225 K target value. This ensures minimal melting of the bulk ice phase and allows us to control the exact temperature of the interface.

### 1.2.3 Computational Details

All simulations were performed using OpenMD,<sup>7</sup> with a time step of 2 fs and periodic boundary conditions in all three dimensions. Electrostatics were handled using the damped-shifted force real-space electrostatic kernel.<sup>8</sup> The systems were divided into 100 bins along the  $z$ -axis for the VSS-RNEMD moves, which were attempted every 50 fs.

The interfaces were equilibrated for a total of 10 ns at equilibrium conditions before being exposed to either a shear or thermal gradient. This consisted of 5 ns under a constant temperature (NVT) integrator set to 225K followed by 5 ns under a microcanonical integrator. Weak thermal gradients were allowed to develop using the VSS-RNEMD (NVE) integrator using a small thermal flux ( $-2.0 \times 10^{-6}$  kcal/mol/Å<sup>2</sup>/fs) for a duration of 5 ns to allow the gradient to stabilize. The resulting temperature gradient was  $\approx 10$ K over the entire 100 Å box length, which was sufficient to keep the temperature at the interface within  $\pm 1$  K of the 225K target.

Velocity gradients were then imposed using the VSS-RNEMD (NVE) integrator with a range of momentum fluxes. These gradients were allowed to stabilize for 1 ns before data collection began. Once established, four successive 0.5 ns runs were performed for each shear rate. During these simulations, snapshots of the system were taken every 1 ps, and statistics on the structure and dynamics in each bin were accumulated throughout the simulations. Although there was some small variation in the measured interfacial width between successive runs, no indication of bulk melting (or crystallization) was observed.

## 1.3 Results and discussion

### 1.3.1 Interfacial width

Any order parameter or time correlation function that changes as one crosses an interface from a bulk liquid to a solid can be used to measure the width of the interface. In previous work on the ice/water interface, Haymet *et al.*? have utilized structural features (including the density) as well as dynamic properties (including the diffusion constant) to estimate the width of the interfaces for a number of facets of the ice crystals. Because VSS-RNEMD imposes a lateral flow, parameters that depend on translational motion of the molecules (e.g. diffusion) may be artificially skewed by the RNEMD moves. A structural parameter is not influenced by the RNEMD perturbations to the same degree. Here, we have used the local tetrahedral order parameter as described by Kumar? and Errington? as our principal measure of the interfacial width. A previous study by Bryk and Haymet also used local tetrahedrality as an order parameter for ice/water interfaces.?

The local tetrahedral order parameter,  $q(z)$ , is given by

$$q(z) = \int_0^L \sum_{k=1}^N \left( 1 - \frac{3}{8} \sum_{i=1}^3 \sum_{j=i+1}^4 \left( \cos \psi_{ikj} + \frac{1}{3} \right)^2 \right) \delta(z_k - z) dz / N_z \quad (1.5)$$

where  $\psi_{ikj}$  is the angle formed between the oxygen site on central molecule  $k$ , and the oxygen sites on two of the four closest molecules,  $i$  and  $j$ . Molecules  $i$  and  $j$  are further restricted to lie within the first peak in the pair distribution function for molecule  $k$  (typically  $< 3.41$  Å for water).  $N_z = \int \delta(z_k - z) dz$  is a normalization factor to account for the varying population of molecules within each finite-width bin. The local tetrahedral order parameter has a range of  $(0, 1)$ , where the larger values of  $q$  indicate a larger degree of tetrahedral ordering of the local environment. In perfect ice I<sub>h</sub> structures, the parameter can approach 1 at low temperatures, while in liquid water, the ordering is significantly less tetrahedral, and values of  $q(z) \approx 0.75$

are more common.

To estimate the interfacial width, the system was divided into 100 bins along the  $z$ -dimension. The  $q_z$  function was time-averaged to give yield a tetrahedrality profile of the system. The profile was then fit to a hyperbolic tangent that smoothly links the liquid and solid states,

$$q(z) \approx q_{liq} + \frac{q_{ice} - q_{liq}}{2} \left[ \tanh\left(\frac{z-l}{w}\right) - \tanh\left(\frac{z-r}{w}\right) \right] + \beta \left| z - \frac{r+l}{2} \right|. \quad (1.6)$$

Here  $q_{liq}$  and  $q_{ice}$  are the local tetrahedral order parameter for the bulk liquid and ice domains, respectively,  $w$  is the width of the interface.  $l$  and  $r$  are the midpoints of the left and right interfaces, respectively. The last term in eq. (3.3) accounts for the influence that the weak thermal gradient has on the tetrahedrality profile in the liquid region.

In Figures 3.9 and 3.10 we see the  $z$ -coordinate profiles for tetrahedrality, temperature, and the  $x$ -component of the velocity for the basal and prismatic interfaces. The lower panels show the  $q(z)$  (black circles) along with the hyperbolic tangent fits (red lines). In the liquid region, the local tetrahedral order parameter,  $q(z) \approx 0.75$  while in the crystalline region,  $q(z) \approx 0.94$ , indicating a more tetrahedral environment. The vertical dotted lines denote the midpoint of the interfaces ( $r$  and  $l$  in eq. (3.3)). The weak thermal gradient applied to the systems in order to keep the interface at  $225 \pm 5$ K, can be seen in middle panels. The transverse velocity profile is shown in the upper panels. It is clear from the upper panels that water molecules in close proximity to the surface (i.e. within 10 Å to 15 Å of the interfaces) have transverse velocities quite close to the velocities within the ice block. There is no velocity discontinuity at the interface, which indicates that the shearing of ice/water interfaces occurs in the “stick” or no-slip boundary conditions.

From the fits using eq. (3.3), we find the interfacial width for the basal and

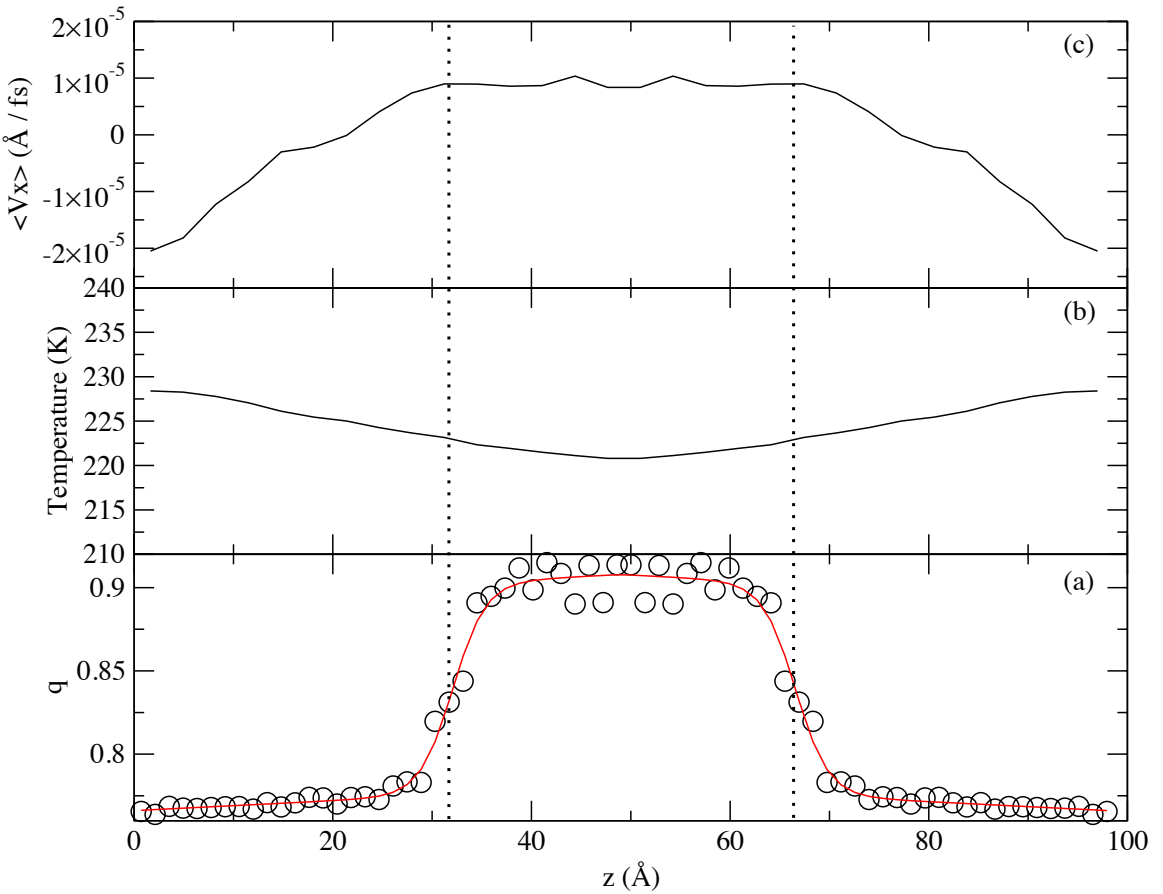


Figure 1.1. The basal interface with a shear rate of  $1.3 \text{ ms}^{-1}$ . Lower panel: the local tetrahedral order parameter,  $q(z)$ , (black circles) and the hyperbolic tangent fit (red line). Middle panel: the imposed thermal gradient required to maintain a fixed interfacial temperature. Upper panel: the transverse velocity gradient that develops in response to an imposed momentum flux. The vertical dotted lines indicate the locations of the midpoints of the two interfaces.

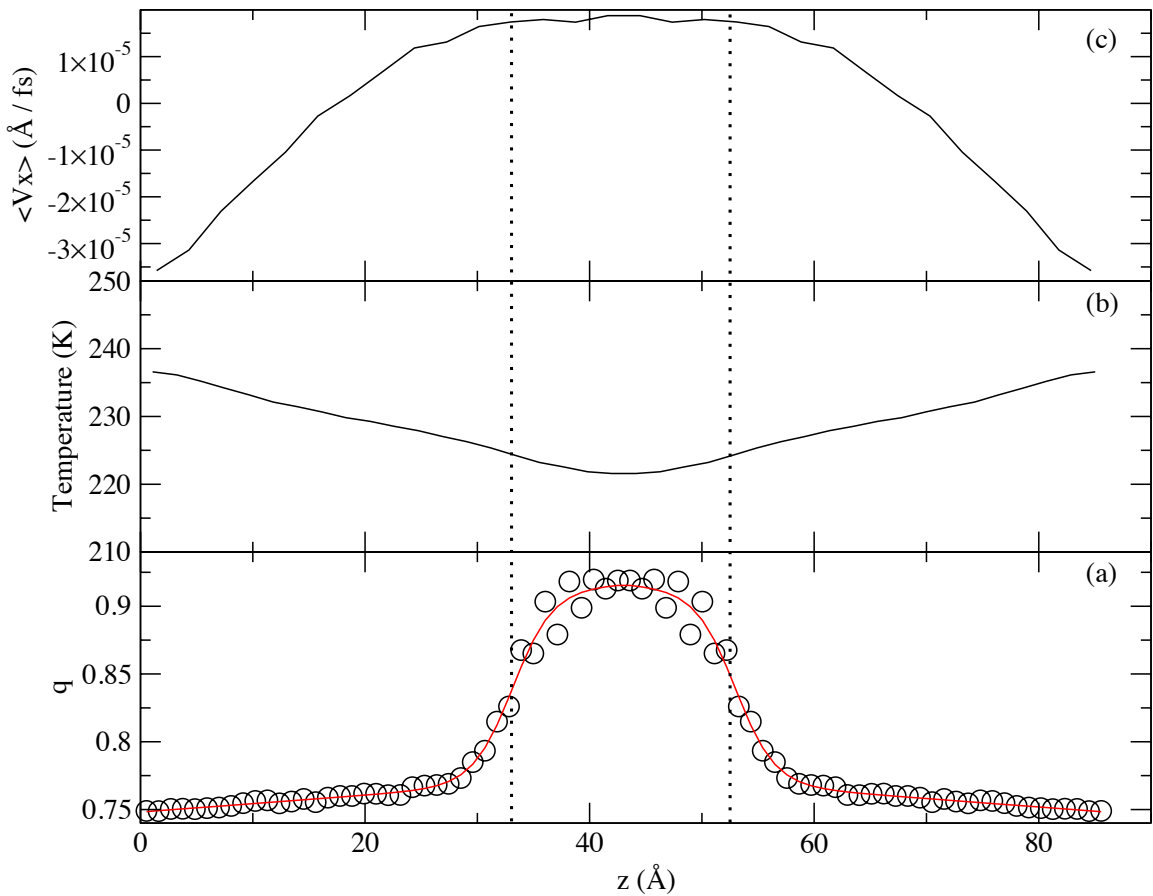


Figure 1.2. The prismatic interface with a shear rate of  $2.0 \text{ ms}^{-1}$ . Panel descriptions match those in figure 3.9

prismatic systems to be  $3.2 \pm 0.4$  Å and  $3.6 \pm 0.2$  Å , respectively, with no applied momentum flux. Over the range of shear rates investigated,  $0.6 \pm 0.3\text{ms}^{-1} \rightarrow 5.3 \pm 0.5\text{ms}^{-1}$  for the basal system and  $0.9 \pm 0.2\text{ms}^{-1} \rightarrow 4.5 \pm 0.1\text{ms}^{-1}$  for the prismatic, we found no appreciable change in the interface width. The fit values for the interfacial width ( $w$ ) over all shear rates contained the values reported above within their error bars. Note that the interfacial widths reported here are based on the hyperbolic tangent parameter  $w$  in Eq. 3.3. This is related to, but not identical with, the 10%-90% intefacial widths commonly used in previous studies.<sup>?</sup> ? To estimate the 10%-90% widths, it is a simple matter to scale the widths obtained from the hyperbolic tangent fits to obtain  $w_{10-90} = 2.1971 \times w$ .<sup>?</sup> ? This results in  $w_{10-90}$  values of  $7.0 \pm 0.9$  Å for the basal face, and  $7.9 \pm 0.4$  Å for the prismatic face. These are somewhat smaller than previously reported values.

### 1.3.1.1 Orientational Dynamics

The orientational time correlation function,

$$C_2(t) = \langle P_2(\mathbf{u}(0) \cdot \mathbf{u}(t)) \rangle, \quad (1.7)$$

gives insight into the local dynamic environment around the water molecules. The rate at which the function decays provides information about hindered motions and the timescales for relaxation. In eq. (3.7),  $P_2$  is the second-order Legendre polynomial, the vector  $\mathbf{u}$  is often taken as HOH bisector, although slightly different behavior can be observed when  $\mathbf{u}$  is the vector along one of the OH bonds. The angle brackets denote an ensemble average over all water molecules in a given spatial region.

To investigate the dynamic behavior of water at the ice interfaces, we have computed  $C_2(z, t)$  for molecules that are present within a particular slab along the  $z$ -axis at the initial time. The change in the decay behavior as a function of the  $z$

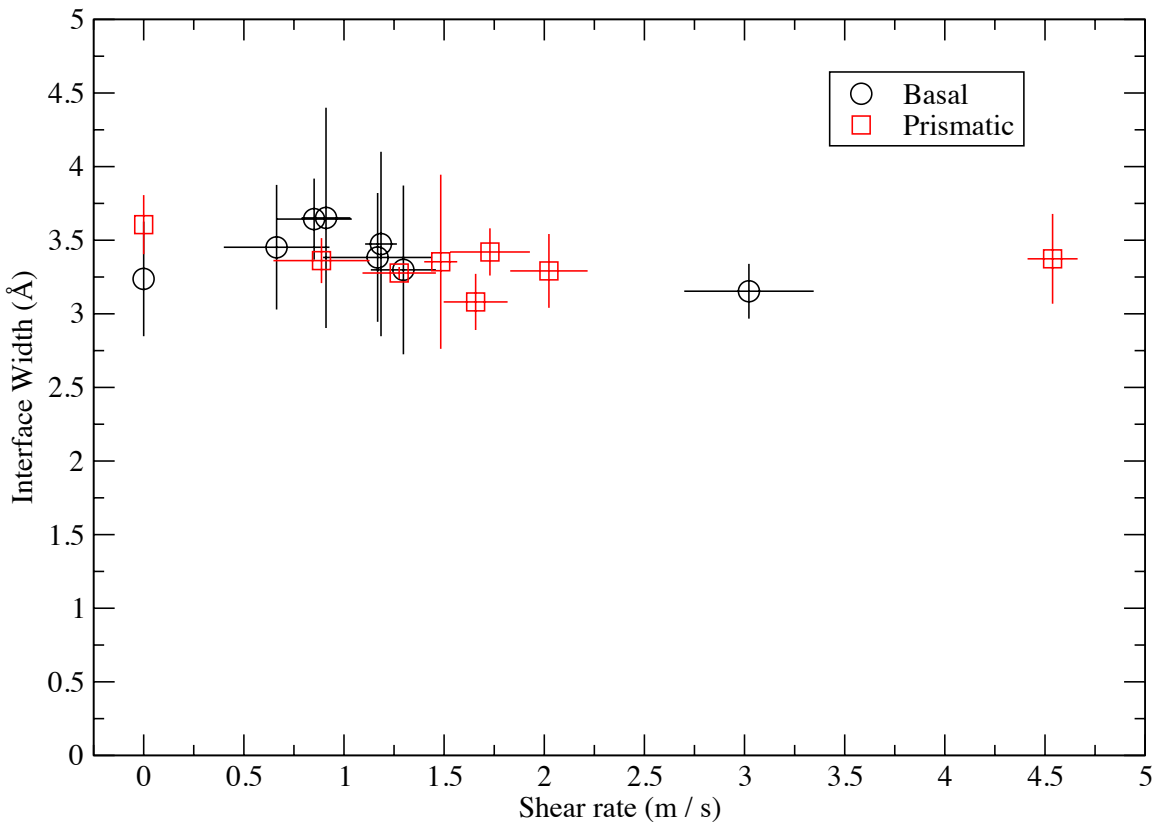


Figure 1.3. The width of the ice water interfaces (as measured by Eq. 3.3) exhibits no dependence on the applied shear rate between the ice and water regions.

coordinate is another measure of the change of how the local environment changes across the ice/water interface. To compute these correlation functions, each of the 0.5 ns simulations was followed by a shorter 200 ps microcanonical (NVE) simulation in which the positions and orientations of every molecule in the system were recorded every 0.1 ps. The systems were then divided into 30 bins along the  $z$ -axis and  $C_2(t)$  was evaluated for each bin.

In simulations of water at biological interfaces, Furse *et al.* fit  $C_2(t)$  functions for water with triexponential functions,<sup>?</sup> where the three components of the decay correspond to a fast (<200 fs) reorientational piece driven by the restoring forces of existing hydrogen bonds, a middle (on the order of several ps) piece describing the large angle jumps that occur during the breaking and formation of new hydrogen bonds, and a slow (on the order of tens of ps) contribution describing the translational motion of the molecules. The model for orientational decay presented recently by Laage and Hynes *et al.*<sup>?</sup> also includes three similar decay constants, although two of the time constants are linked, and the resulting decay curve has two parameters governing the dynamics of decay.

In our ice/water interfaces, we are at substantially lower temperatures, and the water molecules are further perturbed by the presence of the ice phase nearby. We have obtained the most reasonable fits using triexponential functions with three distinct time domains, as well as a constant piece to account for the water stuck in the ice phase that does not experience any long-time orientational decay,

$$C_2(t) \approx ae^{-t/\tau_{\text{short}}} + be^{-t/\tau_{\text{middle}}} + ce^{-t/\tau_{\text{long}}} + (1 - a - b - c) \quad (1.8)$$

Average values for the three decay constants (and error estimates) were obtained for each bin. In figures 1.4 and 1.5, the three orientational decay times are shown as a function of distance from the center of the ice slab.

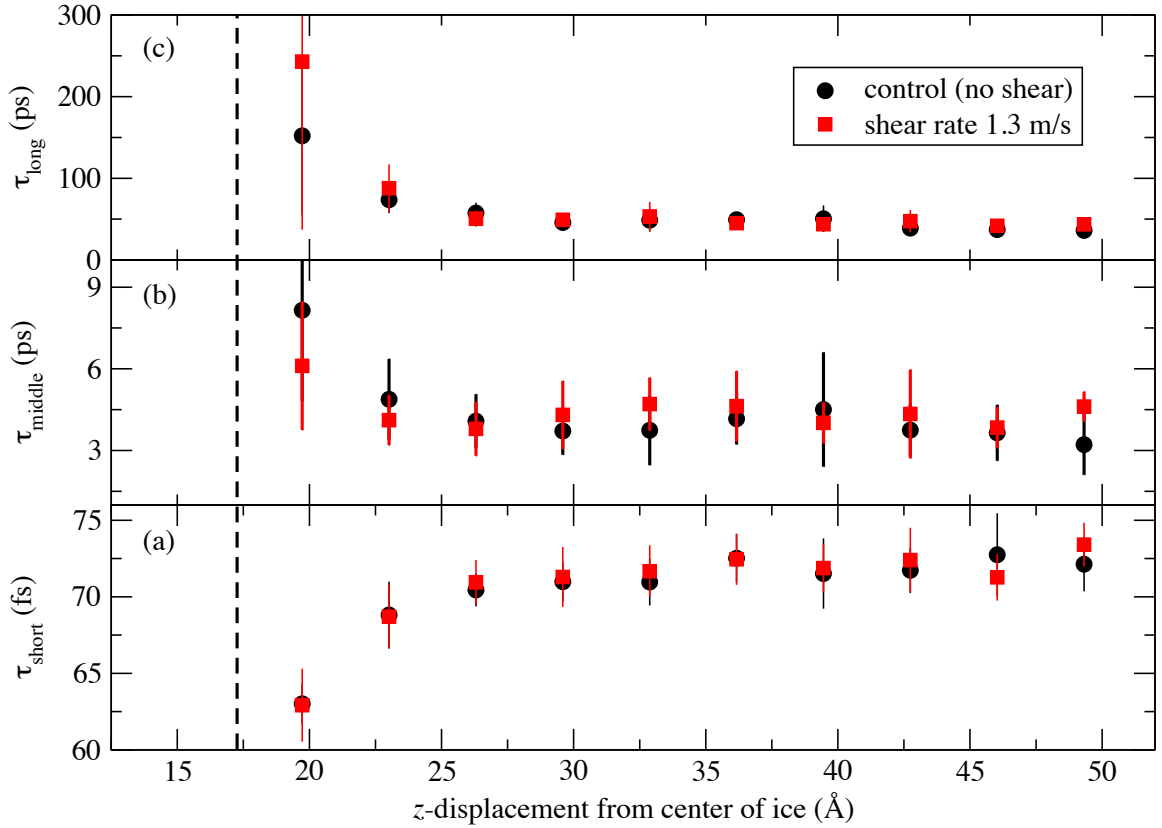


Figure 1.4. The three decay constants of the orientational time correlation function,  $C_2(t)$ , for water as a function of distance from the center of the ice slab. The dashed line indicates the location of the basal face (as determined from the tetrahedrality order parameter) and the black and red lines are fits of Eq. 3.9. The moderate and long time contributions slow down close to the interface which would be expected under reorganizations that involve large motions of the molecules (e.g. frame-reorientations and jumps). The observed speed-up in the short time contribution is surprising, but appears to reflect the restricted motion of librations closer to the interface.

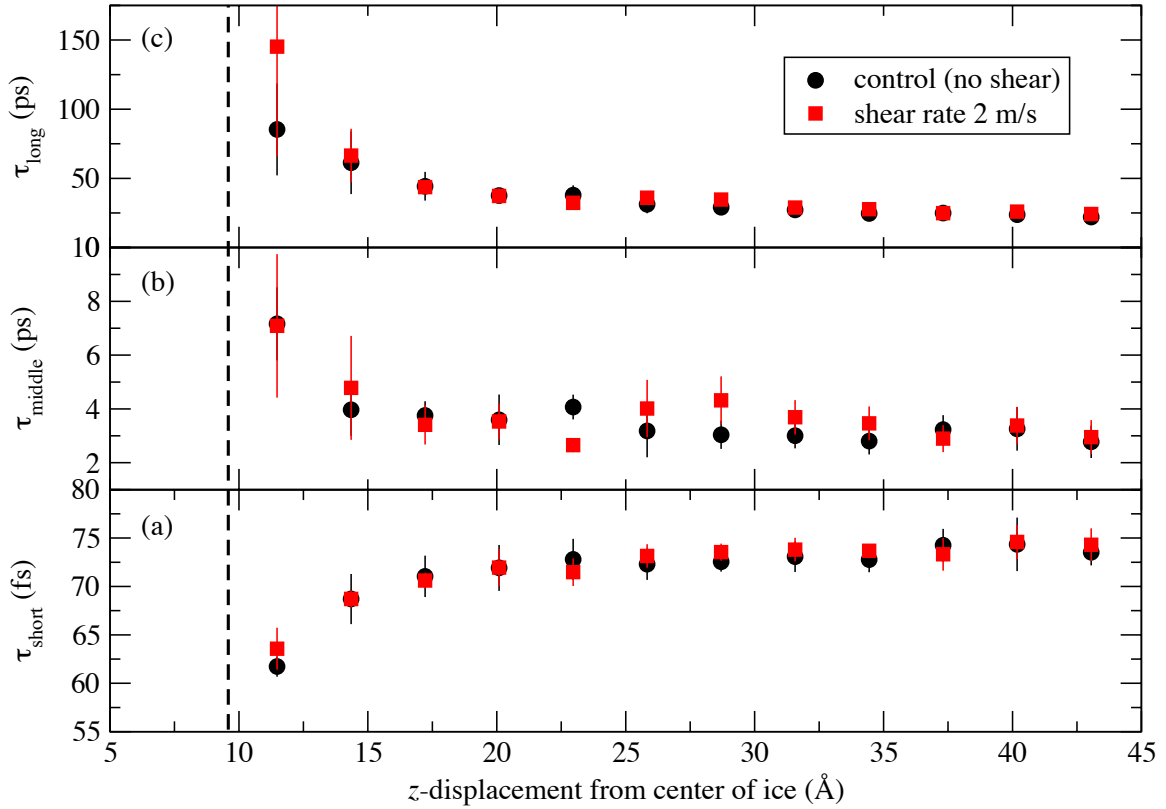


Figure 1.5. Decay constants for  $C_2(t)$  at the prismatic interface. Panel descriptions match those in figure 1.4.

Figures 1.4 and 1.5 show the three decay constants for the orientational time correlation function for water at varying displacements from the center of the ice slab for both the basal and prismatic interfaces. The vertical dotted lines indicate the locations of the midpoints of the interfaces as determined by the tetrahedrality fits. In the liquid regions,  $\tau_{middle}$  and  $\tau_{long}$  have consistent values around 3-4 ps and 20-40 ps, respectively, and increase in value approaching the interface. According to the jump model of Laage and Hynes *et al.*,? ?  $\tau_{middle}$  corresponds to the breaking and making of hydrogen bonds and  $\tau_{long}$  is explained with translational motion of the molecules (i.e. frame reorientation). The shortest of the three decay constants, the librational time  $\tau_{short}$  has a value of about 70 fs in the liquid region, and decreases in value approaching the interface. The observed speed-up in the short time contribution is surprising, but appears to reflect the restricted motion of librations closer to the interface.

The control systems (with no applied momentum flux) are shown with black symbols in figs. 1.4 and 1.5, while those obtained while a shear was active are shown in red.

Two notable features deserve clarification. First, there are nearly-constant liquid-state values for  $\tau_{short}$ ,  $\tau_{middle}$ , and  $\tau_{long}$  at large displacements from the interface. Second, there appears to be a single distance,  $d_{basal}$  or  $d_{prismatic}$ , from the interface at which all three decay times begin to deviate from their bulk liquid values. To quantify this distance, each of the decay constant  $z$ -profiles were fit to

$$\tau(z) \approx \tau_{liquid} + (\tau_{solid} - \tau_{liquid})e^{-(z-z_{wall})/d} \quad (1.9)$$

where  $\tau_{liquid}$  and  $\tau_{solid}$  are the liquid and projected solid values of the decay constants,  $z_{wall}$  is the location of the interface, and  $d$  is the displacement the deviations occur at (see Figures 1.4 and 1.5). The displacements  $d_{basal}$  and  $d_{prismatic}$  were determined

for each of the three decay constants, and then averaged for better statistics. For the basal system, we found  $d_{basal}$  for the control set to be 2.9 Å and 2.8 Å for a simulation with a shear rate of 1.3 ms<sup>-1</sup>. We found  $d_{prismatic}$  to be slightly larger than  $d_{basal}$  for both the control and an applied shear, with displacements of 3.6 Å for the control system and 3.5 Å for a simulation with a 2 ms<sup>-1</sup> shear rate. From this we can conclude there is no apparent dependence on the shear rate for the dynamic interface width.

Beaglehole and Wilson have measured the ice/water interface using ellipsometry and find a thickness of approximately 10 Å for both the basal and prismatic faces.<sup>?</sup> Structurally, we have found the basal and prismatic interfacial width to be 3.2 ± 0.4 Å and 3.6 ± 0.2 Å. Decomposition of the spatial dependence of the decay times of  $C_2(t)$  shows good agreement with the structural interfacial width determined by the local tetrahedrality.

### 1.3.2 Coefficient of Friction of the Interface

As liquid water flows over an ice interface, there is a distance from the structural interface where bulk-like hydrodynamics are recovered. Bocquet and Barrat constructed a theory for the hydrodynamic boundary parameters, which include the slipping length ( $\delta_{wall}$ ) of this boundary layer and the “hydrodynamic position” of the boundary ( $z_{wall}$ ).<sup>?</sup> ? This last parameter is the location (relative to a solid surface) where the bulk-like behavior is recovered. Work by Mundy *et al.* has helped to combine these parameters into a liquid-solid friction coefficient, which quantifies the resistance to pulling the solid interface through a liquid,<sup>?</sup>

$$\lambda_{wall} = \frac{\eta}{\delta_{wall}}. \quad (1.10)$$

This expression is nearly identical to one provided by Pit *et al.* for the solid-liquid friction of an interface,<sup>?</sup>

$$\lambda = \frac{\eta}{\delta} \quad (1.11)$$

where  $\delta$  is the slip length for the liquid measured at the location of the interface itself. In our simulations, the shoulder on the velocity profile indicating the location of the hydrodynamic boundary in the liquid is not always apparent. In some cases, the linear behavior persists nearly up to the interfacial region. For this reason, the hydrodynamic position of the boundary is not always computable, while the Pit approach (Eq. 1.11) can be used to find the solid-liquid friction coefficient more reliably.

In both the Pit and hydrodynamic boundary expressions,  $\eta$  is the shear viscosity of the bulk-like region of the liquid, a quantity which is easily obtained in VSS-RNEMD simulations by fitting the velocity profile in the region far from the surface.<sup>?</sup> Assuming linear response in the bulk-like region,

$$j_z(p_x) = -\eta \left( \frac{\partial v_x}{\partial z} \right) \quad (1.12)$$

Substituting this result into eq. (1.11), we can estimate the solid-liquid coefficient using the slip length,

$$\lambda = -\frac{j_z(p_x)}{\left( \frac{\partial v_x}{\partial z} \right) \delta} \quad (1.13)$$

For ice / water interfaces, the boundary conditions are no-slip, so projecting the bulk liquid state velocity profile yields a negative slip length. This length is the difference between the structural edge of the ice (determined by the tetrahedrality profile) and the location where the projected velocity of the bulk liquid intersects the solid phase velocity (see Figure 1.6). The coefficients of friction for the basal and the prismatic facets were determined for shearing along both the  $x$  and  $y$  axes. The

values are given in table 1.3.

Note that the measured friction coefficient for the basal face is twice that of the prismatic face (regardless of drag direction). These results may seem surprising as the basal face appears smoother than the prismatic with only small undulations of the oxygen positions, while the prismatic surface has deep corrugated channels along the  $x$  direction in the crystal system used in this work. However, the corrugations are relatively thin, and the liquid phase water does not appear to populate the channels. The prismatic face therefore effectively presents stripes of solid-phase molecules (making up approximately half of the exposed surface area) with nearly empty space between them. The interfacial friction appears to be independent of the drag direction, so flow parallel to these channels does not explain the lower friction of the prismatic face. A more likely explanation is that the effective contact between the liquid phase and the prismatic face is reduced by the empty corrugations.

TABLE 1.3

Solid-liquid friction coefficients (measured in amu fs<sup>-1</sup>)

Interface	Drag direction	
	$x$	$y$
basal	0.08 ± 0.02	0.09 ± 0.03
prismatic	0.037 ± 0.008	0.04 ± 0.01

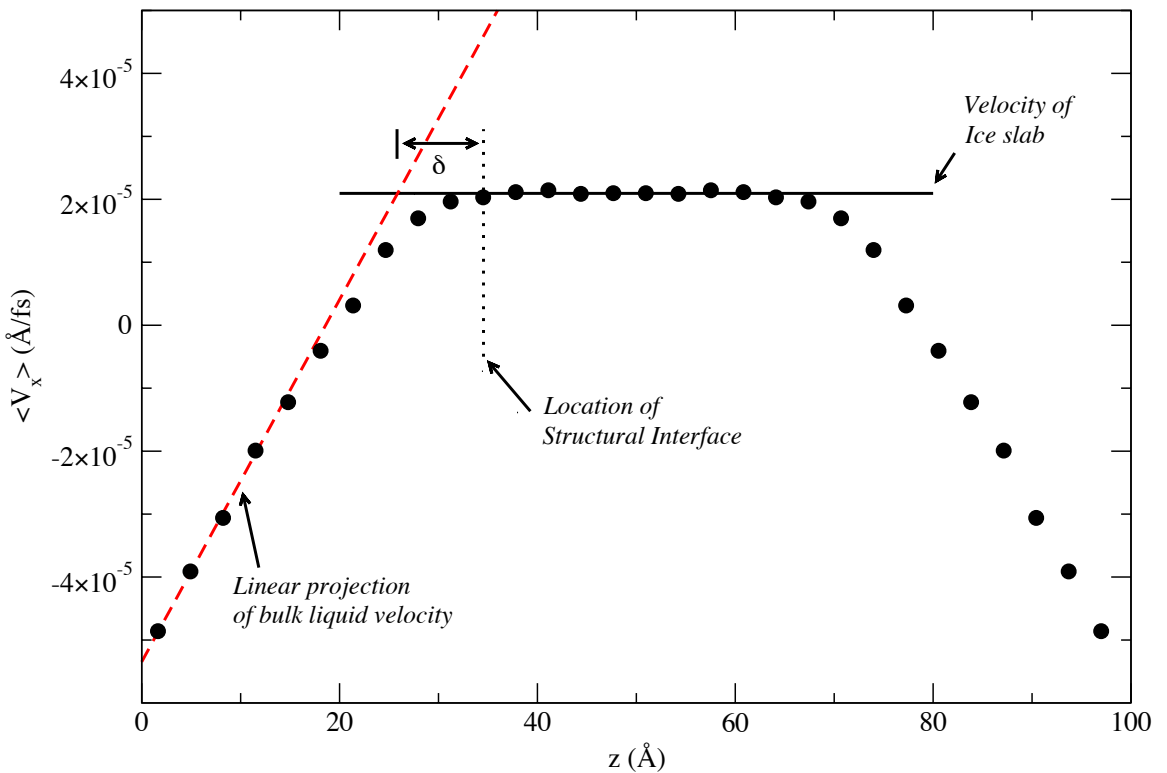


Figure 1.6. Determining the (negative) slip length ( $\delta$ ) for the ice-water interfaces (which have decidedly non-slip behavior). This length is the difference between the structural edge of the ice (determined by the tetrahedrality profile) and the location where the projected velocity of the bulk liquid (dashed red line) intersects the solid phase velocity (solid black line). The dotted line indicates the location of the ice as determined by the tetrahedrality profile. This example is taken from the basal-face simulation with an applied shear rate of  $3.0 \text{ ms}^{-1}$ .

## 1.4 Conclusion

We have simulated the basal and prismatic facets of an SPC/E model of the ice I<sub>h</sub> / water interface. Using VSS-RNEMD, the ice was sheared relative to the liquid while simultaneously being exposed to a weak thermal gradient which kept the interface at a stable temperature. Calculation of the local tetrahedrality order parameter has shown an apparent independence of the interfacial width on the shear rate. This width was found to be  $3.2 \pm 0.4$  Å and  $3.6 \pm 0.2$  Å for the basal and prismatic systems, respectively.

Orientational time correlation functions were calculated at varying displacements from the interface, and were found to be similarly independent of the applied momentum flux. The short decay due to the restoring forces of existing hydrogen bonds decreased close to the interface, while the longer-time decay constants increased in close proximity to the interface. There is also an apparent dynamic interface width,  $d_{basal}$  and  $d_{prismatic}$ , at which these deviations from bulk liquid values begin. We found  $d_{basal}$  and  $d_{prismatic}$  to be approximately 2.8 Å and 3.5 Å . This interfacial width is in good agreement with values determined by the structural analysis of the interface, by the hyperbolic tangent fit of the local tetrahedral order parameter.

The coefficient of liquid-solid friction for each of the facets was also determined. They were found to be  $0.07 \pm 0.01$  amu fs<sup>-1</sup> and  $0.032 \pm 0.007$  amu fs<sup>-1</sup> for the basal and prismatic facets respectively. We attribute the large difference between the two friction coefficients to the direction of the shear and to the surface structure of the crystal facets.

## CHAPTER 2

The different facets of ice have different hydrophilicities:

Friction at water / ice-I<sub>h</sub> interfaces

We present evidence that the prismatic and secondary prism facets of ice-I<sub>h</sub> crystals possess structural features that can reduce the effective hydrophilicity of the ice/water interface. The spreading dynamics of liquid water droplets on ice facets exhibits long-time behavior that differs for the prismatic {10̄10} and secondary prism {11̄20} facets when compared with the basal {0001} and pyramidal {20̄21} facets. We also present the results of simulations of solid-liquid friction of the same four crystal facets being drawn through liquid water, and find that the two prismatic facets exhibit roughly half the solid-liquid friction of the basal and pyramidal facets. These simulations provide evidence that the two prismatic faces have a significantly smaller effective surface area in contact with the liquid water. The ice / water interfacial widths for all four crystal facets are similar (using both structural and dynamic measures), and were found to be independent of the shear rate. Additionally, decomposition of orientational time correlation functions show position-dependence for the short- and longer-time decay components close to the interface.

### 2.1 Introduction

Surfaces can be characterized as hydrophobic or hydrophilic based on the strength of the interactions with water. Hydrophobic surfaces do not have strong enough interactions with water to overcome the internal attraction between molecules in the liquid phase, and the degree of hydrophilicity of a surface can be described by

the extent a droplet can spread out over the surface. The contact angle,  $\theta$ , formed between the solid and the liquid depends on the free energies of the three interfaces involved, and is given by Young's equation ? ,

$$\cos \theta = (\gamma_{sv} - \gamma_{sl}) / \gamma_{lv}. \quad (2.1)$$

Here  $\gamma_{sv}$ ,  $\gamma_{sl}$ , and  $\gamma_{lv}$  are the free energies of the solid/vapor, solid/liquid, and liquid/vapor interfaces, respectively. Large contact angles,  $\theta > 90^\circ$ , correspond to hydrophobic surfaces with low wettability, while small contact angles,  $\theta < 90^\circ$ , correspond to hydrophilic surfaces. Experimentally, measurements of the contact angle of sessile drops is often used to quantify the extent of wetting on surfaces with thermally selective wetting characteristics ? ? ? .

Nanometer-scale structural features of a solid surface can influence the hydrophilicity to a surprising degree. Small changes in the heights and widths of nano-pillars can change a surface from superhydrophobic,  $\theta \geq 150^\circ$ , to hydrophilic,  $\theta \sim 0^\circ$  ? . This is often referred to as the Cassie-Baxter to Wenzel transition. Nano-pillared surfaces with electrically tunable Cassie-Baxter and Wenzel states have also been observed ? ? ? ? ? . Luzar and coworkers have modeled these transitions on nano-patterned surfaces ? ? ? ? , and have found the change in contact angle is due to the field-induced perturbation of hydrogen bonding at the liquid/vapor interface ? .

One would expect the interfaces of ice to be highly hydrophilic (and possibly the most hydrophilic of all solid surfaces). In this paper we present evidence that some of the crystal facets of ice-I<sub>h</sub> have structural features that can reduce the effective hydrophilicity. Our evidence for this comes from molecular dynamics (MD) simulations of the spreading dynamics of liquid droplets on these facets, as well as reverse non-equilibrium molecular dynamics (RNEMD) simulations of solid-liquid friction.

Quiescent ice-I<sub>h</sub>/water interfaces have been studied extensively using computer simulations. Hayward and Haymet characterized and measured the widths of these interfaces [11, 12]. Nada and Furukawa have also modeled the width of basal/water and prismatic/water interfaces [13] as well as crystal restructuring at temperatures approaching the melting point [14].

The surface of ice exhibits a pre-melting layer, often called a quasi-liquid layer (QLL), at temperatures near the melting point. MD simulations of the facets of ice-I<sub>h</sub> exposed to vacuum have found QLL widths of approximately 10 Å at 3 K below the melting point [15]. Similarly, Limmer and Chandler have used the mW water model [16] and statistical field theory to estimate QLL widths at similar temperatures to be about 3 nm [17].

Recently, Sazaki and Furukawa have developed a technique using laser confocal microscopy combined with differential interference contrast microscopy that has sufficient spatial and temporal resolution to visualize and quantitatively analyze QLLs on ice crystals at temperatures near melting [18]. They have found the width of the QLLs perpendicular to the surface at -2.2°C to be 3-4 Å wide. They have also seen the formation of two immiscible QLLs, which displayed different dynamics on the crystal surface [19].

Using molecular dynamics simulations, Samadashvili has recently shown that when two smooth ice slabs slide past one another, a stable liquid-like layer develops between them [20]. In a previous study, our RNEMD simulations of ice-I<sub>h</sub> shearing through liquid water have provided quantitative estimates of the solid-liquid kinetic friction coefficients [21]. These displayed a factor of two difference between the basal and prismatic facets. The friction was found to be independent of shear direction relative to the surface orientation. We attributed facet-based difference in liquid-solid friction to the 6.5 Å corrugation of the prismatic face which reduces the effective surface area of the ice that is in direct contact with liquid water.

In the sections that follow, we describe the simulations of droplet-spreading dynamics using standard MD as well as simulations of tribological properties using RNEMD. These simulations give complementary results that point to the prismatic and secondary prism facets having roughly half of their surface area in direct contact with the liquid.

## 2.2 Methodology

### 2.2.1 Construction of the Ice / Water interfaces

Ice I<sub>h</sub> crystallizes in the hexagonal space group P6<sub>3</sub>/mmc, and common ice crystals form hexagonal plates with the basal face, {0001}, forming the top and bottom of each plate, and the prismatic facet, {10\bar{1}0}, forming the sides. In extreme temperatures or low water saturation conditions, ice crystals can easily form as hollow columns, needles and dendrites. These are structures that expose other crystalline facets of the ice to the surroundings. Among the more common facets are the secondary prism, {11\bar{2}0}, and pyramidal, {20\bar{2}1}, faces.

We found it most useful to work with proton-ordered, zero-dipole crystals that expose strips of dangling H-atoms and lone pairs ? . Our structures were created starting from Structure 6 of Hirsch and Ojamäe's set of orthorhombic representations for ice-I<sub>h</sub> ? . This crystal structure was cleaved along the four different facets. The exposed face was reoriented normal to the *z*-axis of the simulation cell, and the structures were extended to form large exposed facets in rectangular box geometries. Liquid water boxes were created with identical dimensions (in *x* and *y*) as the ice, with a *z* dimension of three times that of the ice block, and a density corresponding to 1 g / cm<sup>3</sup>. Each of the ice slabs and water boxes were independently equilibrated at a pressure of 1 atm, and the resulting systems were merged by carving out any liquid water molecules within 3 Å of any atoms in the ice slabs. Each of the combined

ice/water systems were then equilibrated at 225K, which is the liquid-ice coexistence temperature for SPC/E water [1]. Reference [1] contains a more detailed explanation of the construction of similar ice/water interfaces. The resulting dimensions as well as the number of ice and liquid water molecules contained in each of these systems are shown in Table 3.1.

The SPC/E water model [1] has been extensively characterized over a wide range of liquid conditions [2-5], and its phase diagram has been well studied [2-5]. With longer cutoff radii and careful treatment of electrostatics, SPC/E mostly avoids metastable crystalline morphologies like ice-*i* [6] and ice-B [7]. The free energies and melting points [2-5] of various other crystalline polymorphs have also been calculated. Haymet *et al.* have studied quiescent Ice-I<sub>h</sub>/water interfaces using the SPC/E water model, and have seen structural and dynamic measurements of the interfacial width that agree well with more expensive water models, although the coexistence temperature for SPC/E is still well below the experimental melting point of real water [8]. Given the extensive data and speed of this model, it is a reasonable choice even though the temperatures required are somewhat lower than real ice / water interfaces.

### 2.3 Droplet Simulations

Ice surfaces with a thickness of  $\sim 20 \text{ \AA}$  were created as described above, but were not solvated in a liquid box. The crystals were then replicated along the *x* and *y* axes (parallel to the surface) until a large surface ( $> 126 \text{ nm}^2$ ) had been created. The sizes and numbers of molecules in each of the surfaces is given in Table S1. Weak translational restraining potentials with spring constants of  $1.5 \text{ kcal mol}^{-1} \text{ \AA}^{-2}$  (prismatic and pyramidal facets) or  $4.0 \text{ kcal mol}^{-1} \text{ \AA}^{-2}$  (basal facet) were applied to the centers of mass of each molecule in order to prevent surface melting, although the molecules were allowed to reorient freely. A water droplet containing 2048 SPC/E

molecules was created separately. Droplets of this size can produce agreement with the Young contact angle extrapolated to an infinite drop size ? . The surfaces and droplet were independently equilibrated to 225 K, at which time the droplet was placed 3-5 Å above the surface. Five statistically independent simulations were carried out for each facet, and the droplet was placed at unique  $x$  and  $y$  locations for each of these simulations. Each simulation was 5 ns in length and was conducted in the microcanonical (NVE) ensemble. Representative configurations for the droplet on the prismatic facet are shown in figure 2.1.

## 2.4 Shearing Simulations (Interfaces in Bulk Water)

To perform the shearing simulations, the velocity shearing and scaling variant of reverse non-equilibrium molecular dynamics (VSS-RNEMD) was employed ? . This method performs a series of simultaneous non-equilibrium exchanges of linear momentum and kinetic energy between two physically-separated regions of the simulation cell. The system responds to this unphysical flux with velocity and temperature gradients. When VSS-RNEMD is applied to bulk liquids, transport properties like the thermal conductivity and the shear viscosity are easily extracted assuming a linear response between the flux and the gradient. At the interfaces between dissimilar materials, the same method can be used to extract *interfacial* transport properties (e.g. the interfacial thermal conductance and the hydrodynamic slip length).

The kinetic energy flux (producing a thermal gradient) is necessary when performing shearing simulations at the ice-water interface in order to prevent the frictional heating due to the shear from melting the crystal. Reference ? provides more details on the VSS-RNEMD method as applied to ice-water interfaces. A representative configuration of the solvated prismatic facet being sheared through liquid water is shown in figure 3.2.

All simulations were performed using OpenMD ?? , with a time step of 2 fs and

periodic boundary conditions in all three dimensions. Electrostatics were handled using the damped-shifted force real-space electrostatic kernel ? .

The interfaces were equilibrated for a total of 10 ns at equilibrium conditions before being exposed to either a shear or thermal gradient. This consisted of 5 ns under a constant temperature (NVT) integrator set to 225 K followed by 5 ns under a microcanonical (NVE) integrator. Weak thermal gradients were allowed to develop using the VSS-RNEMD (NVE) integrator using a small thermal flux ( $-2.0 \times 10^{-6}$  kcal/mol/Å<sup>2</sup>/fs) for a duration of 5 ns to allow the gradient to stabilize. The resulting temperature gradient was  $\approx 10$ K over the entire box length, which was sufficient to keep the temperature at the interface within  $\pm 1$  K of the 225 K target.

Velocity gradients were then imposed using the VSS-RNEMD (NVE) integrator with a range of momentum fluxes. The systems were divided into 100 bins along the  $z$ -axis for the VSS-RNEMD moves, which were attempted every time step. Although computationally expensive, this was done to minimize the magnitude of each individual momentum exchange. Because individual VSS-RNEMD exchange moves conserve both total energy and linear momentum, the method can be “bolted-on” to simulations in any ensemble. The simulations of the pyramidal interface were performed under the canonical (NVT) ensemble. When time correlation functions were computed, the RNEMD simulations were done in the microcanonical (NVE) ensemble. All simulations of the other interfaces were carried out in the microcanonical ensemble.

These gradients were allowed to stabilize for 1 ns before data collection started. Once established, four successive 0.5 ns runs were performed for each shear rate. During these simulations, configurations of the system were stored every 1 ps, and statistics on the structure and dynamics in each bin were accumulated throughout the simulations. Although there was some small variation in the measured interfacial width between successive runs, no indication of bulk melting or crystallization was

observed. That is, no large scale changes in the positions of the top and bottom interfaces occurred during the simulations.

## 2.5 Results

### 2.5.1 Ice - Water Contact Angles

To determine the extent of wetting for each of the four crystal facets, contact angles for liquid droplets on the ice surfaces were computed using two methods. In the first method, the droplet is assumed to form a spherical cap, and the contact angle is estimated from the  $z$ -axis location of the droplet's center of mass ( $z_{\text{cm}}$ ). This procedure was first described by Hautman and Klein ? , and was utilized by Hirvi and Pakkanen in their investigation of water droplets on polyethylene and poly(vinyl chloride) surfaces ? . For each stored configuration, the contact angle,  $\theta$ , was found by inverting the expression for the location of the droplet center of mass,

$$\langle z_{\text{cm}} \rangle = 2^{-4/3} R_0 \left( \frac{1 - \cos\theta}{2 + \cos\theta} \right)^{1/3} \frac{3 + \cos\theta}{2 + \cos\theta}, \quad (2.2)$$

where  $R_0$  is the radius of the free water droplet.

In addition to the spherical cap method outlined above, a second method for obtaining the contact angle was described by Ruijter, Blake, and Coninck ? . This method uses a cylindrical averaging of the droplet's density profile. A threshold density of  $0.5 \text{ g cm}^{-3}$  is used to estimate the location of the edge of the droplet. The  $r$  and  $z$ -dependence of the droplet's edge is then fit to a circle, and the contact angle is computed from the intersection of the fit circle with the  $z$ -axis location of the solid surface. Again, for each stored configuration, the density profile in a set of annular shells was computed. Due to large density fluctuations close to the ice, all shells located within  $2 \text{ \AA}$  of the ice surface were left out of the circular fits. The height of the solid surface ( $z_{\text{surface}}$ ) along with the best fitting origin ( $z_{\text{droplet}}$ ) and radius

( $r_{\text{droplet}}$ ) of the droplet can then be used to compute the contact angle,

$$\theta = 90 + \frac{180}{\pi} \sin^{-1} \left( \frac{z_{\text{droplet}} - z_{\text{surface}}}{r_{\text{droplet}}} \right). \quad (2.3)$$

Both methods provided similar estimates of the dynamic contact angle, although the spherical cap method is significantly less prone to noise, and is the method used to compute the contact angles in table 3.2.

Because the initial droplet was placed above the surface, the initial value of  $180^\circ$  decayed over time (See figure 1 in the SI). Each of these profiles were fit to a biexponential decay, with a short-time contribution ( $\tau_c$ ) that describes the initial contact with the surface, a long time contribution ( $\tau_s$ ) that describes the spread of the droplet over the surface, and a constant ( $\theta_\infty$ ) to capture the infinite-time estimate of the equilibrium contact angle,

$$\theta(t) = \theta_\infty + (180 - \theta_\infty) [ae^{-t/\tau_c} + (1-a)e^{-t/\tau_s}] \quad (2.4)$$

We have found that the rate for water droplet spreading across all four crystal facets,  $k_{\text{spread}} = 1/\tau_s \approx 0.7 \text{ ns}^{-1}$ . However, the basal and pyramidal facets produced estimated equilibrium contact angles,  $\theta_\infty \approx 35^\circ$ , while prismatic and secondary prismatic had values for  $\theta_\infty$  near  $43^\circ$  as seen in Table 3.2.

These results indicate that by traditional measures, the basal and pyramidal facets are more hydrophilic than the prismatic and secondary prism facets, and surprisingly, that the differential hydrophilicities of the crystal facets is not reflected in the spreading rate of the droplet.

### 2.5.2 Solid-liquid friction of the interfaces

In a bulk fluid, the shear viscosity,  $\eta$ , can be determined assuming a linear response to a shear stress,

$$j_z(p_x) = \eta \frac{\partial v_x}{\partial z}. \quad (2.5)$$

Here  $j_z(p_x)$  is the flux (in  $x$ -momentum) that is transferred in the  $z$  direction (i.e. the shear stress). The RNEMD simulations impose an artificial momentum flux between two regions of the simulation, and the velocity gradient is the fluid's response. This technique has now been applied quite widely to determine the viscosities of a number of bulk fluids [11, 12, 13].

At the interface between two phases (e.g. liquid / solid) the same momentum flux creates a velocity difference between the two materials, and this can be used to define an interfacial friction coefficient ( $\kappa$ ),

$$j_z(p_x) = \kappa [v_x(\text{liquid}) - v_x(\text{solid})] \quad (2.6)$$

where  $v_x(\text{solid})$  is the velocity of the solid and  $v_x(\text{liquid})$  is the velocity of the liquid measured at the hydrodynamic boundary layer.

The simulations described here contain significant quantities of both liquid and solid phases, and the momentum flux must traverse a region of the liquid that is simultaneously under a thermal gradient. Since the liquid has a temperature-dependent shear viscosity,  $\eta(T)$ , estimates of the solid-liquid friction coefficient can be obtained if one knows the viscosity of the liquid at the interface (i.e. at the melting temperature,  $T_m$ ),

$$\kappa = \frac{\eta(T_m)}{[v_x(\text{fluid}) - v_x(\text{solid})]} \left( \frac{\partial v_x}{\partial z} \right). \quad (2.7)$$

For SPC/E, the melting temperature of Ice-I<sub>h</sub> is estimated to be 225 K [14]. To obtain the value of  $\eta(225 \text{ K})$  for the SPC/E model, a  $31.09 \times 29.38 \times 124.39 \text{ \AA}$  box

with 3744 water molecules in a disordered configuration was equilibrated to 225 K, and five statistically-independent shearing simulations were performed (with imposed fluxes that spanned a range of  $3 \rightarrow 13 \text{ m s}^{-1}$ ). Each simulation was conducted in the microcanonical ensemble with total simulation times of 5 ns. The VSS-RNEMD exchanges were carried out every 2 fs. We estimate  $\eta(225 \text{ K})$  to be  $0.0148 \pm 0.0007 \text{ Pa s}$  for SPC/E, roughly ten times larger than the shear viscosity previously computed at 280 K ? .

The interfacial friction coefficient can equivalently be expressed as the ratio of the viscosity of the fluid to the hydrodynamic slip length,  $\kappa = \eta/\delta$ . The slip length is an indication of strength of the interactions between the solid and liquid phases, although the connection between slip length and surface hydrophobicity is not yet clear. In some simulations, the slip length has been found to have a link to the effective surface hydrophobicity ?, although Ho *et al.* have found that liquid water can also slip on hydrophilic surfaces ?. Experimental evidence for a direct tie between slip length and hydrophobicity ?, ?, . However, recent surface sensitive cross-correlation spectroscopy (TIR-FCCS) measurements have seen similar slip behavior for both hydrophobic and hydrophilic surfaces ? .

In each of the systems studied here, the interfacial temperature was kept fixed to 225 K, which ensured the viscosity of the fluid at the interface was identical. Thus, any significant variation in  $\kappa$  between the systems is a direct indicator of the slip length and the effective interaction strength between the solid and liquid phases.

The calculated  $\kappa$  values found for the four crystal facets of Ice-I<sub>h</sub> are shown in Table 3.2. The basal and pyramidal facets were found to have similar values of  $\kappa \approx 6 (\times 10^{-4} \text{ amu } \text{\AA}^{-2} \text{ fs}^{-1})$ , while the prismatic and secondary prism facets exhibited  $\kappa \approx 3 (\times 10^{-4} \text{ amu } \text{\AA}^{-2} \text{ fs}^{-1})$ . These results are also essentially independent of the direction

of the shear relative to channels on the surfaces of the facets. The friction coefficients indicate that the basal and pyramidal facets have significantly stronger interactions with liquid water than either of the two prismatic facets. This is in agreement with the contact angle results above - both of the high-friction facets exhibited smaller contact angles, suggesting that the solid-liquid friction (and inverse slip length) is correlated with the hydrophilicity of these facets.

### 2.5.3 Structural measures of interfacial width under shear

One of the open questions about ice/water interfaces is whether the thickness of the 'slush-like' quasi-liquid layer (QLL) depends on the facet of ice presented to the water. In the QLL region, the water molecules are ordered differently than in either the solid or liquid phases, and also exhibit distinct dynamical behavior. The width of this quasi-liquid layer has been estimated by finding the distance over which structural order parameters or dynamic properties change from their bulk liquid values to those of the solid ice. The properties used to find interfacial widths have included the local density, the diffusion constant, and both translational and orientational order parameters ? ? ? ? ? ? .

The VSS-RNEMD simulations impose thermal and velocity gradients. These gradients perturb the momenta of the water molecules, so parameters that depend on translational motion are often measuring the momentum exchange, and not physical properties of the interface. As a structural measure of the interface, we have used the local tetrahedral order parameter, which measures the match of the local molecular environments (e.g. the angles between nearest neighbor molecules) to perfect tetrahedral ordering. This quantity was originally described by Errington and Debenedetti ? and has been used in bulk simulations by Kumar *et al.* ? It has previously been used in ice/water interfaces by Bryk and Haymet ? .

To determine the structural widths of the interfaces under shear, each of the

systems was divided into 100 bins along the  $z$ -dimension, and the local tetrahedral order parameter (Eq. 5 in Reference ? ) was time-averaged in each bin for the duration of the shearing simulation. The spatial dependence of this order parameter,  $q(z)$ , is the tetrahedrality profile of the interface. The lower panels in figures 2-5 in the supporting information show tetrahedrality profiles (in circles) for each of the four interfaces. The  $q(z)$  function has a range of  $(0, 1)$ , where a value of unity indicates a perfectly tetrahedral environment. The  $q(z)$  for the bulk liquid was found to be  $\approx 0.77$ , while values of  $\approx 0.92$  were more common in the ice. The tetrahedrality profiles were fit using a hyperbolic tangent function (see Eq. 6 in Reference ? ) designed to smoothly fit the bulk to ice transition while accounting for the weak thermal gradient. In panels *b* and *c* of the same figures, the resulting thermal and velocity gradients from an imposed kinetic energy and momentum fluxes can be seen. The vertical dotted lines traversing these figures indicate the midpoints of the interfaces as determined by the tetrahedrality profiles. The hyperbolic tangent fit provides an estimate of  $d_{\text{struct}}$ , the structural width of the interface.

We find the interfacial width to be  $3.2 \pm 0.2$  Å (pyramidal) and  $3.2 \pm 0.2$  Å (secondary prism) for the control systems with no applied momentum flux. This is similar to our previous results for the interfacial widths of the quiescent basal ( $3.2 \pm 0.4$  Å) and prismatic systems ( $3.6 \pm 0.2$  Å).

Over the range of shear rates investigated,  $0.4 \rightarrow 6.0$  m s<sup>-1</sup> for the pyramidal system and  $0.6 \rightarrow 5.2$  m s<sup>-1</sup> for the secondary prism, we found no significant change in the interfacial width. The mean interfacial widths are collected in table 3.2. This follows our previous findings of the basal and prismatic systems, in which the interfacial widths of the basal and prismatic facets were also found to be insensitive to the shear rate ? .

The similarity of these interfacial width estimates indicate that the particular facet of the exposed ice crystal has little to no effect on how far into the bulk the ice-

like structural ordering persists. Also, it appears that for the shearing rates imposed in this study, the interfacial width is not structurally modified by the movement of water over the ice.

#### 2.5.4 Dynamic measures of interfacial width under shear

The spatially-resolved orientational time correlation function,

$$C_2(z, t) = \langle P_2(\mathbf{u}_i(0) \cdot \mathbf{u}_i(t))\delta(z_i(0) - z)\rangle, \quad (2.8)$$

provides local information about the decorrelation of molecular orientations in time. Here,  $P_2$  is the second-order Legendre polynomial, and  $\mathbf{u}_i$  is the molecular vector that bisects the HOH angle of molecule  $i$ . The angle brackets indicate an average over all the water molecules and time origins, and the delta function restricts the average to specific regions. In the crystal, decay of  $C_2(z, t)$  is incomplete, while in the liquid, correlation times are typically measured in ps. Observing the spatial-transition between the decay regimes can define a dynamic measure of the interfacial width.

To determine the dynamic widths of the interfaces under shear, each of the systems was divided into bins along the  $z$ -dimension ( $\approx 3$  Å wide) and  $C_2(z, t)$  was computed using only those molecules that were in the bin at the initial time. To compute these correlation functions, each of the 0.5 ns simulations was followed by a shorter 200 ps microcanonical (NVE) simulation in which the positions and orientations of every molecule in the system were recorded every 0.1 ps.

The time-dependence was fit to a triexponential decay, with three time constants:  $\tau_{short}$ , measuring the librational motion of the water molecules,  $\tau_{middle}$ , measuring the timescale for breaking and making of hydrogen bonds, and  $\tau_{long}$ , corresponding to the translational motion of the water molecules. An additional constant was introduced

in the fits to describe molecules in the crystal which do not experience long-time orientational decay.

In Figures 6-9 in the supporting information, the  $z$ -coordinate profiles for the three decay constants,  $\tau_{short}$ ,  $\tau_{middle}$ , and  $\tau_{long}$  for the different interfaces are shown.

(Figures 6 & 7 are new results, and Figures 8 & 9 are updated plots from Ref ? .)

. In the liquid regions of all four interfaces, we observe  $\tau_{middle}$  and  $\tau_{long}$  to have approximately consistent values of 3 – 6 ps and 30 – 40 ps, respectively. Both of these times increase in value approaching the interface. Approaching the interface, we also observe that  $\tau_{short}$  decreases from its liquid-state value of 72 – 76 fs. The approximate values for the decay constants and the trends approaching the interface match those reported previously for the basal and prismatic interfaces.

We have estimated the dynamic interfacial width  $d_{dyn}$  by fitting the profiles of all the three orientational time constants with an exponential decay to the bulk-liquid behavior,

$$\tau(z) \approx \tau_{liquid} + (\tau_{wall} - \tau_{liquid})e^{-(z-z_{wall})/d_{dyn}} \quad (2.9)$$

where  $\tau_{liquid}$  and  $\tau_{wall}$  are the liquid and projected wall values of the decay constants,  $z_{wall}$  is the location of the interface, as measured by the structural order parameter. These values are shown in table 3.2. Because the bins must be quite wide to obtain reasonable profiles of  $C_2(z, t)$ , the error estimates for the dynamic widths of the interface are significantly larger than for the structural widths. However, all four interfaces exhibit dynamic widths that are significantly below 1 nm, and are in reasonable agreement with the structural width above.

## 2.6 Conclusions

In this work, we used MD simulations to measure the advancing contact angles of water droplets on the basal, prismatic, pyramidal, and secondary prism facets of

Ice-I<sub>h</sub>. Although we saw no significant change in the *rate* at which the droplets spread over the surface, the long-time behavior predicts larger equilibrium contact angles for the two prismatic facets.

We have also used RNEMD simulations of water interfaces with the same four crystal facets to compute solid-liquid friction coefficients. We have observed coefficients of friction that differ by a factor of two between the two prismatic facets and the basal and pyramidal facets. Because the solid-liquid friction coefficient is directly tied to the inverse of the hydrodynamic slip length, this suggests that there are significant differences in the overall interaction strengths between these facets and the liquid layers immediately in contact with them.

The agreement between these two measures have lead us to conclude that the two prismatic facets have a lower hydrophilicity than either the basal or pyramidal facets. One possible explanation of this behavior is that the face presented by both prismatic facets consists of deep, narrow channels (i.e. stripes of adjacent rows of pairs of hydrogen-bound water molecules). At the surfaces of these facets, the channels are 6.35 Å wide and the sub-surface ice layer is 2.25 Å below (and therefore blocked from hydrogen bonding with the liquid). This means that only 1/2 of the surface molecules can form hydrogen bonds with liquid-phase molecules.

In the basal plane, the surface features are shallower (1.3 Å), with no blocked subsurface layer. The pyramidal face has much wider channels (8.65 Å) which are also quite shallow (1.37 Å). These features allow liquid phase molecules to form hydrogen bonds with all of the surface molecules in the basal and pyramidal facets. This means that for similar surface areas, the two prismatic facets have an effective hydrogen bonding surface area of half of the basal and pyramidal facets. The reduction in the effective surface area would explain much of the behavior observed in our simulations.

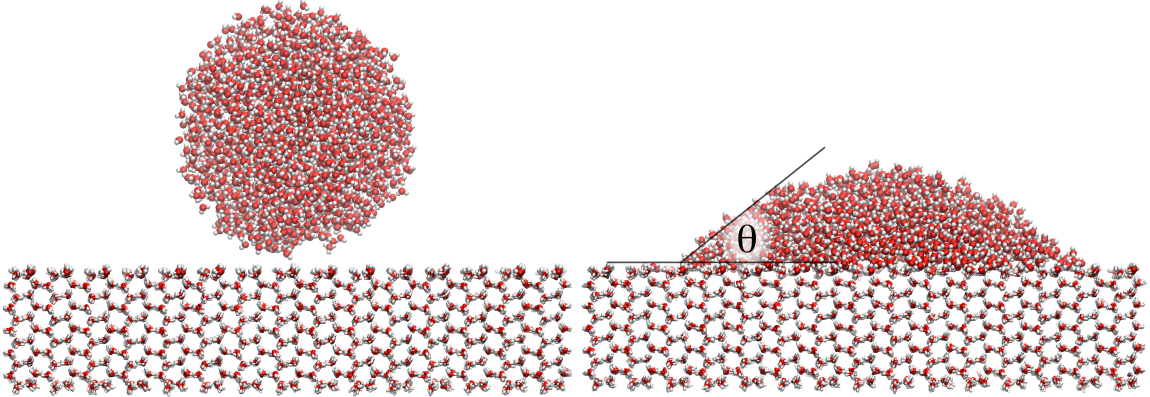


Figure 2.1. Computational model of a droplet of liquid water spreading over the prismatic  $\{10\bar{1}0\}$  facet of ice, before (left) and 2.6 ns after (right) being introduced to the surface. The contact angle ( $\theta$ ) shrinks as the simulation proceeds, and the long-time behavior of this angle is used to estimate the hydrophilicity of the facet.

## 2.7 The Advancing Contact Angle

The advancing contact angles for the liquid droplets were computed using inversion of Eq. (2) in the main text which requires finding the real roots of a fourth order polynomial,

$$c_4 \cos^4 \theta + c_3 \cos^3 \theta + c_2 \cos^2 \theta + c_1 \cos \theta + c_0 = 0 \quad (2.10)$$

where the coefficients of the polynomial are expressed in terms of the  $z$  coordinate of the center of mass of the liquid droplet relative to the solid surface,  $z = z_{\text{cm}} - z_{\text{surface}}$ , and a factor that depends on the initial droplet radius,  $k = 2^{-4/3}R_0$ . The coefficients

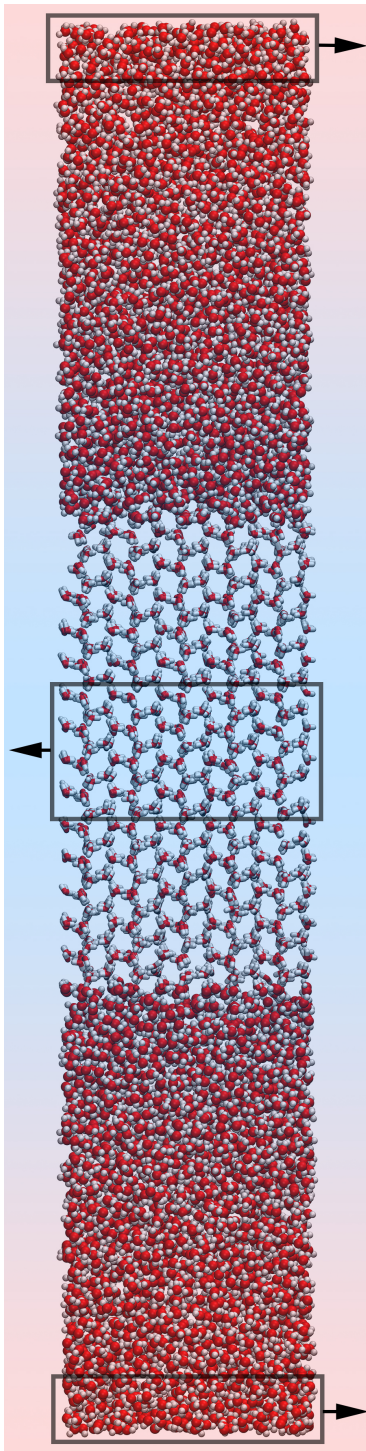


Figure 2.2. Computational model of a slab of ice being sheared through liquid water. In this figure, the ice is presenting two copies of the prismatic  $\{10\bar{1}0\}$  facet towards the liquid phase. The RNEMD simulation exchanges both linear momentum (indicated with arrows) and kinetic energy between the central box and the box that spans the cell boundary. The system responds with weak thermal gradient and a velocity profile that shears the ice relative to the surrounding liquid.

TABLE 2.1

Sizes of the droplet and shearing simulations. Cell dimensions are measured in Å.

2*Interface	Droplet				Shearing				
	$N_{\text{ice}}$	$N_{\text{droplet}}$	$L_x$	$L_y$	$N_{\text{ice}}$	$N_{\text{liquid}}$	$L_x$	$L_y$	$L_z$
Basal {0001}	12960	2048	134.70	140.04	900	1846	23.87	35.83	98.64
Pyramidal {20̄21}	11136	2048	143.75	121.41	1216	2203	37.47	29.50	93.02
Prismatic {10̄10}	9900	2048	110.04	115.00	3000	5464	35.95	35.65	205.7
Secondary Prism {11̄20}	11520	2048	146.72	124.48	3840	8176	71.87	31.66	161.5

are simple functions of these two quantities,

$$c_4 = z^3 + k^3 \quad (2.11)$$

$$c_3 = 8z^3 + 8k^3 \quad (2.12)$$

$$c_2 = 24z^3 + 18k^3 \quad (2.13)$$

$$c_1 = 32z^3 \quad (2.14)$$

$$c_0 = 16z^3 - 27k^3. \quad (2.15)$$

Solving for the values of the real roots of this polynomial (Eq. 2.10) give estimates of the advancing contact angle. The dynamics of this quantity for each of the four interfaces is shown in figure 1 below.

## 2.8 Interfacial widths using structural information

To determine the structural widths of the interfaces under shear, each of the systems was divided into 100 bins along the  $z$ -dimension, and the local tetrahedral

TABLE 2.2

Structural and dynamic properties of the interfaces of Ice-I<sub>h</sub> with water.

2*Interface	Channel Size		Droplet		Shearing		
	Width (Å)	Depth (Å)	$\theta_\infty$ (°)	$k_{\text{spread}}$ (ns <sup>-1</sup> )	$\kappa_x$	$\kappa_y$	$d_{\text{struc}}$
Basal {0001}	4.49	1.30	34.1(9)	0.60(7)	5.9(3)	6.5(8)	3.2
Pyramidal {20̄21}	8.65	1.37	35(3)	0.7(1)	5.8(4)	6.1(5)	3.2
Prismatic {10̄10}	6.35	2.25	45(3)	0.75(9)	3.0(2)	3.0(1)	3.0
Secondary Prism {11̄20}	6.35	2.25	43(2)	0.69(3)	3.5(1)	3.3(2)	3.2

<sup>1</sup>Liquid-solid friction coefficients ( $\kappa_x$  and  $\kappa_y$ ) are expressed in 10<sup>-4</sup> amu Å<sup>-2</sup> fs<sup>-1</sup>.<sup>2</sup>Uncertainties in the last digits are given in parentheses.

order parameter (Eq. 5 in Reference ? ) was time-averaged in each bin for the duration of the shearing simulation. The spatial dependence of this order parameter,  $q(z)$ , is the tetrahedrality profile of the interface. The lower panels in figures 2-5 show tetrahedrality profiles (in circles) for each of the four interfaces. The  $q(z)$  function has a range of (0, 1), where a value of unity indicates a perfectly tetrahedral environment. The  $q(z)$  for the bulk liquid was found to be  $\approx 0.77$ , while values of  $\approx 0.92$  were more common in the ice. The tetrahedrality profiles were fit using a hyperbolic tangent function (see Eq. 6 in Reference ? ) designed to smoothly fit the bulk to ice transition while accounting for the weak thermal gradient. In panels *b* and *c* of the same figures, the resulting thermal and velocity gradients from an imposed kinetic energy and momentum fluxes can be seen. The vertical dotted lines traversing these figures indicate the midpoints of the interfaces as determined by the tetrahedrality profiles.

## 2.9 Interfacial widths using dynamic information

To determine the dynamic widths of the interfaces under shear, each of the systems was divided into bins along the  $z$ -dimension ( $\approx 3 \text{ \AA}$  wide) and  $C_2(z, t)$  was computed using only those molecules that were in the bin at the initial time. To compute these correlation functions, each of the 0.5 ns simulations was followed by a shorter 200 ps microcanonical (NVE) simulation in which the positions and orientations of every molecule in the system were recorded every 0.1 ps.

The time-dependence was fit to a triexponential decay, with three time constants:  $\tau_{short}$ , measuring the librational motion of the water molecules,  $\tau_{middle}$ , measuring the timescale for breaking and making of hydrogen bonds, and  $\tau_{long}$ , corresponding to the translational motion of the water molecules. An additional constant was introduced in the fits to describe molecules in the crystal which do not experience long-time orientational decay.

In Figures 6-9, the  $z$ -coordinate profiles for the three decay constants,  $\tau_{short}$ ,  $\tau_{middle}$ , and  $\tau_{long}$  for the different interfaces are shown. (Figures 6 & 7 are new results, and Figures 8 & 9 are updated plots from Ref ? .) In the liquid regions of all four interfaces, we observe  $\tau_{middle}$  and  $\tau_{long}$  to have approximately consistent values of 3–6 ps and 30–40 ps, respectively. Both of these times increase in value approaching the interface. Approaching the interface, we also observe that  $\tau_{short}$  decreases from its liquid-state value of 72 – 76 fs. The approximate values for the decay constants and the trends approaching the interface match those reported previously for the basal and prismatic interfaces.

We have estimated the dynamic interfacial width  $d_{\text{dyn}}$  by fitting the profiles of all the three orientational time constants with an exponential decay to the bulk-liquid behavior,

$$\tau(z) \approx \tau_{liquid} + (\tau_{wall} - \tau_{liquid})e^{-(z-z_{wall})/d_{\text{dyn}}} \quad (2.16)$$

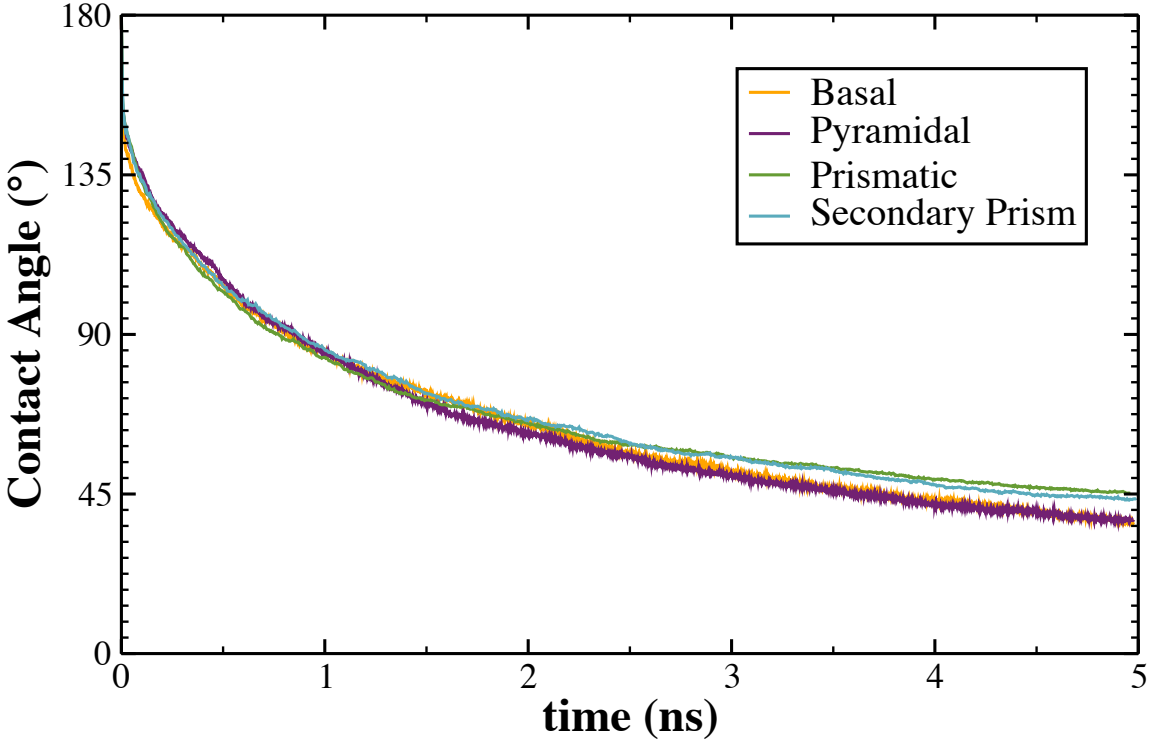


Figure 2.3. The dynamic contact angle of a droplet after approaching each of the four ice facets. The decay to an equilibrium contact angle displays similar dynamics. Although all the surfaces are hydrophilic, the long-time behavior stabilizes to significantly flatter droplets for the basal and pyramidal facets. This suggests a difference in hydrophilicity for these facets compared with the two prismatic facets.

where  $\tau_{liquid}$  and  $\tau_{wall}$  are the liquid and projected wall values of the decay constants,  $z_{wall}$  is the location of the interface, as measured by the structural order parameter. These values are shown in table 1 in the main text. Because the bins must be quite wide to obtain reasonable profiles of  $C_2(z, t)$ , the error estimates for the dynamic widths of the interface are significantly larger than for the structural widths. However, all four interfaces exhibit dynamic widths that are significantly below 1 nm, and are in reasonable agreement with the structural width above.

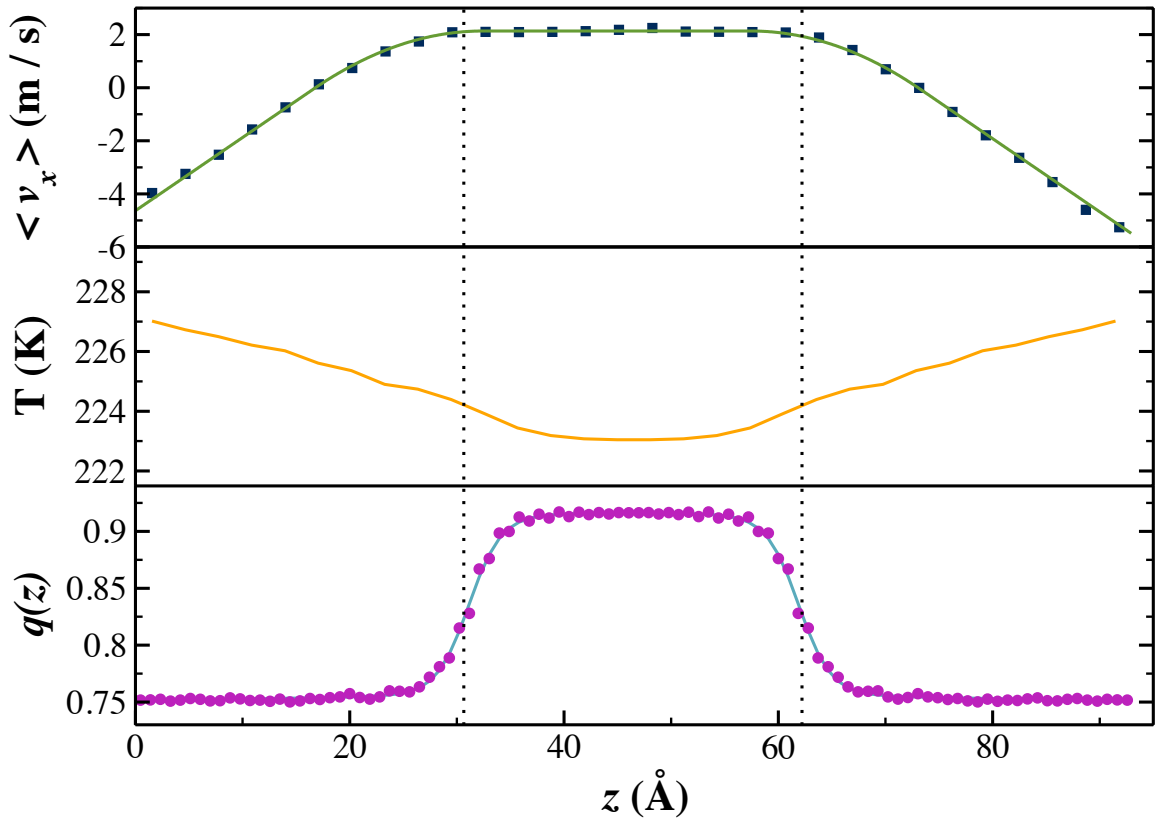


Figure 2.4. Properties of the pyramidal interface being sheared through water at  $3.8 \text{ ms}^{-1}$ . Lower panel: the local tetrahedral order parameter,  $q(z)$ , (circles) and the hyperbolic tangent fit (turquoise line). Middle panel: the imposed thermal gradient required to maintain a fixed interfacial temperature of 225 K. Upper panel: the transverse velocity gradient that develops in response to an imposed momentum flux. The vertical dotted lines indicate the locations of the midpoints of the two interfaces.

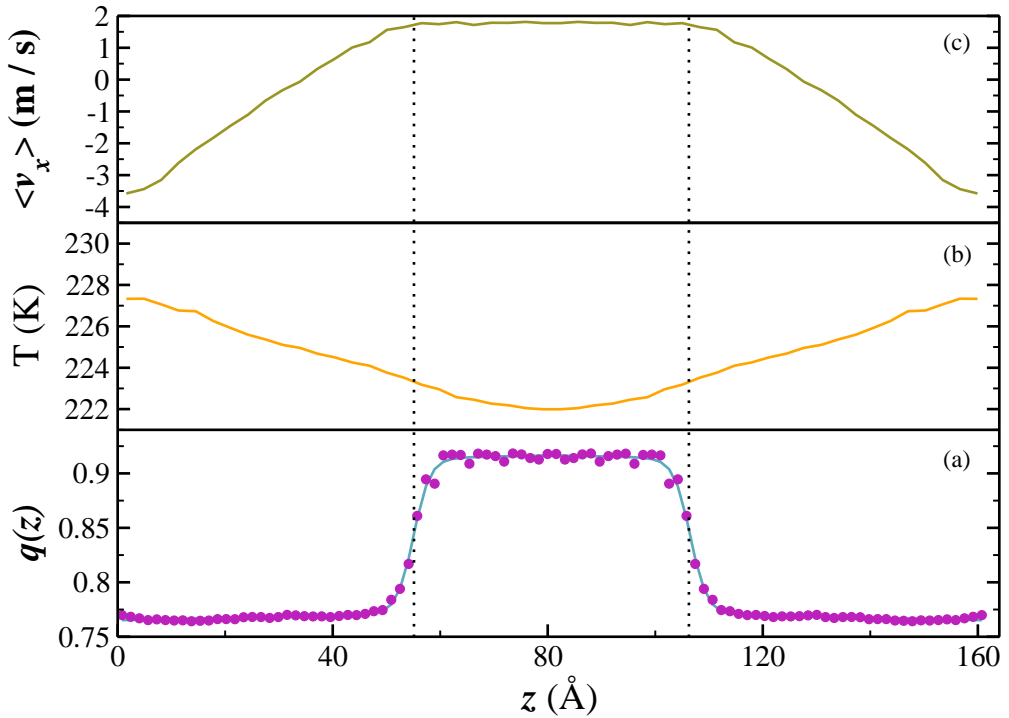


Figure 2.5. The secondary prism interface with a shear rate of  $3.5 \text{ ms}^{-1}$ .  
Panel descriptions match those in figure 3.8.

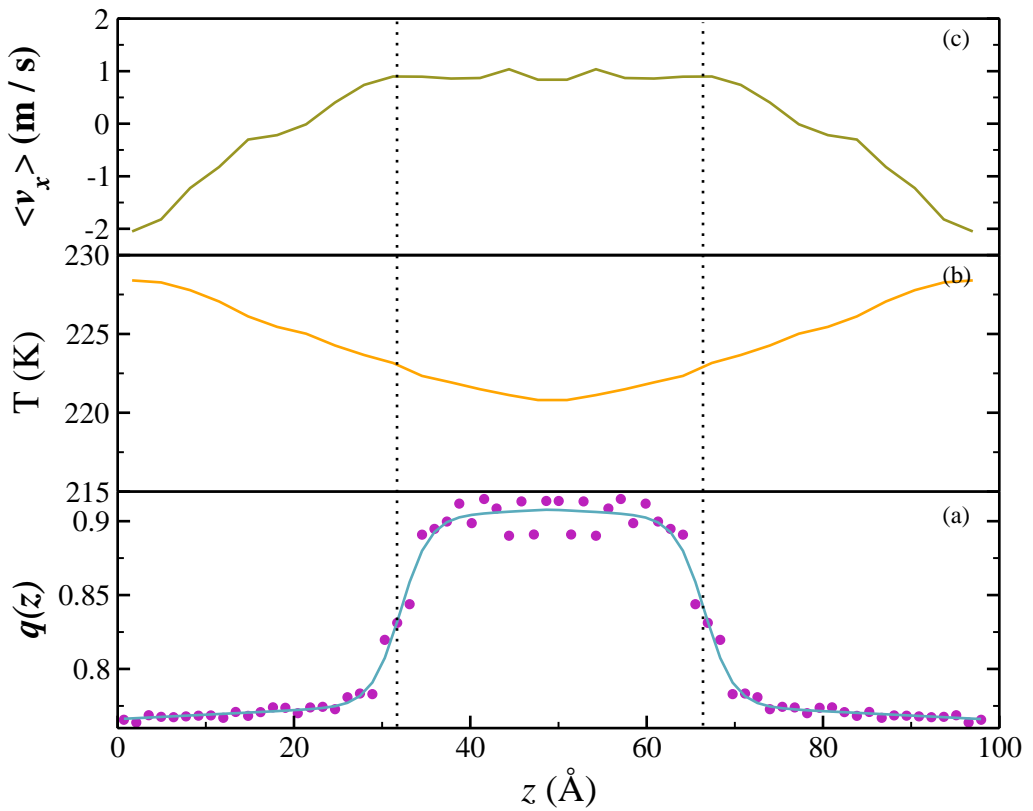


Figure 2.6. The basal interface with a shear rate of  $1.3 \text{ ms}^{-1}$ . Panel descriptions match those in figure 3.8.

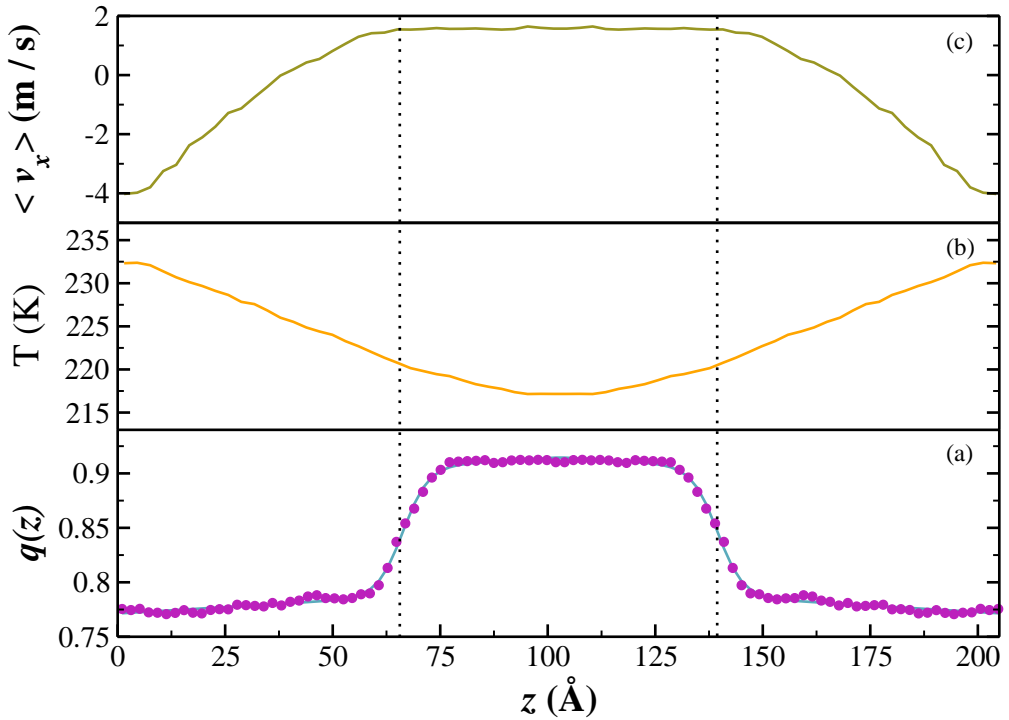


Figure 2.7. The prismatic interface with a shear rate of  $2 \text{ ms}^{-1}$ . Panel descriptions match those in figure 3.8.

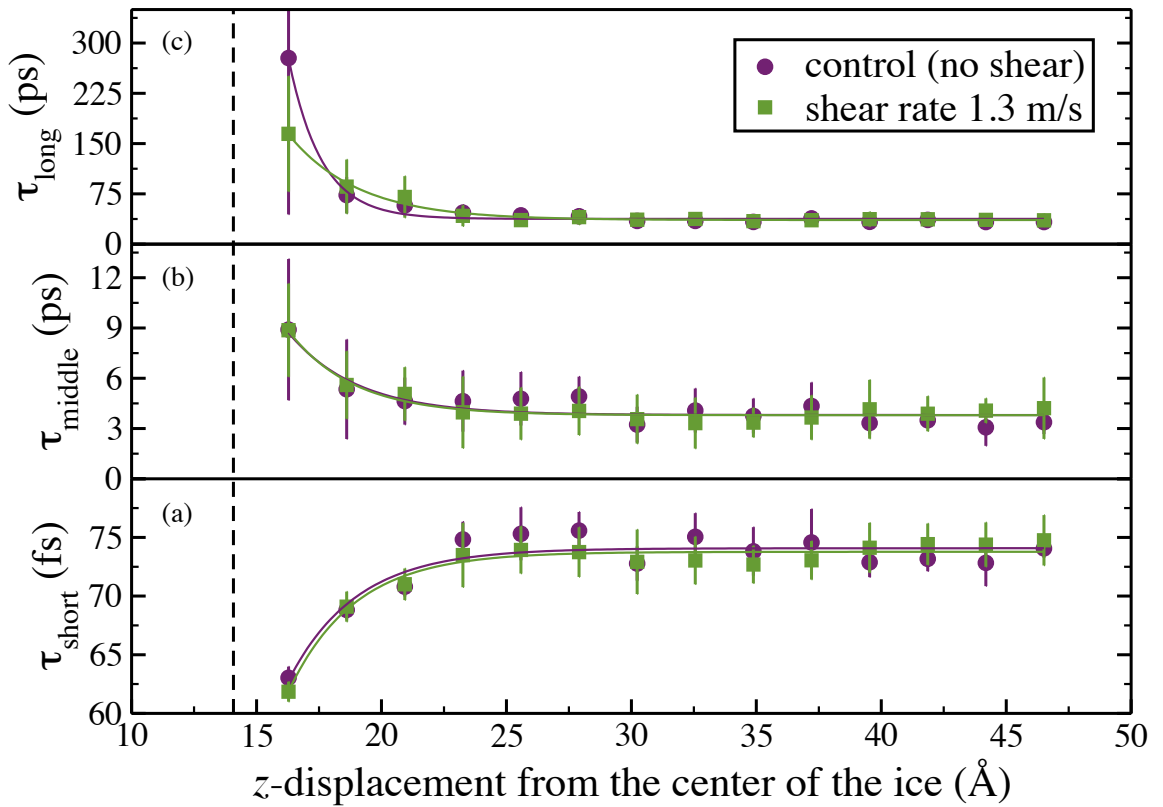


Figure 2.8. The three decay constants of the orientational time correlation function,  $C_2(z, t)$ , for water as a function of distance from the center of the ice slab. The vertical dashed line indicates the edge of the pyramidal ice slab determined by the local order tetrahedral parameter. The control (circles) and sheared (squares) simulations were fit using shifted-exponential decay (see Eq. 9 in Ref. ? ).

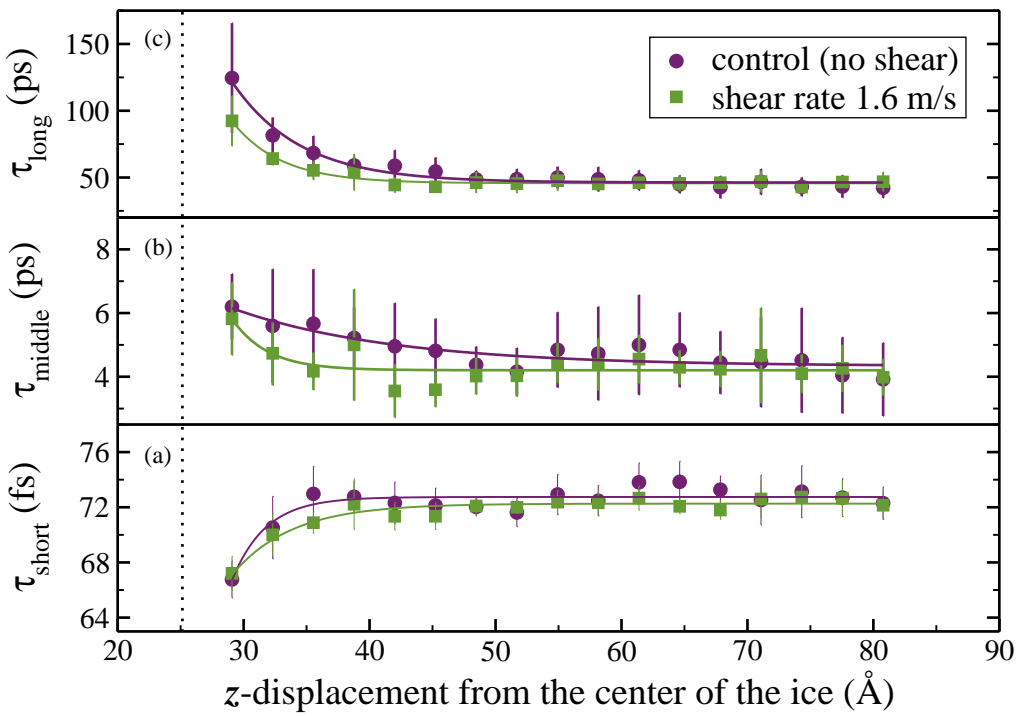


Figure 2.9. Decay constants for  $C_2(z, t)$  at the secondary prism face.  
Panel descriptions match those in 2.8.

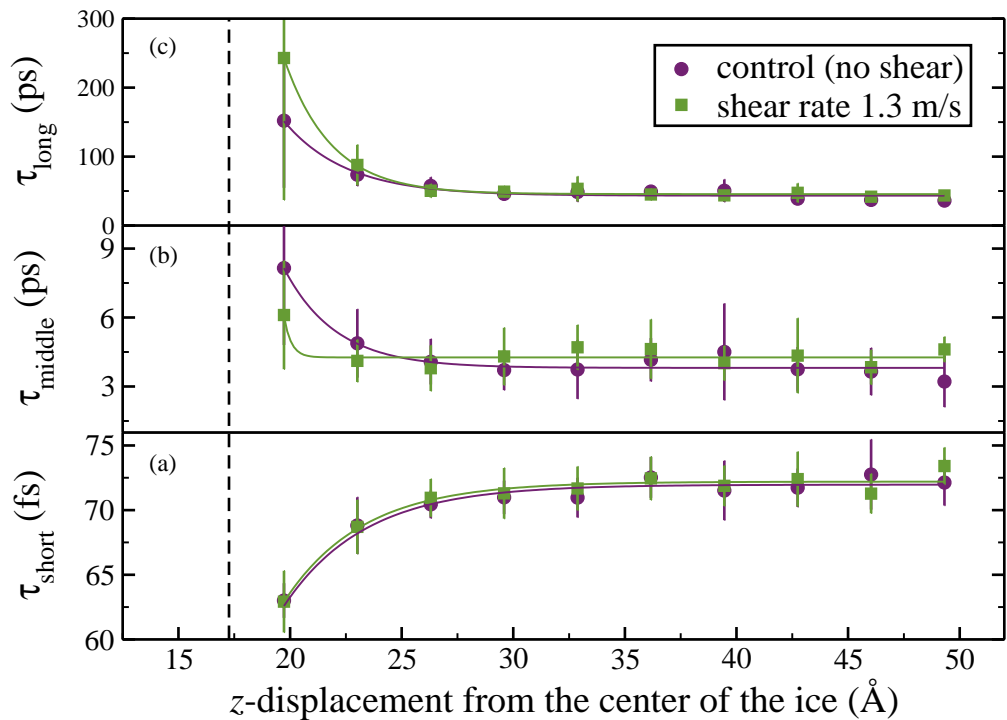


Figure 2.10. Decay constants for  $C_2(z, t)$  at the basal face. Panel descriptions match those in 2.8.

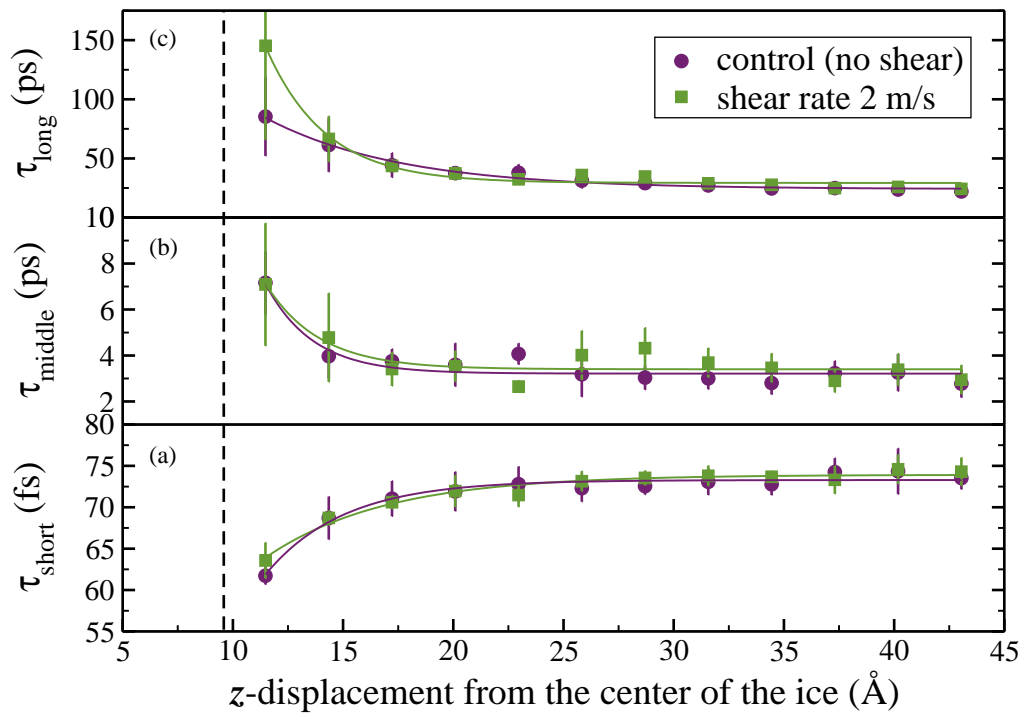


Figure 2.11. Decay constants for  $C_2(z, t)$  at the prismatic face. Panel descriptions match those in 2.8.

## CHAPTER 3

Friction at ice-I<sub>h</sub> / water interfaces is governed by solid-liquid hydrogen-bonding

We present evidence that the surface density of solid to liquid hydrogen bonds directly correlates with the solid/liquid friction of ice/water interfaces. Using non-equilibrium molecular dynamics simulations, the basal {0001}, prismatic {10̄10}, pyramidal {20̄21}, and secondary prism {11̄20} facets of ice-I<sub>h</sub> were drawn through liquid water with a momentum flux between the solid and liquid phases. Solid to liquid hydrogen bonds were identified using local tetrahedral ordering of the water molecules. An expression for friction coefficients appropriate for negative slip boundary conditions is presented, and the computed friction of these interfaces is found to be invariant to the shear rate and direction of shear relative to the surface features. Structural and dynamic interfacial widths for all four facets were found to be similar, and are also independent of the shear rate and direction. Differences in the solid to liquid hydrogen bond density are explained in terms of surface features of the four facets.

### 3.1 Introduction

Ice friction has been investigated extensively with a range of experiments to elucidate the role of temperature,<sup>1–6</sup> sliding speed,<sup>2, 4, 5</sup> applied load,<sup>1, 4, 7–9</sup> contact area,<sup>1, 10</sup> and moisture.<sup>11</sup> Kietzig *et al.* performed experiments on steel alloy rings sliding over a prepared ice surface.<sup>12</sup> They investigated the effect of surface nanopatterning, hydrophobicity, and surface structure of the ice-exposed slider on the ice/slider friction. Using laser irradiation, the slider surface hydrophobicity was

tuned without changing the chemical nature of the material. Kietzig showed that laser-induced hydrophobicity resulted in fewer capillary bridges forming between the slider and a thin film of melted ice. This reduced the amount of viscous shearing of the ice-melt, resulting in a lower friction coefficient. While ice friction experiments have focused on heterogeneous materials,<sup>1, 2, 4, 5, 9, 10, 12–14</sup> there have also been significant advances made on understanding ice-ice friction.<sup>7, 15–20</sup>

Experiments and computer simulations both suggest the existence of a quasi-liquid layer (QLL) that forms at the surface of ice at temperatures below the bulk melting point but above 235K.<sup>21–26</sup> The formation of this layer is driven by the termination of the periodic crystal structure. The surface molecules are not as tightly bound to their lattice positions as molecules in the underlying ice, and with sufficient thermal energy, these molecules reorient to maximize hydrogen bonding. At warmer temperatures, they can also translate along the surface.<sup>25, 27</sup> The existence of the QLL is now generally accepted as one of the reasons that ice displays a low coefficient of sliding friction.<sup>28–31</sup>

Generally, three distinct ice friction regimes have been found: boundary friction, mixed friction, and hydrodynamic friction, and the particular regime depends on the temperature and sliding velocity of the material.<sup>12, 14, 32–34</sup> The observed friction is the result of different physical processes in each regime. In boundary friction, the lubricating layer of ice melt is only a few molecules thick. This thin film is unable to support the sliding load, and friction can be attributed to surface asperities of the sliding material interacting with the ice surface itself.<sup>32</sup> In the mixed friction regime, the lubricating layer is thicker than in the boundary regime, but not yet sufficiently thick to maintain the sliding load. The QLL film reduces solid-solid adhesion at the interface, although the lubricating layer can also form capillary bridges with the material, resulting in a drag force.<sup>12, 14</sup>

If the liquid layer is thick enough to support the sliding load, the slider's surface

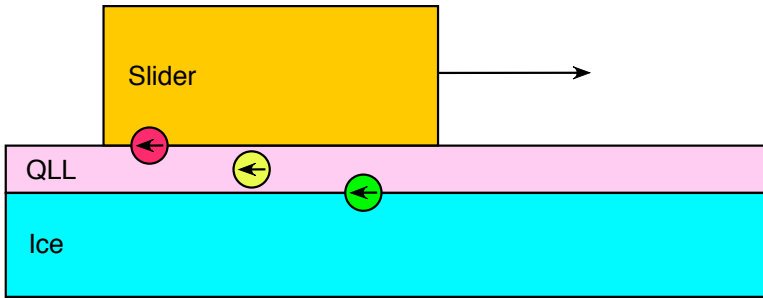


Figure 3.1. In the hydrodynamic regime, the friction felt by a slider on an ice surface is mediated by a quasi-liquid layer (QLL) that forms on the surface of the ice. There can be many contributions to this friction: capillary bridges between the material and the QLL (red), viscous drag in the liquid (yellow), and solid-liquid friction between the ice and the liquid film (green). This study concerns the last of the three contributions, the drag contributed by the ice-liquid interface.

asperities are no longer in contact with the surface and the observed friction may be due to the capillary bridges formed between the ice melt and the material. Under these conditions, the ice friction is classified as hydrodynamic friction.<sup>12, 14</sup> Thus the three regimes are characterized by the extent that a liquid-like layer of water mitigates the sliding load.

Kietzig *et al.* have outlined popular experimental techniques used to investigate the coefficients of friction for a variety of materials sliding on ice, as well as their sensitivity to temperature, slider load, contact area, wettability and hydrophobicity of the slider.<sup>14</sup> Of particular interest, the friction coefficients were found to increase with increasing slider velocity. This was attributed to three physical processes; adhesion forces between the slider's asperities and the ice surface, breaking of capillary bridges between the slider and the ice surface, and the viscous shearing of the ice melt across the ice surface. While teasing apart the individual contributions has proven challenging, Kietzig<sup>12</sup> and Persson<sup>33, 34</sup> have made significant progress. However, there is still very little known about water shearing over ice surfaces. Open questions

include: how does the structure of the interface change during this process, and what role does the presented crystal facet have in the observed friction?

To help understand slider-ice friction in the hydrodynamic regime, we have simulated the drag forces contributed by the interaction of the liquid water film with the underlying ice facet. This study uses non-equilibrium molecular dynamics (with an applied momentum flux) to create a shear flow at the ice/water interface. The magnitude of the momentum flux is then used to compute the solid-liquid friction for four different facets of ice that are presented to the liquid. We have previously used this technique to study solid-liquid friction for the basal and prismatic crystal facets where we observed significant facet-dependence, and noted surface corrugations that could contribute to these differences.<sup>35</sup> Here, we broaden the investigation to four common ice facets, we study significantly larger systems for significantly longer times, a wider range of shear rates, and we introduce a novel method for calculating solid-liquid friction coefficients under conditions of *negative* slip.

### 3.2 Methodology

#### 3.2.1 Construction of Ice / Water interfaces

Ice I<sub>h</sub> crystallizes in the hexagonal space group P6<sub>3</sub>/mmc, and ice crystals normally form hexagonal plates with the basal face, {0001}, forming the top and bottom of each plate, and the prismatic facet, {10̄10}, forming the sides. In extreme temperatures or low water saturation conditions, ice crystals can form hollow columns, needles, and dendrites, exposing other crystalline facets of the ice to the surroundings. Among the more commonly-observed facets are the secondary prism, {11̄20}, and pyramidal, {20̄21}, faces.

Although bulk ice I<sub>h</sub> is proton disordered, our simulations were carried out with proton-ordered, zero-dipole crystals that expose stripes of dangling H-atoms and

lone pairs. These initial configurations reproduce the surface features from Buch *et al.*<sup>36</sup> that helped interpret sum-frequency generation (SFG) experiments by the Schultz lab.<sup>37</sup> Our structures were created starting from Structure 6 of Hirsch and Ojamäe's set of orthorhombic representations for ice-I<sub>h</sub><sup>38</sup>. The primitive unit cell was replicated in all dimensions. The crystal was cleaved along the desired face, and two additional mutually perpendicular cuts were made. The crystal was reoriented so that the initial cut was normal to the *z*-axis of the simulation cell. The resulting structures were extended in *x* and *y* to form large exposed facets in rectangular box geometries.

Liquid water boxes were created with identical dimensions (in *x* and *y*) as the ice, with a *z* dimension of three times that of the ice block, and with a density corresponding to 1 g / cm<sup>3</sup>. Each of the ice slabs and water boxes were independently equilibrated to 50K and a pressure of 1 atm, and the resulting systems were merged by carving out any liquid water molecules within 3 Å of any atoms in the ice slabs. Each of the combined ice/water systems were then equilibrated to 225K, which is the liquid-ice coexistence temperature for SPC/E water<sup>39</sup>. The quiescent ice / water interfaces were then equilibrated for 10 ns, with 5 ns under a constant temperature (NVT) integrator set to the coexistence temperature (225K), followed by 5 ns under a microcanonical (NVE) integrator. During this time the ice was monitored for crystal growth or melting. We observed no advancement of the ice interface into the liquid, and no loss of crystallinity of the ice. Reference Louden<sup>2013</sup> contains a more detailed explanation of the construction of similar ice/water interfaces. The resulting dimensions as well as the number of ice and liquid water molecules contained in each of these systems are shown in Table 3.1. Note that the water molecules are not restrained in any way - molecules that start in the liquid phase may exchange with the ice (and vice versa).

TABLE 3.1

Sizes of the ice/water shearing simulations.

Interface	$N_{\text{ice}}$	$N_{\text{liquid}}$	$L_x$ (Å)	$L_y$ (Å)	$L_z$ (Å)
Basal {0001}	900	1846	23.87	35.83	98.64
Prismatic {10̄10}	3000	5464	35.95	35.65	205.77
Pyramidal {20̄21}	1216	2203	37.47	29.50	93.02
Secondary Prism {11̄20}	3840	8176	71.87	31.66	161.55

The SPC/E water model 40 has been extensively characterized over a wide range of liquid conditions 41, 42, and its phase diagram has been well studied 43–46. With longer cutoff radii and careful treatment of electrostatics, SPC/E mostly avoids metastable crystalline morphologies like ice-*i* 46 and ice-B 43, although Sanz *et al.* found that the stable polymorph for this model is likely ice-II at this temperature and 1 bar.<sup>45</sup> The free energies and melting points 39, 41, 43–50 of various other crystalline polymorphs have also been calculated. Haymet *et al.* have studied quiescent ice-I<sub>h</sub>/water interfaces using the SPC/E water model, and have seen structural and dynamic measurements of the interfacial width that agree well with both experimental results and more expensive water models, although the coexistence temperature for SPC/E is still well below the experimental melting point of real water 39. Given the extensive data and speed of this model, it is a reasonable choice even though the temperatures required are somewhat lower than real ice / water interfaces.

### 3.2.2 Creating shear in molecular simulations

The velocity shearing and scaling variant of reverse nonequilibrium molecular dynamics (VSS-RNEMD)<sup>42</sup> was employed to create shear in our simulation cells. This

method performs a series of simultaneous nonequilibrium exchanges of linear momentum and kinetic energy between two physically separated regions of the simulation cell. The system responds to this unphysical flux with velocity and temperature gradients. When VSS-RNEMD is applied to bulk liquids, transport properties like the shear viscosity,  $\eta$ , are easily extracted assuming a linear response between the applied flux,  $j_z(p_x)$ , and the resulting gradient,

$$j_z(p_x) = -\eta \left( \frac{\partial v_x}{\partial z} \right). \quad (3.1)$$

At interfaces between dissimilar materials, the same method can be used to extract *interfacial* transport properties (e.g. the hydrodynamic slip length or the interfacial thermal conductance). Because the individual VSS-RNEMD exchange moves conserve both total energy and linear momentum, the method can be “bolted on” to simulations in any ensemble. A more detailed explanation of VSS-RNEMD shearing simulations applied to ice / water interfaces can be found in our previous work.<sup>35</sup>

All simulations were performed using OpenMD 51, 52, with a time step of 2 fs and periodic boundary conditions in all three dimensions. When applicable, VSS-RNEMD moves were attempted every time step. This minimized the magnitude of individual momentum exchanges. For all simulations, electrostatics were handled using the damped-shifted force real-space electrostatic kernel.<sup>53</sup>

### 3.2.2.1 Shearing at ice / water interfaces

The RNEMD exchanges that force the solid to shear through a surrounding liquid do measurable work on the system, and this work causes frictional heating at the interface. Close to the melting point of the solid, this frictional heating may result in melting of the crystal. We are interested in the structure and dynamics of the interface at the coexistence temperature. Therefore, in order to prevent melting of

the ice phase, we have imposed a weak kinetic energy flux ( $J_z \sim 2.0 \times 10^{-6}$  kcal mol $^{-1}$  Å $^{-2}$  fs $^{-1}$ ) normal to the interface. The resulting thermal gradients (< 10 K over the length of the simulation box) were allowed to stabilize for 5 ns, and were found to be sufficient in keeping the interface within  $\pm 1$  K of the 225 K target during all shearing simulations.

Once thermal gradients had stabilized, linear momentum fluxes were imposed coincident with the kinetic energy flux. The resulting velocity gradients were allowed to stabilize for 1 ns before data collection began. Four successive 1 ns simulations were performed for each shear rate (varying from  $0.5 \rightarrow 10.0$  m s $^{-1}$ ). Configurations of the systems were stored every 1 ps, and statistics on the structure and dynamics were accumulated every 0.1 ps. Small variations in the measured interfacial widths between successive simulations were observed, but there was no indication of bulk melting or crystal growth. That is, no large scale changes in the positions of the top and bottom interfaces were observed during the simulations. A representative configuration of the solvated prismatic facet being sheared through liquid water is shown in Figure 3.2.

### 3.3 Results

#### 3.3.1 Structural measures of interfacial width under shear

One of the open questions about ice / water interfaces is whether the thickness of the interfacial ‘slush’ layer depends on the facet of ice presented to the water. In the interfacial region, the water molecules are ordered differently than in either the solid or liquid phases, and also exhibit dynamics unique to their local structure. The width of this interfacial layer has been estimated by finding the distance over which structural order parameters or dynamic properties change from their bulk liquid values to those of the solid ice. The properties used to find interfacial widths

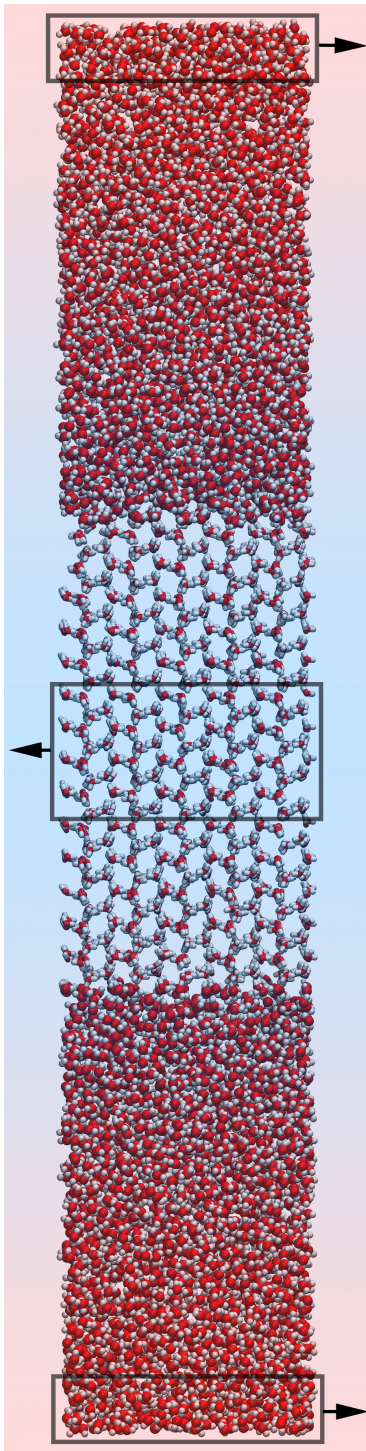


Figure 3.2. Computational model of a slab of ice being sheared through liquid water. The ice presents two copies of the prismatic  $\{10\bar{1}0\}$  facet towards the liquid phase. The RNEMD simulation exchanges both linear momentum (indicated with arrows) and kinetic energy between the central box and the box that spans the cell boundary. The system responds with weak thermal gradient and a velocity profile that shears the ice relative to the surrounding liquid.

have included the local density, the diffusion constant, and both translational and orientational order parameters 35, 39, 47, 54–57.

Because the VSS-RNEMD method creates thermal and velocity gradients in the system, the momenta of the water molecules are perturbed, and order parameters that depend on translational motion may measure the momentum exchange and not physical properties of the interface. As a structural measure of the interface, we have used the local tetrahedral order parameter, which compares the local molecular environments (e.g. the angles between nearest neighbor molecules) to perfect tetrahedral ordering. This quantity was originally described by Chau and Hardwick, 58 was rescaled by Errington and Debenedetti, 59 and has been used in bulk liquid simulations by Kumar *et al.* 60 It has also previously been used in ice/water interfaces by Bryk and Haymet 44, and in our initial work on ice / water interfaces35.

We have evaluated the local tetrahedral order parameter,  $q$ , along the coordinate perpendicular to the ice / water interface, i.e., the  $z$ -axis of the simulation box.

$$q(z) = \frac{1}{N_z} \int_0^L \sum_{i=1}^N \left( 1 - \frac{9}{2n(n-1)} \sum_{j=1}^{n-1} \sum_{k=j+1}^n \left( \cos \psi_{jik} + \frac{1}{3} \right)^2 \right) \delta(z_i - z) dz \quad (3.2)$$

$\psi_{jik}$  is the angle formed between the oxygen sites of water molecules  $i$ ,  $j$ , and  $k$ , where molecule  $i$  is the central water molecule and molecules  $j$  and  $k$  are two of the  $n$  neighbors of  $i$ . Molecules  $j$  and  $k$  lie within the first solvation shell of molecule  $i$  ( $r < 3.41$  Å for water), and the double sum visits all angles for neighbors of molecule  $i$  that are within this distance. When molecule  $i$  has exactly four neighbors ( $n = 4$ ), the prefactor reduces to 3/8, as in the expression of Errington and Debenedetti, but Eq. (3.2) also provides tetrahedrality information for water molecules that are either under- or over-coordinated. We have also introduced the normalization factor  $N_z = \sum_i \int \delta(z_i - z) dz$  to account for the varying populations of water molecules within each finite-width bin.

At low temperatures, the tetrahedral order parameter can approach unity for perfect ice-I<sub>h</sub> structures. However, at temperatures close to melting, values of 0.9 are more common due to thermal motion in the lattice. In liquid water, overlap of the local environment with a perfect tetrahedron is reduced, and values of  $q(z) \approx 0.75$  are common at 225 K.

The structural widths of the ice / water interfaces were determined by dividing each system into 1 Å bins along the  $z$ -axis, and computing statistical averages of  $q(z)$  in each bin. For the secondary prism interface, the resulting distribution can be seen in the bottom panel of Fig. 3.3 (and in the Supporting Information for the other interfaces). In the bulk liquid (at small and large values of  $z$ ), the order parameter takes on values of  $q(z) \approx 0.77$ , while  $q(z) \approx 0.92$  was found in bins spanning the ice. The tetrahedrality profiles were fit using a function that captures the smooth transition from the bulk liquid to ice (turquoise line in the bottom panel of the same figures),

$$q(z) \approx q_{\text{liq}} + \frac{q_{\text{ice}} - q_{\text{liq}}}{2} \left[ \tanh\left(\frac{z-l}{w}\right) - \tanh\left(\frac{z-r}{w}\right) \right] + \beta \left| z - \frac{r+l}{2} \right|. \quad (3.3)$$

Here  $q_{\text{liq}}$  and  $q_{\text{ice}}$  are the values of the order parameter for the bulk liquid and ice domains. The locations  $l$  and  $r$  are the  $z$ -coordinates of the Gibbs dividing surface for the left and right interfaces (shown in Fig. 3.3 with vertical dotted lines), and  $w$  is the interfacial width. The last term in Eq. (3.3) accounts for the influence of the weak thermal gradient on the tetrahedrality profile in the liquid region. Namely, at warmer temperatures the liquid is able to adopt local configurations resulting in lower values of the order parameter. This results in a small linear decay in the tetrahedrality profiles for increasing displacements from the ice surface.

In the middle panel of Fig. 3.3, we show the resulting thermal gradient from the imposed kinetic energy flux. At the ice / water interface, the local temperature is

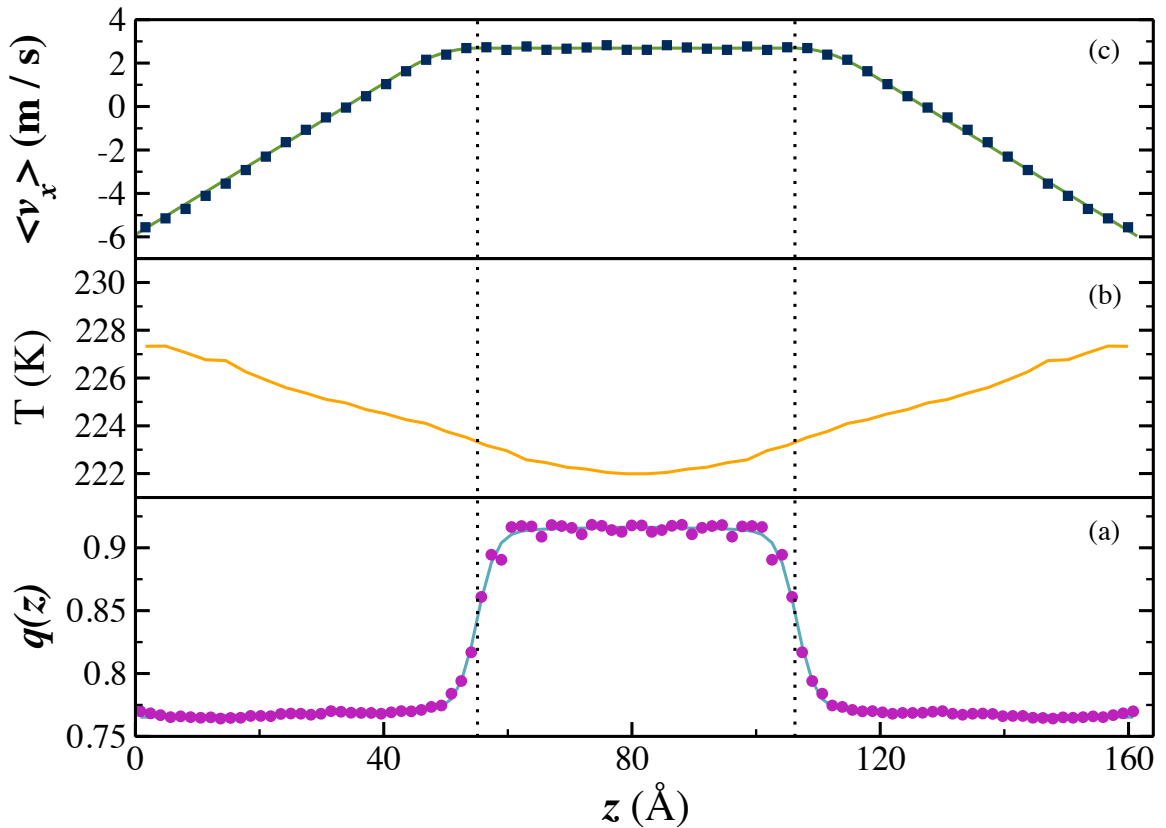


Figure 3.3. Properties of the secondary prism interface being sheared through water at  $8.6 \text{ ms}^{-1}$ . Lower panel: the local tetrahedral order parameter,  $q(z)$ , (circles) and the hyperbolic tangent fit (turquoise line). Middle panel: the imposed thermal gradient required to maintain a fixed interfacial temperature of 225 K. Upper panel: the transverse velocity gradient (squares) that develops in response to an imposed momentum flux, along with the fit (green line). The vertical dotted lines indicate the locations of the Gibbs dividing surfaces of the two interfaces.

held at approximately 225 K, allowing investigation of the response to the shear while maintaining solid-liquid coexistence. In the top panel, the velocity gradient resulting from the imposed momentum flux shows that the ice has a uniform positive velocity along the  $x$  axis. The bulk liquid at the ends of the simulation cell has negative velocity, although the center of mass of the simulation box is stationary. The bulk fluid shows a primarily linear velocity gradient allowing for easy calculation of the shear viscosity. Close to the interface, the ice imparts significant positive momentum into the surrounding interfacial liquid. Projections of the velocity gradient from the liquid onto the Gibbs dividing surface indicate that the ice-water interface is in the negative slip regime.

From Eq. (3.3), we have obtained estimates for  $w$ , the structural widths of the interfaces for the quiescent ice / water systems. These values are related to the 10% – 90% interfacial widths commonly reported in previous studies ( $w_{10-90} = 2.197 w$ ).<sup>39, 44</sup> We find  $w_{10-90} \approx 7 \text{ \AA}$  for each of the interfaces as seen in Table 3.2. These values are similar to our previous findings for the 10% – 90% interfacial widths obtained from shorter simulations, ( $7.0 \pm 0.9 \text{ \AA}$ ) for the basal and ( $7.9 \pm 0.4 \text{ \AA}$ ) for the prismatic interfaces.<sup>35</sup> Over the range of shear rates investigated,  $\sim 0.5 - 10.0 \text{ m s}^{-1}$ , we find no significant differences in the interfacial widths for any of the crystal faces. All values of  $w_{10-90}$  obtained from shearing simulations fell inside the error bars of the values obtained from the quiescent simulations.

These values agree well with those reported by Haymet *et al.*<sup>39, 44, 54–57</sup> Using a variety of water models and several different order parameters, they have estimated the ice / water interface to be between 5  $\text{\AA}$  and 18  $\text{\AA}$  depending on the particular interface and means of measure. For the SPC/E model, they found the basal and prismatic ice / water interface to be  $\approx 11 \text{ \AA}$  wide from translational and window-averaged density order parameters. The interfacial widths were also estimated by

TABLE 3.2

Structural and dynamic properties of the interfaces of Ice-I<sub>h</sub> with water.

Interface	$w_{10-90}$ (Å)	$d_{10-90}$ (Å)	$\kappa$ (amu Å <sup>-2</sup> fs <sup>-1</sup> )	$\rho_{sl}$ (Å <sup>-2</sup> )
Basal {0001}	$7.5 \pm 0.4$	$5 \pm 1$	$0.31 \pm 0.03$	$0.1227 \pm 0.0003$
Prismatic {10̄10}	$7.2 \pm 0.2$	$8 \pm 2$	$0.48 \pm 0.04$	$0.2014 \pm 0.0005$
Pyramidal {20̄21}	$6.6 \pm 0.2$	$6 \pm 1$	$0.26 \pm 0.02$	$0.0866 \pm 0.0003$
Secondary Prism {11̄20}	$6.7 \pm 0.2$	$7 \pm 1$	$0.41 \pm 0.02$	$0.1384 \pm 0.0004$

observing the transition of a similar tetrahedral order parameter from their ice-like value of 0.9 to the bulk liquid value of 0.6. This gave estimates of  $\approx 11$  Å, somewhat larger than our current estimates.

### 3.3.2 Solid-liquid friction at ice/water interfaces

In no-stick boundary conditions, fluid flowing over a solid is characterized by a slip length,  $\delta$ , describing the extent of slip of the fluid at the interface. This length is the extrapolated distance from the interface where the tangential velocity component vanishes. For solids with weak interactions with the liquid, there is little drag imposed on the fluid and the resulting interfacial liquid velocity,  $\Delta v_{\text{slip}}$ , can be significant. In no-stick boundaries, therefore, the extrapolated slip lengths are also large (top panel of Fig. 3.4). Balasubramanian and Mundy have related the slip length to the interfacial friction coefficient,

$$\lambda = \frac{\eta}{\delta} \quad (3.4)$$

where  $\eta$  is the shear viscosity of the liquid.<sup>61</sup>

For solids that have strong interactions with the liquid, a larger frictional drag is

imposed on the fluid at the interface and the resulting slip lengths are smaller. When the solid-liquid interactions become large enough, the interface is best described with stick boundary conditions, and the slip length will vanish (middle panel of Fig. 3.4). Stick boundaries pose a problem for Eq. (3.4), as  $\lambda$  asymptotically goes to infinity as  $\delta \rightarrow 0$ . Likewise, some materials possess solid-liquid interactions that are strong enough for the extrapolated tangential velocity to vanish *before* reaching the solid. The velocity profile yields a negative slip length (bottom panel of Fig. 3.4), and the solid-liquid friction coefficient defined in Eq. (3.4) becomes meaningless. Ice shearing through liquid water is in the negative slip limit. The tangential velocity profile of the liquid extrapolates to zero several molecular layers before reaching the solid. Thus a new friction coefficient must be defined to describe these interfaces.

The solid-liquid friction coefficient may also be defined using the velocity drop across the interface, rather than the length scale over which this drop occurs. We can relate the imposed shear stress with the relative tangential velocity of the fluid in the interfacial region,<sup>42</sup>

$$j_z(p_x) = \kappa \Delta v \quad (3.5)$$

where  $\Delta v = v_x(\text{solid}) - v_x(\text{liquid})$  is the difference in transverse velocity between points that are unambiguously on the solid and liquid sides of the interface. In slip boundary conditions,  $\kappa$  and  $\lambda$  are identical, but Eq. (3.5) provides a direct analogy to non-equilibrium expressions for the interfacial thermal conductance ( $G$ ),

$$J_z = G \Delta T. \quad (3.6)$$

Here,  $J_z$  is a thermal flux and the temperature drop is measured across an interface of *finite width*. By analogy,  $\kappa$  is a transport coefficient that measures interfacial momentum conductance.

In ice/water interfaces, the solid-liquid boundary is not an infinitely thin plane.

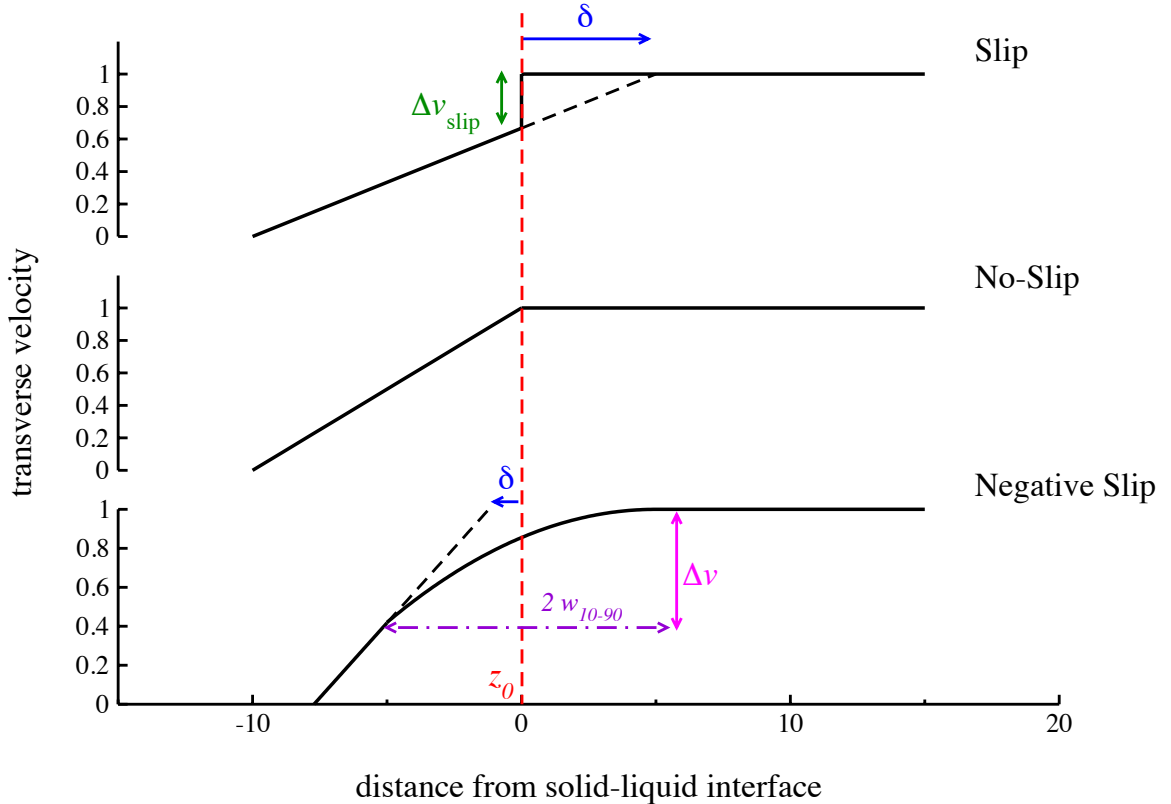


Figure 3.4. Transverse velocity profiles,  $v_x(z)$ , for interfaces in slip (top), no-slip (middle), and negative slip boundary conditions (bottom). The location of the interface is defined by a Gibbs dividing surface at  $z_0$ . Under negative slip conditions, the 10-90 interfacial width,  $w_{10-90}$ , provides locations that are unambiguously on the liquid and solid sides of the interface.

An order parameter (the tetrahedrality) goes smoothly between the phases over a few molecular diameters. We can use this order parameter to find the interfacial width and define locations in space that are unambiguously on the solid and liquid sides of the interface. In what follows, we have used the Gibbs dividing surface ( $z_0$ ) and the 10–90 width of the interface ( $w_{10-90}$ ) to arrive at physical locations for measuring  $v_x(\text{solid})$  and  $v_x(\text{liquid})$ . These uniquely define a friction coefficient in terms of well-defined structural features ( $z_0$  and  $w_{10-90}$ ) and dynamic properties ( $v_x(z)$ ) of the interface.

Tangential velocity profiles from the simulations were fit using a piecewise function that is both continuous and continuously differentiable (see Supporting Information). To arrive at estimates of the interfacial velocities, these fits were queried at locations on either side of the structural Gibbs dividing surface,

$$v_x(\text{solid}) = v_x(z_0 + w_{10-90})$$

$$v_x(\text{liquid}) = v_x(z_0 - w_{10-90}).$$

The momentum flux,  $j_z(p_x)$  is an imposed parameter of the VSS-RNEMD simulations, and by using Eq. (3.5), estimates of interfacial friction coefficient  $\kappa$  are straightforward.

The calculated  $\kappa$  values found for the four crystalline facets of ice-I<sub>h</sub> investigated here are shown in Table 3.2. These results were found to be independent of the shear rate, as well as the direction of the shear relative to the features on the surfaces of the facets.

Note that the values of  $\kappa$  for the basal and prismatic crystal facets in Table 3.2 disagree with values for interfacial friction ( $\lambda$ ) we previously reported.<sup>35</sup> In our initial report, the expression for the coefficient of friction was derived from equation (3.4) and the linear constitutive relation for shear stress in a bulk fluid. However, as

described above, sheared ice/water interfaces are in the domain negative slip lengths. Eq. (3.4) should only be used in slip boundary conditions, as negative slip can yield coefficients of friction that appear to be smaller in magnitude than the zero slip conditions. In our previous work, the prismatic surface was found to have a larger negative slip length than the basal face, indicating a prismatic surface that should have been reported with a larger coefficient of friction. If one instead uses Eq. (3.5) and interfacial widths to compute friction, the reported values come into agreement.

### 3.3.3 Dynamic measures of interfacial width under shear

The spatially-resolved orientational time correlation function,

$$C_2(z, t) = \langle P_2(\mathbf{u}_i(0) \cdot \mathbf{u}_i(t))\delta(z_i(0) - z)\rangle, \quad (3.7)$$

provides local information about the decorrelation of molecular orientations in time. Here,  $P_2$  is the second-order Legendre polynomial, and  $\mathbf{u}_i$  is the molecular unit vector that bisects the HOH angle of molecule  $i$ . The angle brackets indicate an average over all the water molecules and time origins, and the delta function restricts the average to specific regions in the  $z$ -dimension.

Recently, Laage and Hynes have determined the mechanism for water reorientation.<sup>62, 63</sup> Using molecular dynamics simulations, they found that water reorients by breaking a hydrogen bond with an overcoordinated first-shell neighbor, and makes a large angle jump to form a new hydrogen bond with an undercoordinated second-shell neighbor. The hydrogen bond cleavage and molecular reorientation occur in a concerted fashion, not in successive steps as was previously thought. With this detailed picture, they constructed the Extended Jump Model<sup>62, 63</sup> based on the Ivanov Jump Model and parameters extracted from their molecular simulations; the average jump amplitude of the rotational jump,  $\theta_0$ , and the frequency of the jumps,  $1/\tau_0$ . After

accounting for molecular frame reorientation, the Extended Jump Model is able to predict reorientation relaxation times,  $\tau_n^{jump}$ , which agree with experimental results as well as estimates obtained from simulations where fast librational motion is ignored.

In the ice crystal, decay of  $C_2(z, t)$  is incomplete, while in the liquid, correlation times are typically measured in ps. Observing the spatial-transition between the decay regimes can define a dynamic measure of the interfacial width. To determine the dynamic widths of the interfaces under shear, each of the systems were divided into bins along the  $z$  axis ( $\approx 1 \text{ \AA}$  wide) and  $C_2(z, t)$  was computed using only those molecules that were in the bin at the initial time. For each ice / water interface investigated, the following 0.5 ns simulations were computed: quiescent simulations (where no thermal or momentum gradient was present), simulations with only a thermal gradient present, and simulations where both thermal and momentum gradients were present. During these simulations, the positions and orientations of each molecule were recorded every 100 fs.

Computed  $C_2(z, t)$  values have previously been fit to a triexponential decay, with three time constants:  $\tau_{\text{short}}$ , measuring the librational motion of the water molecules,  $\tau_{\text{middle}}$ , measuring the timescale for the large angle jumps during the breaking and making of hydrogen bonds, and  $\tau_{\text{long}}$ , corresponding to the translational motion of the water molecules.<sup>35</sup> The Extended Jump Model also includes three similar decay constants, however two of them are linked and the dynamics of the decay is governed by two parameters. Since we are interested in how the decay times and the individual contributions may change through the interface, we have fit the  $C_2(z, t)$  data with

$$C_2(z, t) = a e^{-t/\tau_{\text{short}}} + b e^{-t/\tau_{\text{middle}}} + (1 - a - b) e^{-t/\tau_{\text{long}}} \quad (3.8)$$

where all of the decay constants are considered local functions of the  $z$  coordinate. In Fig. 3.6, the  $z$ -coordinate profiles for the three decay constants,  $\tau_{\text{short}}$ ,  $\tau_{\text{middle}}$ , and  $\tau_{\text{long}}$

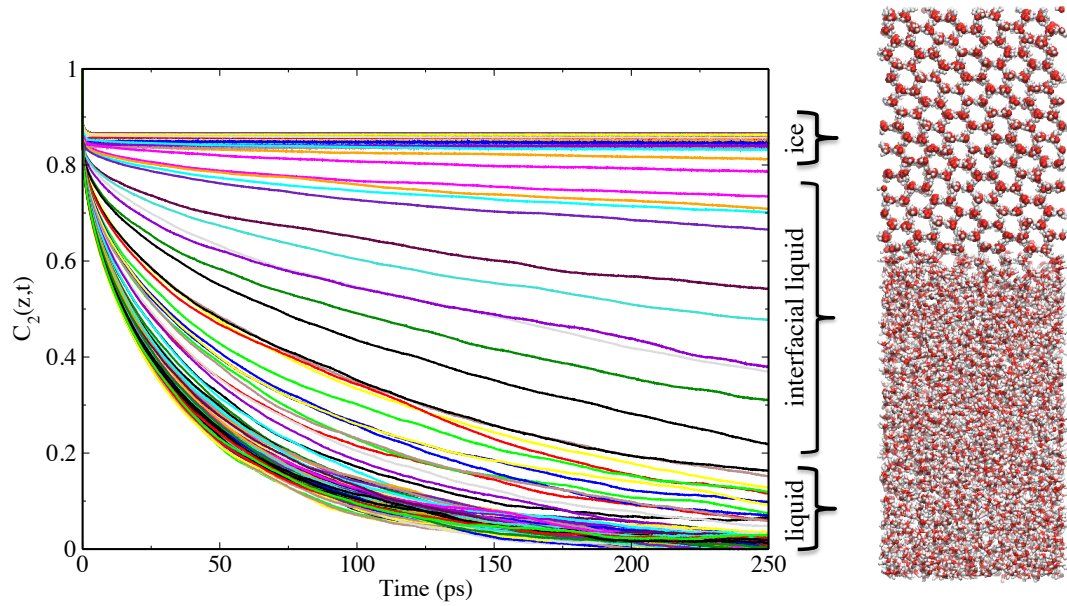


Figure 3.5.  $C_2(z,t)$  collected in  $1 \text{ \AA}$  bins across the secondary prism ice/water interface. The band that experiences very little decay represents water molecules in the ice, while the band that decays quickly corresponds to bins in the liquid. The correlation function presents a continuous distribution of decay behaviors across the interface between ice and liquid water.

for the secondary prism interface is shown, along with their fractional components of the overall total decay, ( $a$ ,  $b$ ,  $1 - a - b$ ), respectively. Similar figures for the other interfaces are provided in the Supporting Information.

In the liquid regions of all four interfaces,  $\tau_{\text{middle}}$  and  $\tau_{\text{long}}$  consistently approach 3–6 ps and 30–40 ps, respectively. Both of these times increase closer to the interface. Conversely,  $\tau_{\text{short}}$  decreases from a liquid-state value of 72 – 76 fs approaching the interface.

The fractional contributions of the three motions to the overall decay changes as we approach the interface as well. Far from the ice, the librational motion and hydrogen bond breaking/making events each contribute to about 20 percent of the total decay, whereas frame reorientation contributes about 60 percent. As we approach the interface, the librations and hydrogen bond dynamics both decrease in contribution. The librations comprise approximately 15 percent of the overall decay at the edge of the interface, whereas the hydrogen bond contributions drop to approximately zero. In contrast, the fraction of the total decay due to frame reorientation is shown to increase approaching the interface. The time constant corresponding to this motion is seen to logarithmically increase as we approach the interface as the molecules become more ice-like. In the ice we would expect molecular reorientation to be incomplete, however, at the interface we observe frame reorientation to contribute 85 percent of the overall decay.

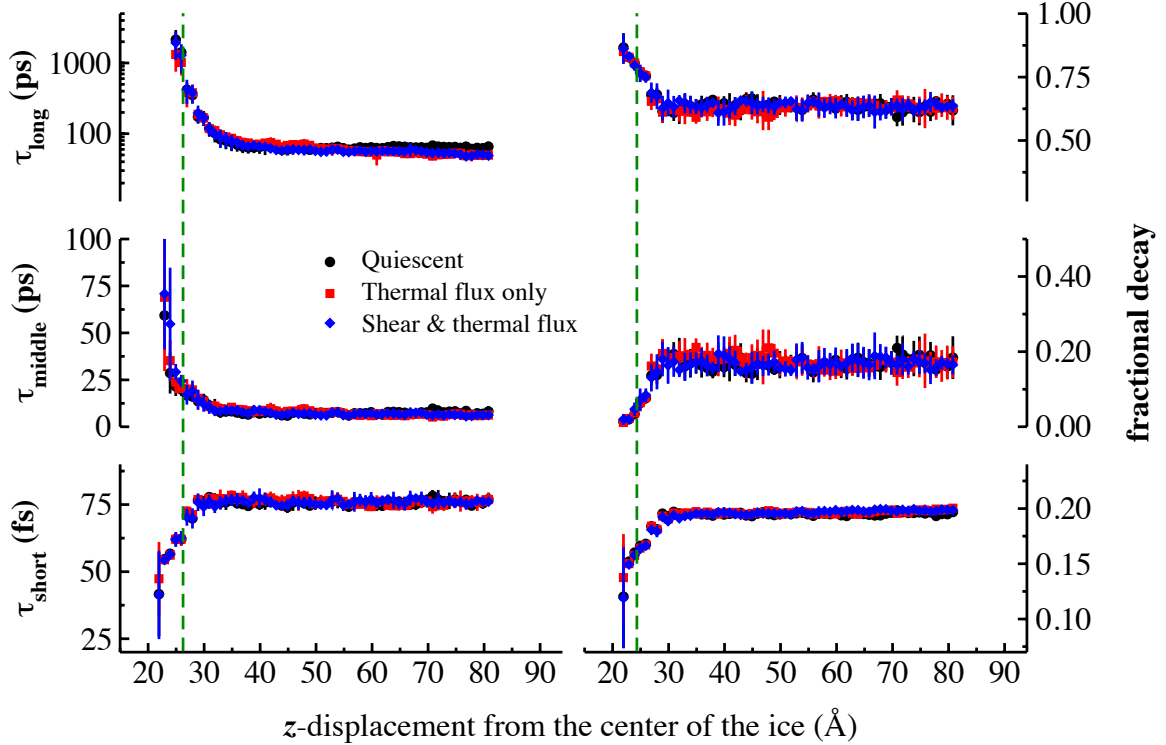


Figure 3.6. Decay times (left) for  $C_2(z, t)$  at the secondary prism interface, and their fractional contributions to the overall decay (right) fit using Eq. (3.8). The local decay constants are plotted as a function of distance from the center of the ice slab. The vertical dashed line indicates the Gibbs dividing surface determined using the local tetrahedral order parameter.

Results are shown for a quiescent system with no applied kinetic or momentum flux (black), an interface with an imposed kinetic energy flux (red), and a sheared simulation (blue) with both kinetic and momentum fluxes.

We have estimated a dynamic interfacial width by fitting the profiles of all the three orientational time constants with an exponential decay to the bulk-liquid behavior,

$$\tau(z) = \tau_{\text{liquid}} + (\tau_{\text{wall}} - \tau_{\text{liquid}})e^{-(z-z_0)/d} \quad (3.9)$$

where  $\tau_{\text{liquid}}$  and  $\tau_{\text{wall}}$  are the liquid and projected interfacial values of the decay constants,  $z_0$  is the location of the Gibbs dividing surface, as measured by the structural order parameter. As with the structural widths, 10% – 90% dynamic widths are

easily computed from the fits ( $d_{10-90} = 2.197$   $d$ ). These values are provided in Table 3.2. All four interfaces exhibit dynamic widths that are  $\sim 6$  Å, and are in reasonable agreement with the structural widths above.

We note that Bryk and Haymet also calculated the orientational time correlation function at the basal interface of SPC/E water,<sup>39</sup> and observed the same qualitative trend through the ice / water interface, although the spatial resolution was not sufficient to resolve a dynamic width.

Laage and Hynes investigated how water molecules reorient around ions<sup>64–67</sup>, proteins<sup>68</sup>, and in confined spaces<sup>69, 70</sup>. They also studied how the strength of the hydrogen bond might perturb the reorientation dynamics,<sup>71</sup> and found the librational motion which forms a cone around the O-O vector is smaller for more strongly hydrogen bonded water. This may also provide a partial explanation for the increasing contribution of short time decay very close to the ice surfaces. Since the solid creates an excluded volume for the water molecules that are in proximity to the interface, the hindered range of motion (i.e., a smaller cone around the O-O vector) manifests as faster librational decay.

### 3.4 Discussion

The primary result of this paper is the observation that the different facets of ice-I<sub>h</sub> produce significantly different solid-liquid interfacial friction coefficients with water (see Table 3.2). The two prismatic surfaces displayed the largest coefficients of friction, while the basal and pyramidal facets exhibited significantly lower friction.

The differences in friction are surprising given that densities and molecular interactions are identical for the four interfaces and the interfacial widths measured via both structural and dynamic features are also nearly the same. There are few remaining surface properties that could give rise to differences in solid-liquid friction of the four facets, notably surface corrugation and hydrogen bonding density at the

interface. In this section we investigate the roles of these surface features.

### 3.4.0.1 Solid-liquid hydrogen bond density

One reason for the observed differences in friction coefficients is that ice surfaces may yield different densities of hydrogen bonds that bridge the solid and liquid. An ice surface that forms more hydrogen bonds with the interfacial liquid would be able to exert significant lateral forces on the liquid layer, yielding a larger friction coefficient. To probe this possibility, we have investigated the density of cross hydrogen bonds between the ice and the liquid.

Quantifying water molecules as “ice” or “liquid” at an interface of finite width requires a local order parameter for separating the molecules. We have again chosen the tetrahedral order parameter,  $q$  and the value of at the Gibbs dividing surface ( $q(z_0) \approx 0.84$ ) as our partitioning criterion. Note that some molecules have strong tetrahedral ordering in the liquid phase, so this segregation will not yield perfect division between ice and liquid phase molecules.

To determine if a hydrogen bond has been formed between two water molecules, we used the geometric criteria of Luzar and Chandler.<sup>72</sup> We identify a hydrogen bond between two water molecules if their oxygen sites are within  $r_{OO} < 3.5$  Å and the OHO bond angle is within  $\theta_{OHO} < 30$  degrees.

For each of the shearing simulations performed above, a hydrogen bond tetrahedrality matrix was constructed. Snapshots from the shearing trajectories were taken every 0.1 ps, and the tetrahedrality ( $q$ ) value for each water molecule in the system was calculated. Hydrogen bonds were also identified, and the tetrahedrality of the donor ( $q_D$ ) and acceptor ( $q_A$ ) molecules were recorded. A probability density of hydrogen bonds categorized by donor and acceptor tetrahedrality,  $\rho_{\text{HB}}(q_D, q_A)$ , was then recorded.

The lower panel of Fig. 3.7 shows a hydrogen bond tetrahedrality distribution for the prismatic facet with  $q_D$  plotted along the  $x$ -axis and  $q_A$  along the  $y$ -axis. Population around  $q_D \approx q_A \approx 0.9$  indicates the density of ice-ice hydrogen bonds in the system, while the liquid-state hydrogen bonds are concentrated in the lower left, and are significantly more diffuse. The off-diagonal regions of the distribution represent the population of molecules in tetrahedral (ice-like) environments bound to non-tetrahedral (liquid-like) environments. Integrating the population found in each of these regions and normalizing by the surface area of each ice crystal produces a surface density of hydrogen bonds ( $\text{\AA}^{-2}$ ) formed between the ice and interfacial liquid,

$$\rho_{sl} = \frac{N_{\text{HB}}}{2L_x L_y} \left[ \int_0^{0.84} dq_D \int_{0.84}^1 dq_A \rho_{\text{HB}}(q_D, q_A) + \int_0^{0.84} dq_A \int_{0.84}^1 dq_D \rho_{\text{HB}}(q_D, q_A) \right] \quad (3.10)$$

$N_{\text{HB}}$  is the total number of hydrogen bonds found in the system, and  $L_x$  and  $L_y$  are the dimensions of the two ice facets exposed to the liquid. Values for  $\rho_{sl}$  for each of the ice surfaces are reported in Table 3.2.

The trend in surface density of solid-liquid hydrogen bonds reproduces the trend in the friction coefficients, indicating that friction at ice-I<sub>h</sub> water interfaces is strongly influenced, if not governed, by the number of solid-liquid hydrogen bonds that can be formed. This result is robust under multiple shear rates and orientation of shear flow relative to the surface features of the ice, indicating that the hydrogen bonding statistics between an ice facet and the liquid are not altered by the imposed shear.

### 3.4.0.2 Surface corrugation

A second possible influence on the friction coefficient is the surface topography of the ice crystals, the dimensions of which are reported in Table 3.3. When a crystal of ice-I<sub>h</sub> is cleaved along either of the two prismatic crystal facets, the exposed oxygen atoms present channel-like structures with channel widths of 6.35 Å and channel

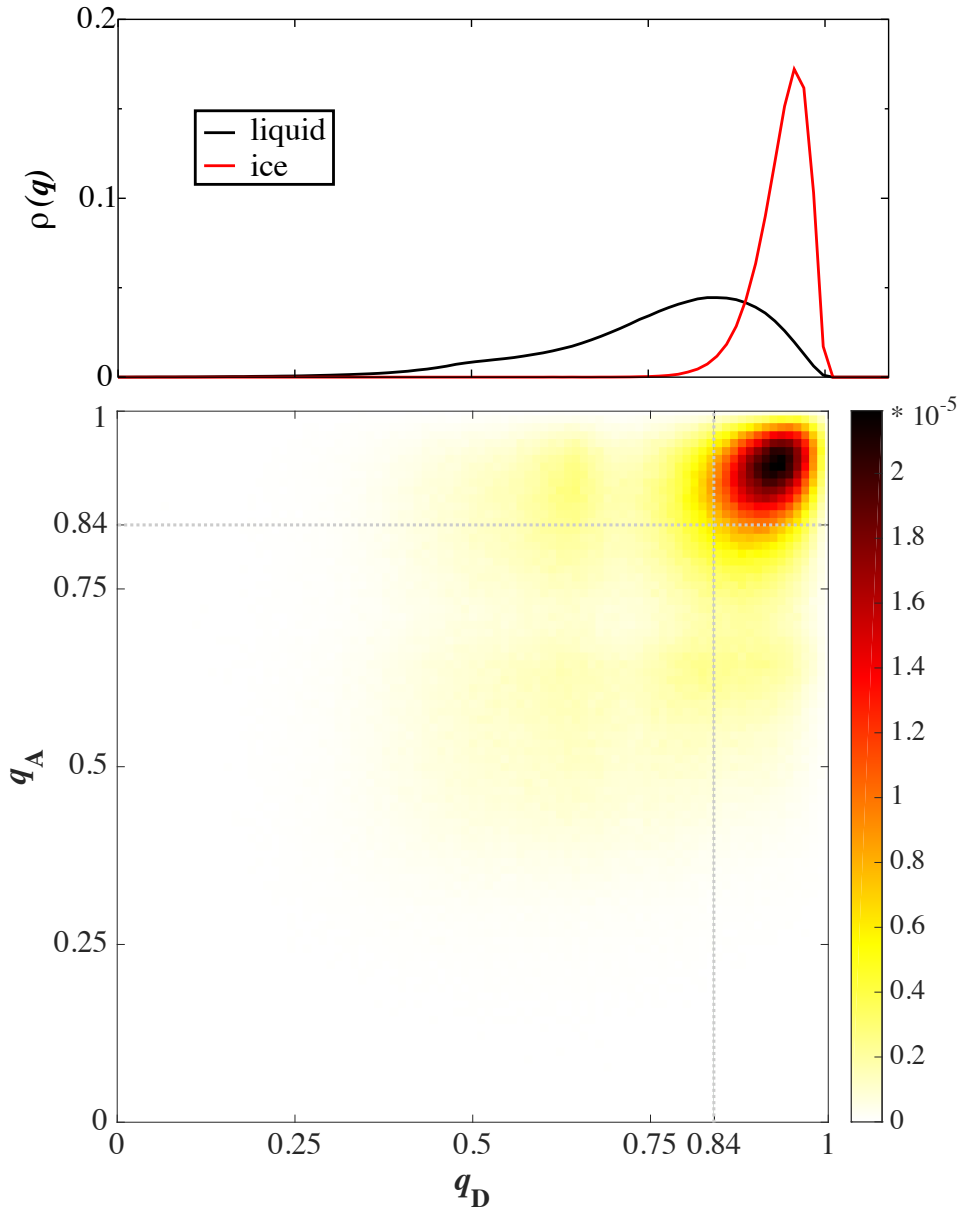


Figure 3.7. Distribution of hydrogen bonds at a prismatic interface showing the tetrahedralities of donor ( $q_D$ ) and acceptor ( $q_A$ ) molecules (lower panel). Distributions of tetrahedralities in bulk ice and liquid phases are shown in the upper panel, and the value of  $q$  at the Gibbs dividing surface is indicated with dashed lines. Hydrogen bonds between ice molecules are represented by the upper right square, while those between liquid molecules are in the lower left. Hydrogen bonds that bridge the ice-liquid interface exist primarily in the vertical and horizontal strips that remain.

depths of 2.25 Å . When cleaved along the pyramidal facet, the resulting surface features a much larger channel, ~ 8.7 Å wide. Conversely, the basal surface presents a rather smooth surface to the liquid, with stripes of oxygen atoms forming surface ripples with depths of ~ 1.3 Å .

TABLE 3.3

Surface features of Ice-I<sub>h</sub> facets.

Interface	Channel width (Å)	Channel depth (Å)
Basal {0001}	4.49	1.30
Prismatic {10̄10}	6.35	2.25
Pyramidal {20̄21}	8.65	2.59
Secondary Prism {11̄20}	6.35	2.25

The prismatic channels are quite stable. That is, we do not observe liquid phase molecules populating the prismatic and secondary prism surface channels. One might expect regions of low liquid density to yield smaller solid-liquid interactions, and it does appear that these two surfaces present roughly half of the surface oxygen atoms to the liquid. However, the molecules forming the bottoms of the channels are fully saturated (four hydrogen bonds each), while the molecules that form the tops of the channels present a high density of available hydrogen bond locations.

The oxygen-based surface features of the prism and secondary prism are identical, and only the orientation of the water molecules varies. This means that the

patterning of donor and acceptors on the two facets is quite different. A liquid with internal hydrogen bonding constraints that is in contact with these facets will allow the prismatic surface to form a higher density of solid-liquid hydrogen bonds than the secondary prism, even with identical oxygen ordering at the interface.

In contrast with the prismatic facets, liquid state molecules do populate the surface channels on the pyramidal facet. Again, one might expect the interactions between the solid and the liquid in close physical contact to be quite large. However, the liquid molecules populating this channel do not pack efficiently and cannot fully saturate the surface locations available for hydrogen bonding, resulting in a lower solid-liquid hydrogen bond density and a smaller coefficient of friction.

With its smooth surface, one could make reasonable physical arguments for the basal face to have either high or low friction with liquid water. That is, liquid molecules should be able to form a fully populated network of hydrogen bonds with the surface, as there are no recessed surface molecules at the bottoms of deep channels, and no channel packing constraints. In the absence of large surface undulations, however, liquid-phase molecules should also be able to slip over the surface easily. However, the basal facet was found to have an intermediate friction coefficient compared with the other facets studied here. The sensible explanation in light of the hydrogen bonding data is simply that the surface density of solid-liquid hydrogen bonds (however transitory) dominates the interfacial friction.

### 3.5 Conclusions

RNEMD simulations of the different facets of ice being drawn through surrounding water at the coexistence temperature indicate some facet-dependence of solid-liquid friction. We have defined a negative slip interfacial friction coefficient,  $\kappa$  (measured in amu Å<sup>-2</sup> fs<sup>-1</sup>) and find that the two prismatic facets exert the largest drag on the surrounding liquid. The basal facet provides an intermediate level of drag, while the

pyramidal facet has roughly half the interfacial friction of the prismatic facet.

Using the local tetrahedral order parameter as a metric to differentiate ice and liquid water molecules and a geometric hydrogen bonding criteria, the friction coefficients were shown to be largely governed by the surface density of solid-liquid hydrogen bonds ( $\rho_{sl}$ ). A simple linear fit for the four interfaces yields

$$\kappa \approx 2.1772(\text{amu fs}^{-1}) \times \rho_{sl}(\text{\AA}^{-2}) + 0.0777(\text{amu \AA}^{-2} \text{ fs}^{-1}), \quad (3.11)$$

so the majority of the calculated solid-liquid friction is determined by the surface density of solid-liquid hydrogen bonds.

In addition, we have found the ice / water interfacial widths for all four crystal facets to be similar (using both structural and dynamic measures) and found these widths to be independent of shear rate. The similarity of interfacial width estimates for the four facets indicate that the particular facet of the exposed ice crystal has very little effect on how far into the bulk the ice-like structural ordering persists. While differences have been found in previous simulations of ice / water interfaces<sup>56, 57</sup>, experimentally these differences have been less clear.<sup>73</sup> The significant differential friction coefficients obtained here suggest that while the liquid next to the ice might be structurally organized like bulk liquid, the dynamics of the molecules are still quite strongly perturbed by the ice. That is, the surface hydrogen bonding significantly alters how the water layers are pulled along with the ice during shear.

### 3.6 Fitting velocity profiles

In order to calculate solid-liquid friction coefficients,  $\kappa$  from Eq. (5) in the main text, the velocity profiles,  $v_x(z)$ , obtained from each shearing simulation were fit assuming linear behavior through each of the three regions of the simulation box; the lower liquid, the solid, and the upper liquid. Parabolic functions were designed to

capture the negative slip behavior that links the three regions,

$$v(z) = \begin{cases} v_l - m_l z & 0 \leq z < (z_1 - w) \\ v_s - \frac{1}{2}k(z - z_1)^2 & (z_1 - w) \leq z < z_1 \\ v_s & z_1 \leq z < z_2 \\ v_s - \frac{1}{2}k(z - z_2)^2 & z_2 \leq z < (z_2 + w) \\ v_s - \frac{1}{2}kw^2 - m_l(z - (z_2 + w)) & (z_2 + w) \leq z \end{cases} \quad (3.12)$$

Here,  $v_l$  is the velocity of the liquid at the middle of the liquid domain (the edge of the simulation box), and  $v_s$  is the velocity of the solid. The locations  $z_1$  and  $z_2$  are the edges of the ice slab, and  $w$  is the width of the interface (distinct from  $w_{10-90}$  mentioned in the main text). The parameter  $m_l$  is the slope of the velocity profile in the liquid regions of the box which is related to the liquid-state viscosity. Figure 3.8 shows a representative velocity profile (navy squares) and fit (green line) with the locations of  $z_1$  and  $z_2$  indicated as vertical dotted lines. Once the fits were obtained, the values for  $v_x(solid)$  and  $v_x(liquid)$  for Eq. (5) were sampled from the fit. The  $z$  locations used to sample the fit were determined by structural measures. The  $z$  location for  $v_x(liquid)$  was taken to be the Gibbs dividing surface of the interface, less the 10–90 width of the interface. Similarly, the  $z$  location for  $v_x(solid)$  was taken to be the Gibbs dividing surface plus the 10–90 width of the interface.

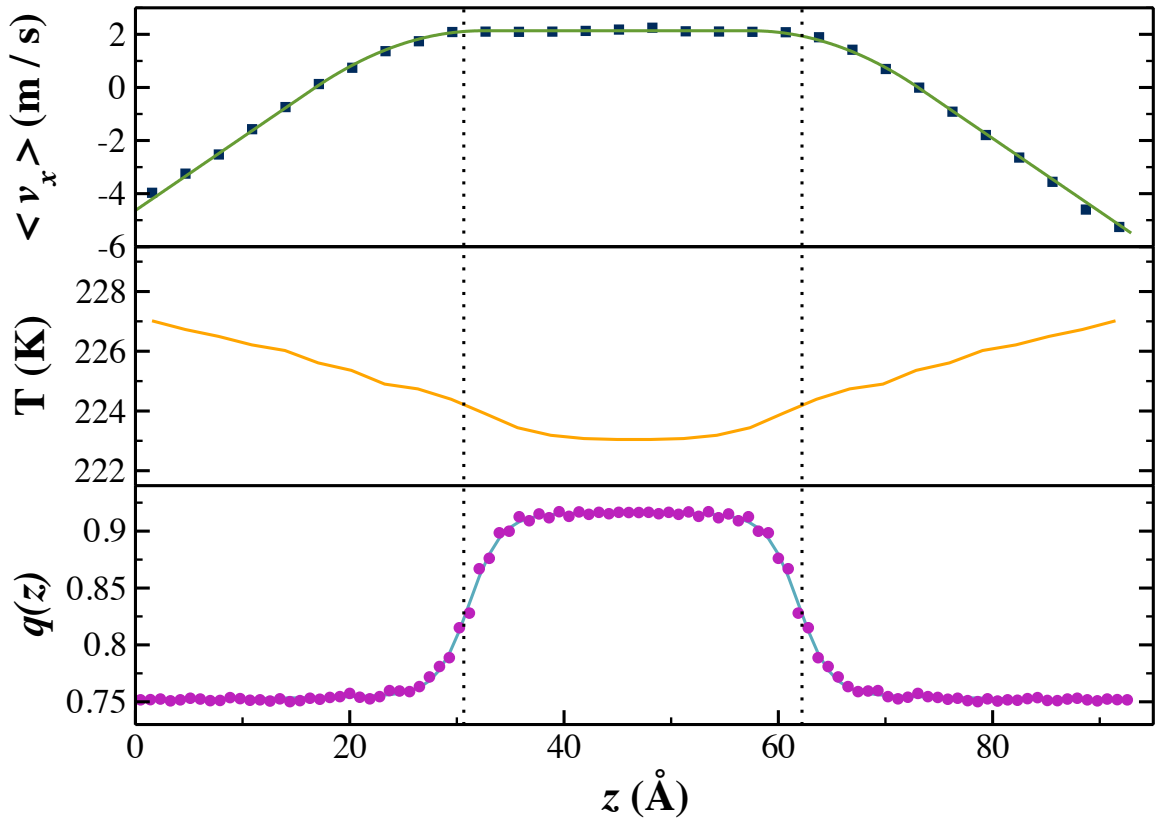


Figure 3.8. Properties of the pyramidal interface being sheared through water at  $7.6 \text{ ms}^{-1}$ . Lower panel: the local tetrahedral order parameter,  $q(z)$ , (circles) and the hyperbolic tangent fit (turquoise line). Middle panel: the imposed thermal gradient required to maintain a fixed interfacial temperature of 225 K. Upper panel: the transverse velocity gradient (squares) that develops in response to an imposed momentum flux, along with the fit (green line). The vertical dotted lines indicate the locations of the Gibbs dividing surfaces of the two interfaces.

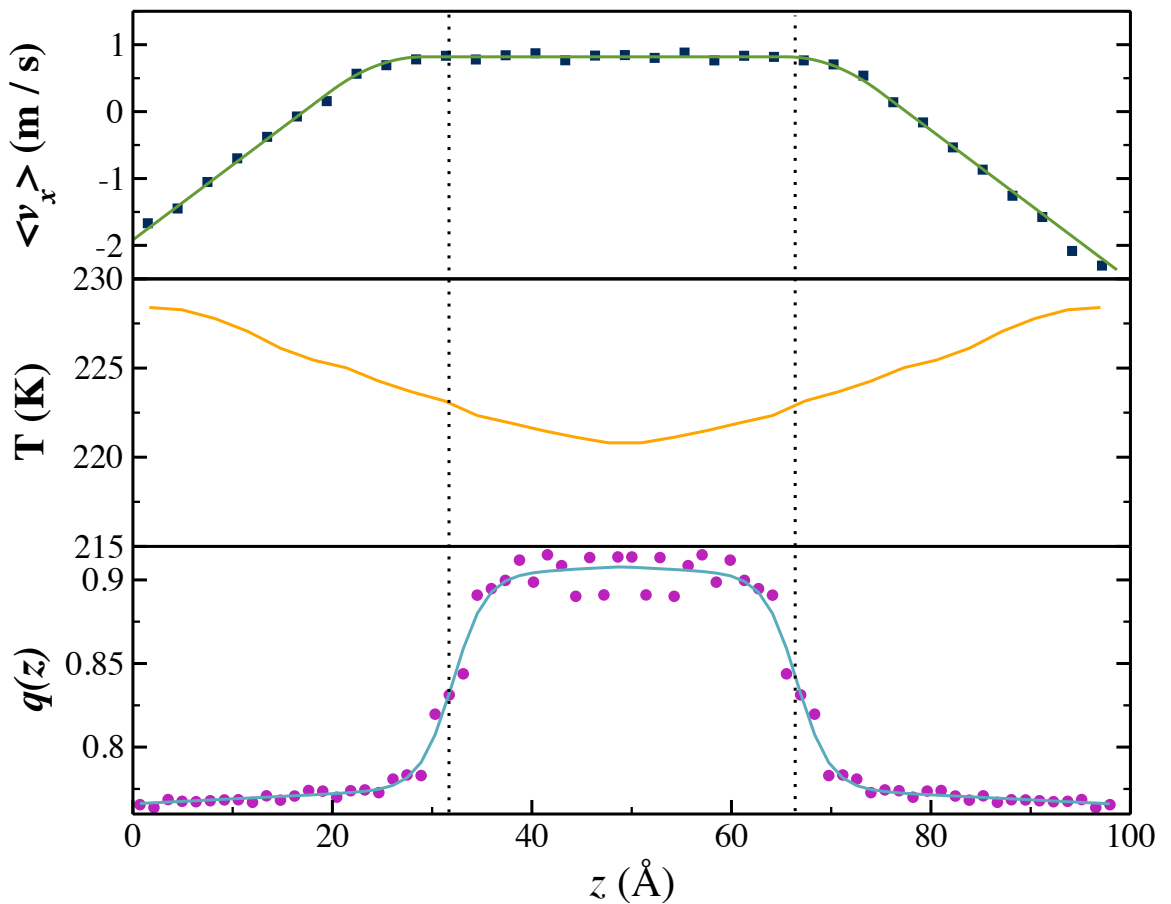


Figure 3.9. Properties of the basal interface being sheared through water at  $3.2 \text{ ms}^{-1}$ . Panel descriptions are the same as in Fig. 3.8.

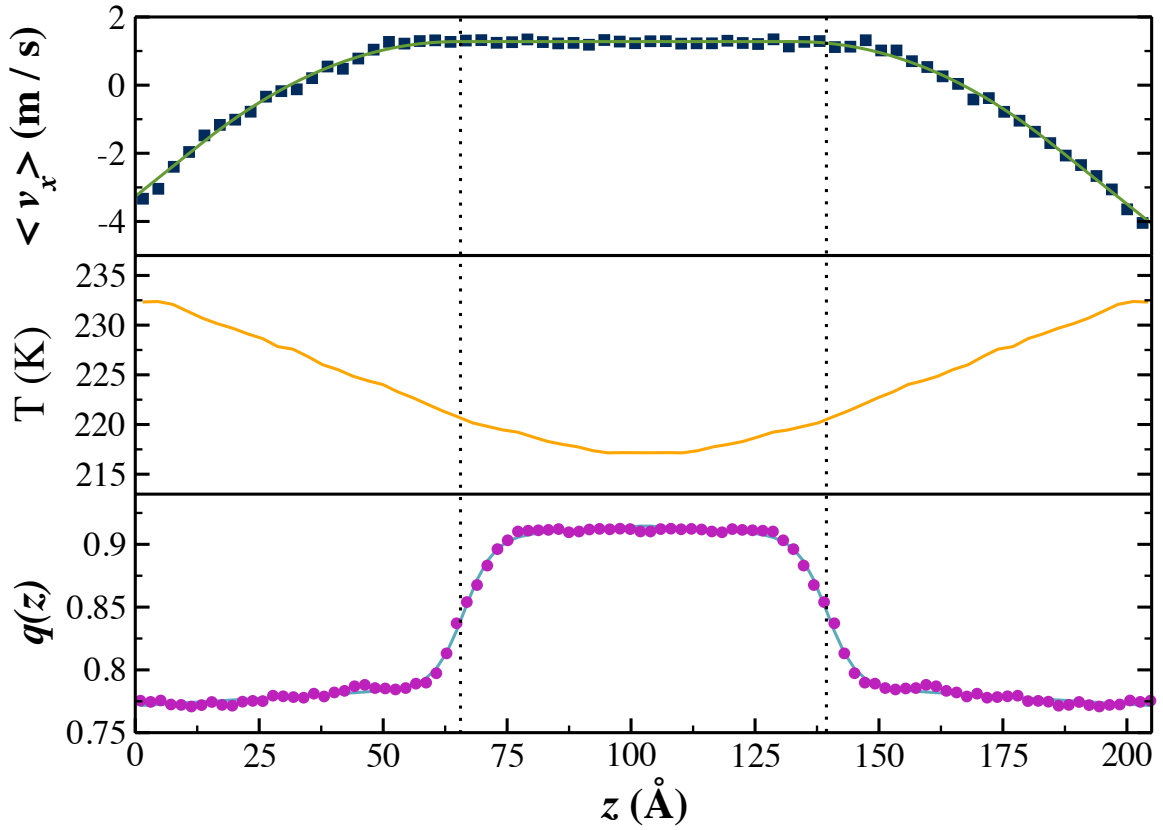


Figure 3.10. Properties of the prismatic interface being sheared through water at  $6.0 \text{ ms}^{-1}$ . Panel descriptions are the same as in Fig. 3.8.

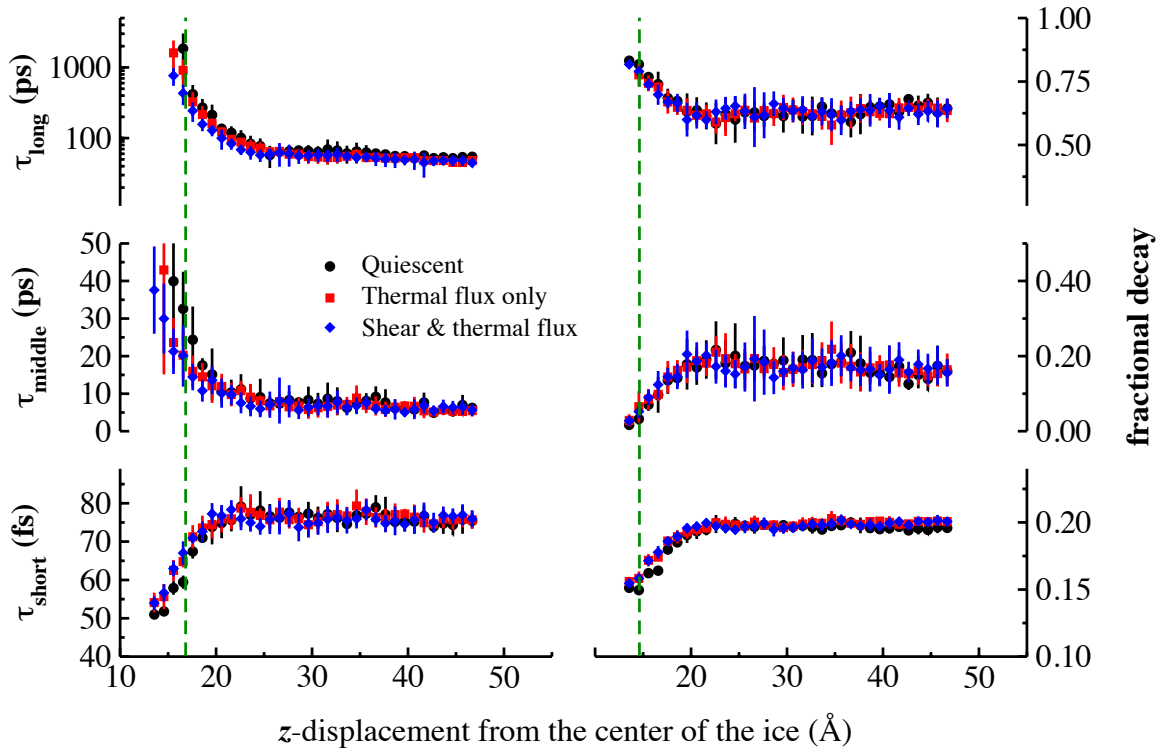


Figure 3.11. Decay times (left) for  $C_2(z, t)$  at the pyramidal interface, and their fractional contributions to the overall decay (right) fit using Eq. (8).

The local decay constants are plotted as a function of distance from the center of the ice slab. The vertical dashed line indicates the Gibbs dividing surface determined using the local tetrahedral order parameter. Results are shown for a quiescent system with no applied kinetic or momentum flux (black), an interface with an imposed kinetic energy flux (red), and a sheared simulation (blue) with both kinetic and momentum fluxes.

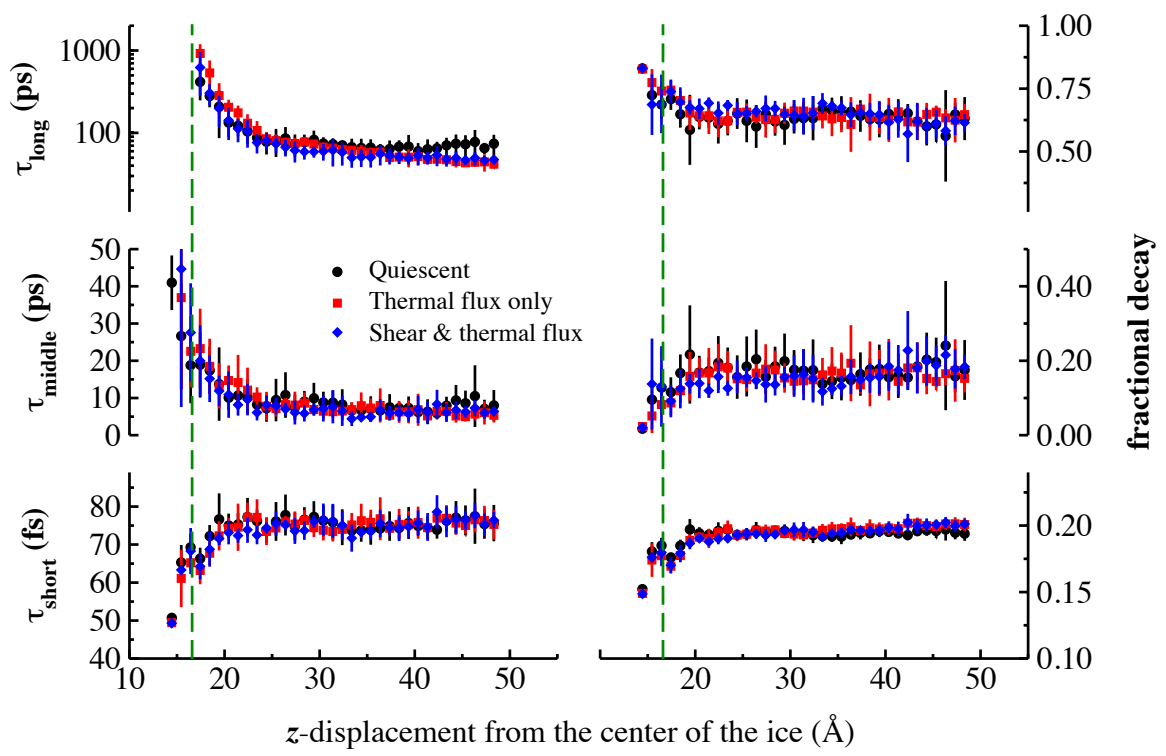


Figure 3.12.  $C_2(z, t)$  time constants for the basal interface. Panel descriptions are the same as in Fig. 3.11.

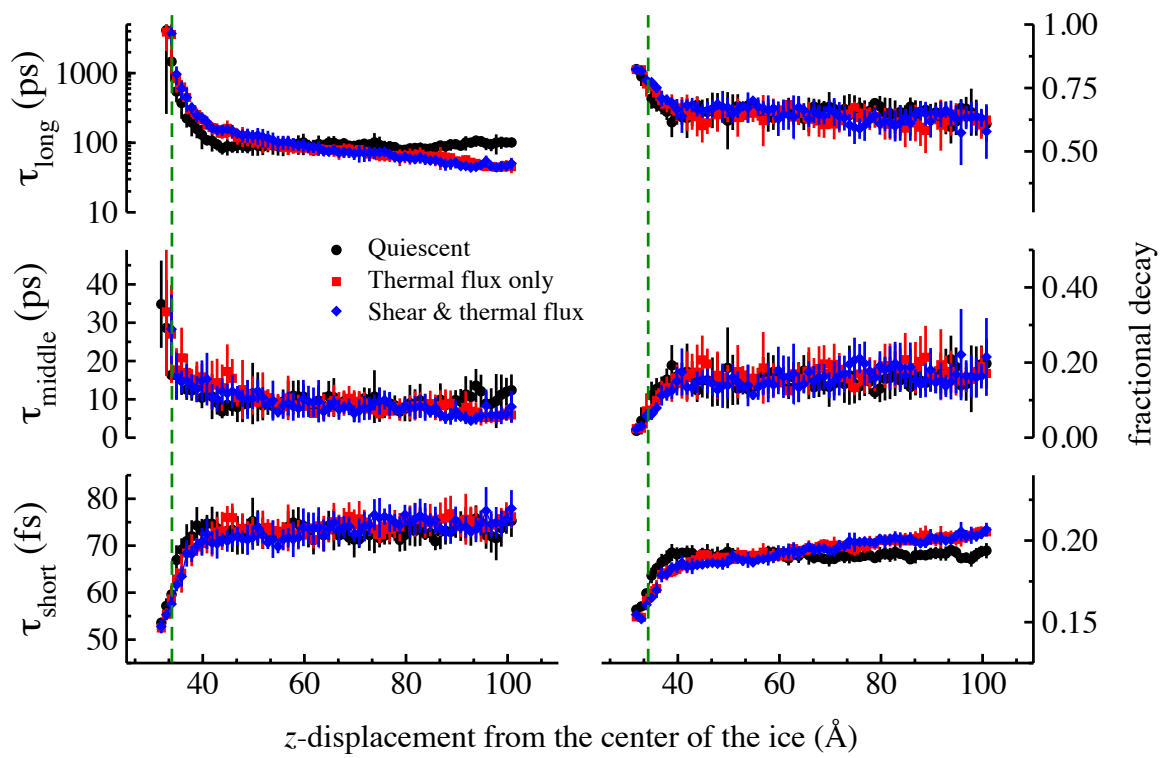


Figure 3.13.  $C_2(z, t)$  time constants for the prismatic interface. Panel descriptions are the same as in Fig. 3.11.

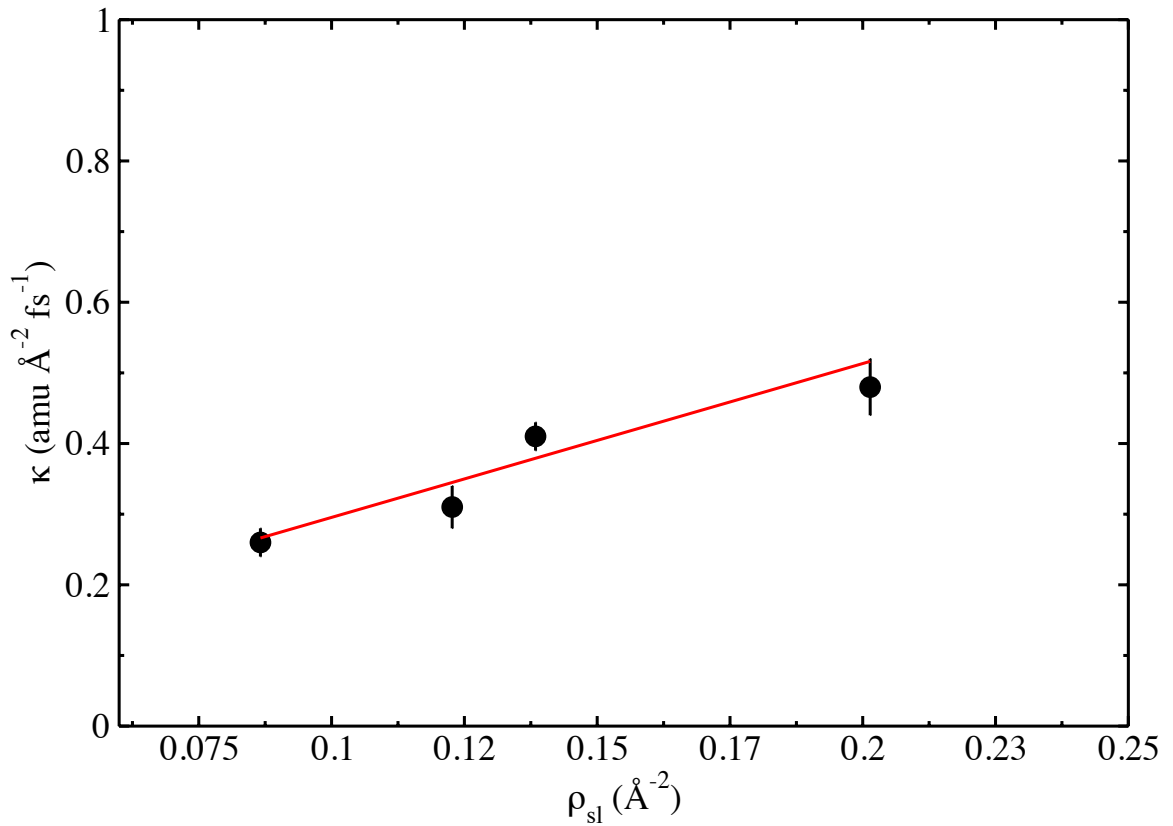


Figure 3.14. Solid-liquid friction coefficients by the surface density of hydrogen bonds. Linear regression gives a slope of 2.1772 (amu  $\text{fs}^{-1}$ ) and a y-intercept of 0.0777 (amu  $\text{\AA}^{-2}$   $\text{fs}^{-1}$ ).

## APPENDIX A

### A Single-Site Model for Water: Parameterized for the Reproduction of the Melting Point of Ice I<sub>h</sub>

#### A.1 Introduction

Abascal and Vega have recently observed that the melting points of common 3-site and 4-site water models correlates strongly with their dipolar and quadrupolar interactions.<sup>?</sup> <sup>?</sup> <sup>?</sup> To quantify dipole and quadrupole moments, we must first consider how to define our coordinate system. For planar water models, we define our coordinate system in the following way; the  $z$  axis as the dipole moment direction (the HOH bisector), the  $y$  axis parallel to the vector connecting the two Hydrogens, and the  $x$  axis normal to the plane of the molecule. This choice of coordinate system follows that of Rick, and thus the equations in his paper follows naturally. Abascal and Vega define their coordinate system by flipping the  $x$  and  $y$  axes, resulting in a few sign changes between our work and theirs. Having defined a coordinate system, we can calculate the traceless quadrupole tensor,  $\Theta$ , for any water model by

$$\Theta_{ij} = \frac{1}{2} \sum_{\alpha} q_{\alpha} (3r_{i,\alpha}r_{j,\alpha} - |\vec{r}_{\alpha}|^2 \delta_{ij}) \quad (\text{A.1})$$

where,  $q$  is the charge and the sum is taken over all charged sites in the model. The traceless quadrupole tensor has certain special properties, and is aptly named for one of them; which is the trace, ( $Tr$ ), of the tensor is null.

$$Tr(\Theta) = \sum_{i,j} \Theta_{ij} \delta_{ij} = 0 \quad (\text{A.2})$$

While having a traceless tensor can make certain calculations easier to perform, it is also possible to calculate a traced quadrupole tensor  $Q$ , one in which the trace is not null.

$$Q_{ij} = \frac{1}{2} \sum_{\alpha} q_{\alpha}(r_{i,\alpha} - r_{i,com})(r_{j,\alpha} - r_{j,com}) \quad (\text{A.3})$$

Here,  $r_{i,com}$  is the position of the center of mass in the  $i$ -th dimension, and therefore the position of the quadrupole moment is set at the center of mass of the molecule. It will be desirable to change between the traceless and traced quadrupole tensors during this work, and changing between the two formalisms can be achieved by the following

$$\Theta = 3Q - Tr(Q) \quad (\text{A.4})$$

Based on the suggestion of Carnie and Patey? , as well as Rick? , Abascal and Vega have described an effective tetrahedral quadrupole moment ( $\Theta_T$ ), defined in ours and Rick's coordinate system for a traceless quadrupole as

$$\Theta_T = \frac{1}{2}(\Theta_{yy} - \Theta_{xx}). \quad (\text{A.5})$$

Abascal and Vega have shown that the water models which most accurately reproduce the melting point of ice  $I_h$  have a ratio of their dipole moment to  $\Theta_T$  of approximately unity. The equivalent expression for the traced quadrupole tensor is given as

$$Q_T = \frac{3}{2}(Q_{yy} - Q_{xx}). \quad (\text{A.6})$$

The  $Q_T$  values for each of the water models investigated by Abascal and Vega are shown in Table A.1, along with the non-zero elements of their traced quadrupole

tensors.

	$Q_{xx}$	$Q_{yy}$	$Q_{zz}$	$Tr(Q)$	QBar	$Q_T$	$T_m$
TIP4P/Ice	0.0	1.6629	0.7427	2.3657	2.8143	2.4348	272.2
TIP4P/2005	0.0	1.531	0.7034	2.2336	2.6553	2.2969	252.1
TIP4P/Ew	0.0	1.4427	0.6617	2.1044	2.5017	2.1640	245.5
TIP4P	0.0	1.4311	0.6584	2.0895	2.4814	2.1466	232.0
SPC/E	0.0	1.357	0.5267	1.8837	2.3700	2.0356	215.0
SPC	0.0	1.3129	0.5095	1.8224	2.2928	1.9693	109.5
TIP3P	0.0	1.1476	0.5337	1.6812	1.9894	1.7214	146

TABLE A.1

Traced quadrupole tensors for the water models investigated by Abasca and Vega. All elements of the tensors are in units of DÅ , melting temperatures are reported in Kelvin.

In Figures A.1 and A.2, we have replotted the melting point for ice I<sub>h</sub> of these water models by  $\overline{Q}$  and the trace of their quadrupole tensor, where  $\overline{Q}$  is given by,

$$\overline{Q} = \sqrt{2(3Q : Q - (Tr(Q))^2)} \quad (\text{A.7})$$

We see in both cases there is a strong correlation between the values of their quadrupole tensors and their melting point.

Based on this observation, we have begun work on a 1-site model with intentions

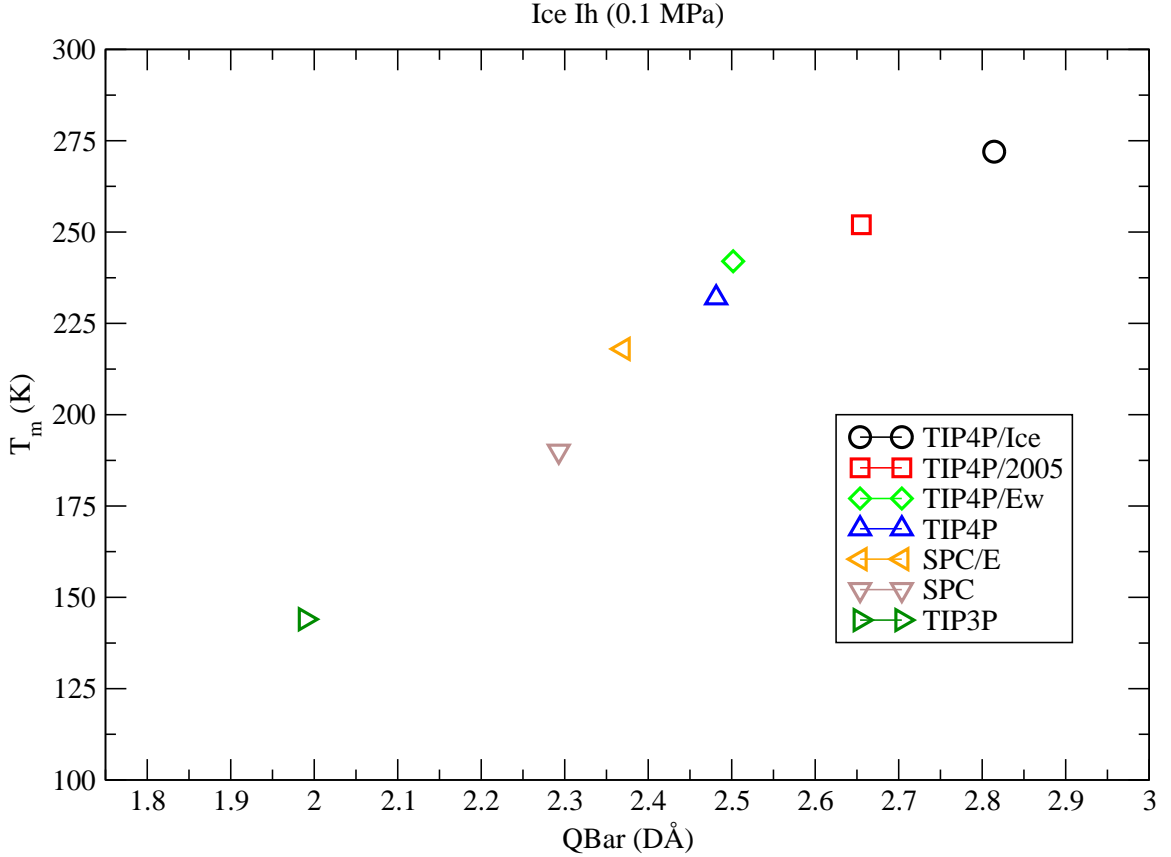


Figure A.1. Melting point for ice  $I_h$  of several popular water models as a function of the QBar for the model. We see a strong correlation between a more accurate melting point and a larger value of QBar. We estimate that

a QBar of approximately 2.8 DÅ will result in the experimental melting point of 273.15 K. A linear regression of the data resulted in an equation of best fit of  $y = 158.89x - 166.83$ . From this, we have predicted an optimal QBar to be 2.7690 DÅ .

of setting the dipole moment and structuring the quadrupole tensor in such a way that will give us a ratio of unity. As a starting point, we have collapsed the 4-site TIP4P-Ice model? onto a 1-site model (TIP1P/Ice). The geometric parameters, the Lennard-Jones and charges, and the dipole and quadrupole elements that have value can be found for both models in Table A.2, Table A.3, and Table A.4 respectively.

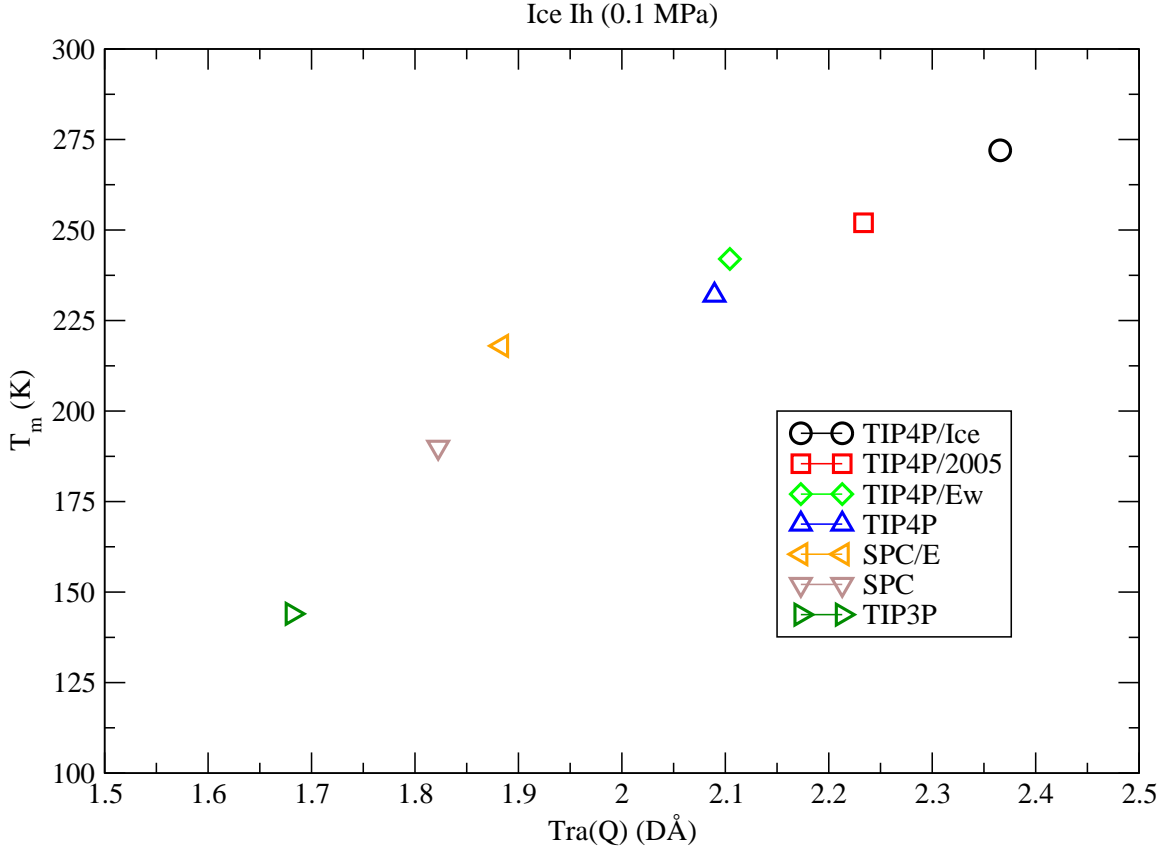


Figure A.2. Melting point for ice  $I_h$  of several popular water models as a function of the trace of the quadrupole tensor for the model. We see a strong correlation between a more accurate melting point and a larger value of the trace. We estimate that a trace of approximately  $2.3 \text{ D}\text{\AA}$  will result in the experimental melting point of  $273.15 \text{ K}$ .

## A.2 TIP1P/Ice

### A.2.1 Gas Phase Dimer

This section contains details and graphs of the attempts to tune the TIP1P/Ice model to the experimental and ab initio predicted results for the gas phase water dimer. In order to tune the TIP1P/Ice model, we are going to calculate the geometry of the gas phase water dimer as shown in Figure A.3? .

There are three values of interest for our characterization of the water dimer. The

	OH bond length Å	OM bond length Å	HOH °
TIP4P/Ice	0.9572	0.1577	104.52
TIP1P/Ice	-	-	-

TABLE A.2

Geometric parameters of the TIP4P/Ice and TIP1P/Ice models.

	$\sigma$ Å	$\epsilon$ kcal/mol	$q_H$ (e)	$q_M$ (e)
TIP4P/Ice	3.1668	0.2108509	0.5897	-1.1794
TIP1P/Ice	3.1668	0.2108509	-	-

TABLE A.3

Lennard-Jones and charge parameters of the TIP4P/Ice and TIP1P/Ice models.

	$\mu$ D	$Q_{xx}$ DÅ	$Q_{yy}$ DÅ	$Q_{zz}$ DÅ	$Q_T$ DÅ
TIP4P/Ice	2.4255966	0.0	1.62291807	0.74278997	2.434
TIP1P/Ice	2.4255966	0.0	1.62291807	0.74278997	2.434

TABLE A.4

Dipole and quadrupole parameters for the TIP4P/Ice and TIP1P/Ice models.

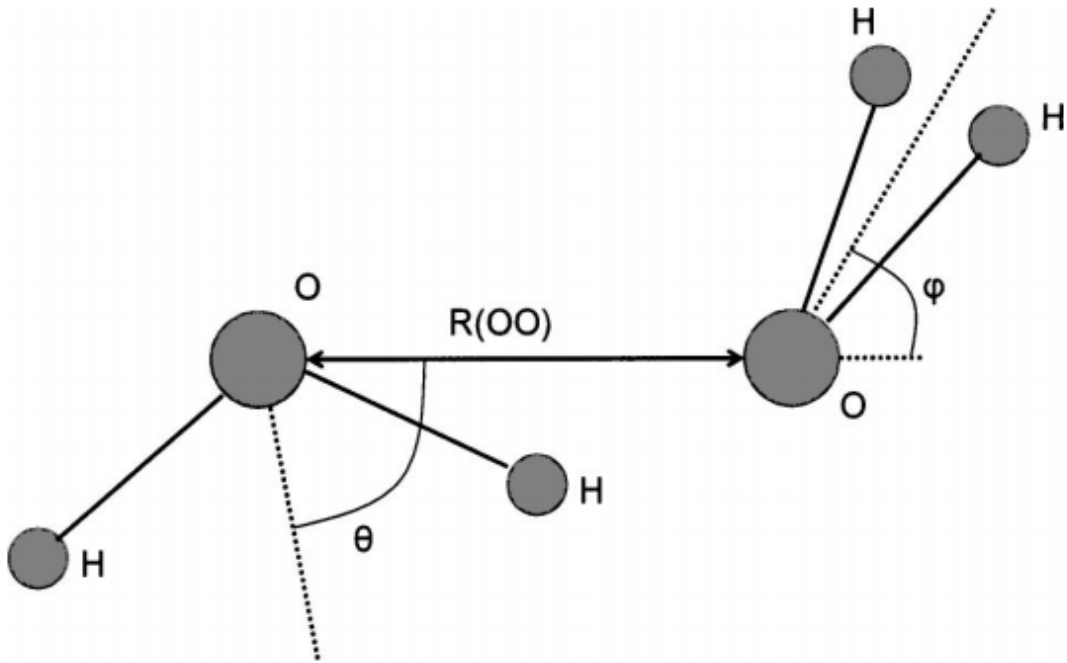


FIG. 2. Definition of the distance  $R(OO)$  and the angles  $\theta$  and  $\phi$  that determine the relative position and orientation of the monomers of the water dimer in the gas phase.

Figure A.3. The gas phase water dimer geometry.

first is the oxygen-oxygen separation distance,  $R_{OO}$ . The other two parameters of the dimer are the two angles,  $\theta$  and  $\phi$ . These angles are taken from the HOH bisector to the  $R_{OO}$  vector. While the length of the  $R_{OO}$  vector will be dependent on the magnitude of the dipole and quadrupole moments, the relative contributions of  $Q_{xx}$ ,  $Q_{yy}$ , and  $Q_{zz}$  will strongly influence the angles. We also expect that the Lennard-Jones parameter  $\sigma$  will strongly influence the magnitude of the  $R_{OO}$  vector. The experimentally measured and computationally predicted values for the geometry of the water dimer can be found in Table A.5. Also in Table A.5, we see the geometry parameters computed at 0.1 K for the TIP4P/Ice and TIP1P/Ice models.

	$R_{OO}$ (Å)	$\theta$ (°)	$\phi$ (°)
Expt.	2.95	$51 \pm 10$	$57 \pm 10$
Ab initio	2.91	56	58
TIP4P/Ice	2.79	52.52	43.17
TIP1P/Ice	2.83	40.56	36.59

TABLE A.5

Geometric parameters of the TIP4P/Ice and TIP1P/Ice gas phase water dimer. Ab initio and Expt. values were taken from another source? .

#### A.2.1.1 Testing Electrostatic Cutoff

First we will see if we can recover the TIP4P/Ice dimer geometry by decreasing damping  $\alpha$  to  $0.05 \text{ \AA}^{-1}$  and vary the cutoff radius for the electrostatics. In Figure A.4, we see that with very small damping  $\alpha$ , increasing the cutoff radius of the potential does not recover the TIP4P/Ice calculated geometry.

#### A.2.1.2 Varying Lennard-Jones Parameters

In our initial test, as seen in Figure A.5, the Lennard-Jones parameter  $\sigma$  was varied while holding the other parameters of the TIP1P/Ice model constant. We see that the ab. initio predicted  $R_{OO}$  separation distance of  $2.91 \text{ \AA}$  is obtained when  $\sigma$  is set to approximately  $3.25 \text{ \AA}$ . However, the two angles  $\theta$  and  $\phi$  tend to decrease with increasing values of  $\sigma$ , and result in values of about  $36^\circ$  and  $31^\circ$ , which is in poor agreement with the ab. initio calculations. Also, changing the Lennard-Jones parameter  $\sigma$  will drastically alter the condensed phase properties of the model. Namely, the radial distribution function is very sensitive to  $\sigma$ . The location of the first solvation shell can be tuned by  $\sigma$ , so we will initially retain the TIP4P/Ice model's value of

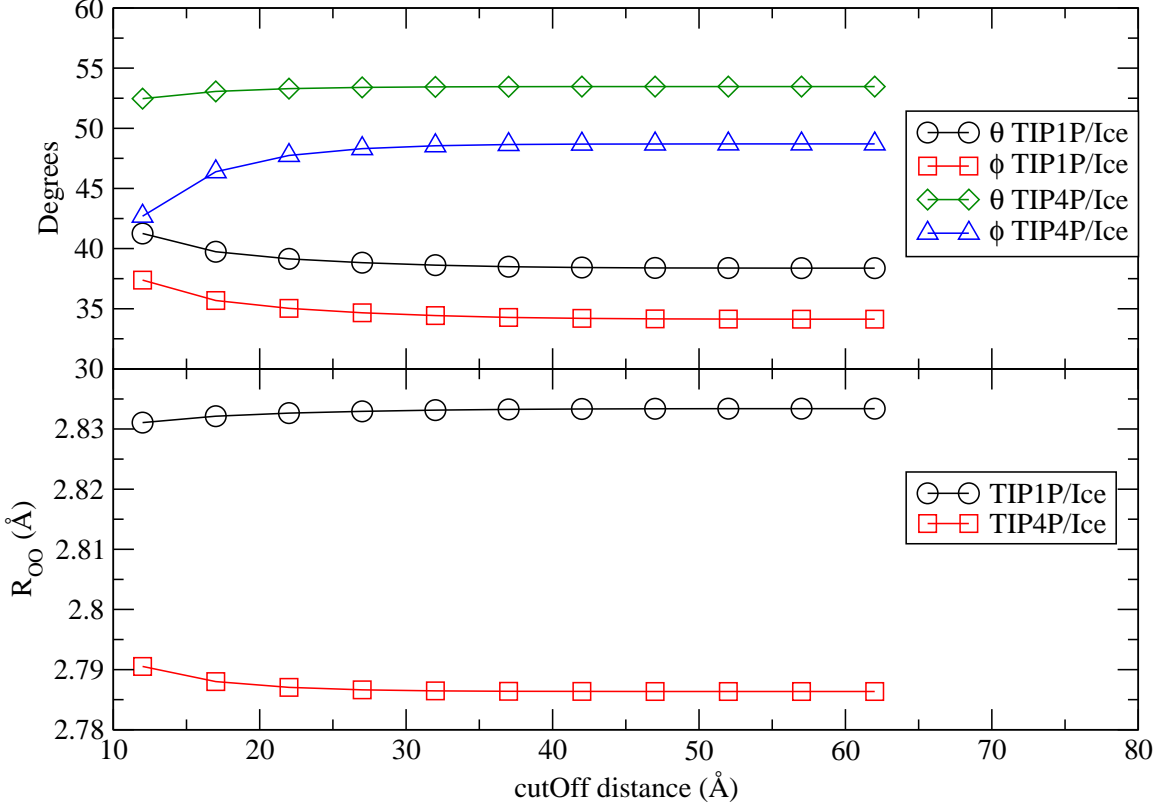


Figure A.4. Damping  $\alpha$  set to  $0.05 \text{ \AA}^{-1}$  and the simulation box was  $300 \times 300 \times 300 \text{ \AA}$ .

$3.1668 \text{ \AA}$  and vary it later if the radial distribution function is off.

Next, we will vary the Lennard-Jones parameter  $\epsilon$ , as seen in Figure A.6. We see that the ab. initio calculated value of  $R_{OO}$  distance of about  $2.91 \text{ \AA}$  is achieved when  $\epsilon$  is set to approximately  $0.275 \text{ kcal/mol}$ . However, both  $\theta$  and  $\phi$  tend to decrease with increasing  $\epsilon$ , and the resulting values for the two angles at this value of  $\epsilon$  are approximately  $38^\circ$  and  $33^\circ$ , which are again far from the predicted values. Changing  $\epsilon$  is not a great way to parameterize the model though, and we will avoid doing so as much as possible.

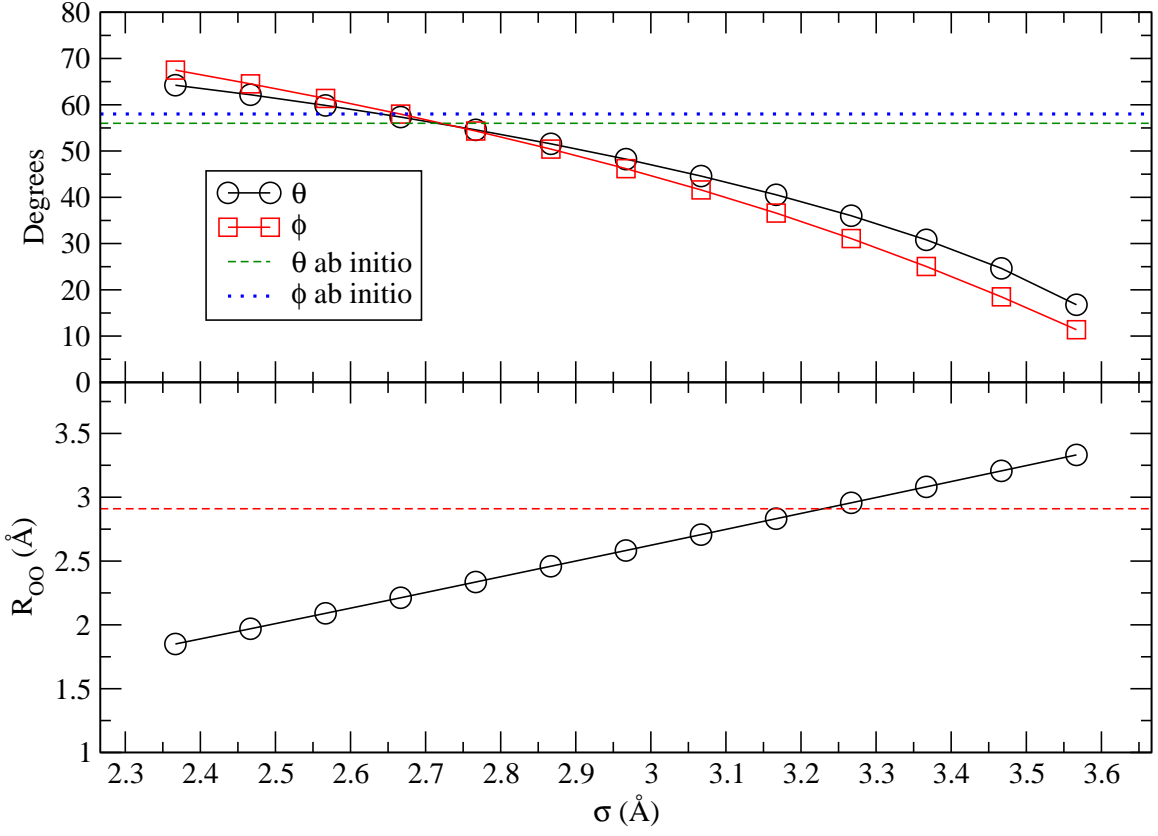


Figure A.5. The Lennard-Jones parameter  $\sigma$  was varied while holding the other parameters of the TIP1P/Ice model constant.

#### A.2.1.3 Varying Damping $\alpha$

Having changed both the Lennard-Jones parameters independently and not achieving the desired values for the separation distance or angles of the gas phase water dimer, the next natural parameter of the TIP1P/Ice model to vary would be the dipole or quadrupole moment. Before doing so, however, we will vary the damping  $\alpha$  value which effects how the electrostatics are calculated in OpenMD? . In Figure A.7, we see that  $R_{OO}$  is minimally effected by varying damping  $\alpha$  for small values of  $\alpha$ . For values larger than about  $0.25 \text{ \AA}^{-1}$ , the dimer separation distance decreases slightly. However, the ab. initio calculated distance is not recovered by varying damping  $\alpha$  alone. The angles  $\theta$  and  $\phi$  also do not converge on the ab. initio predicted values

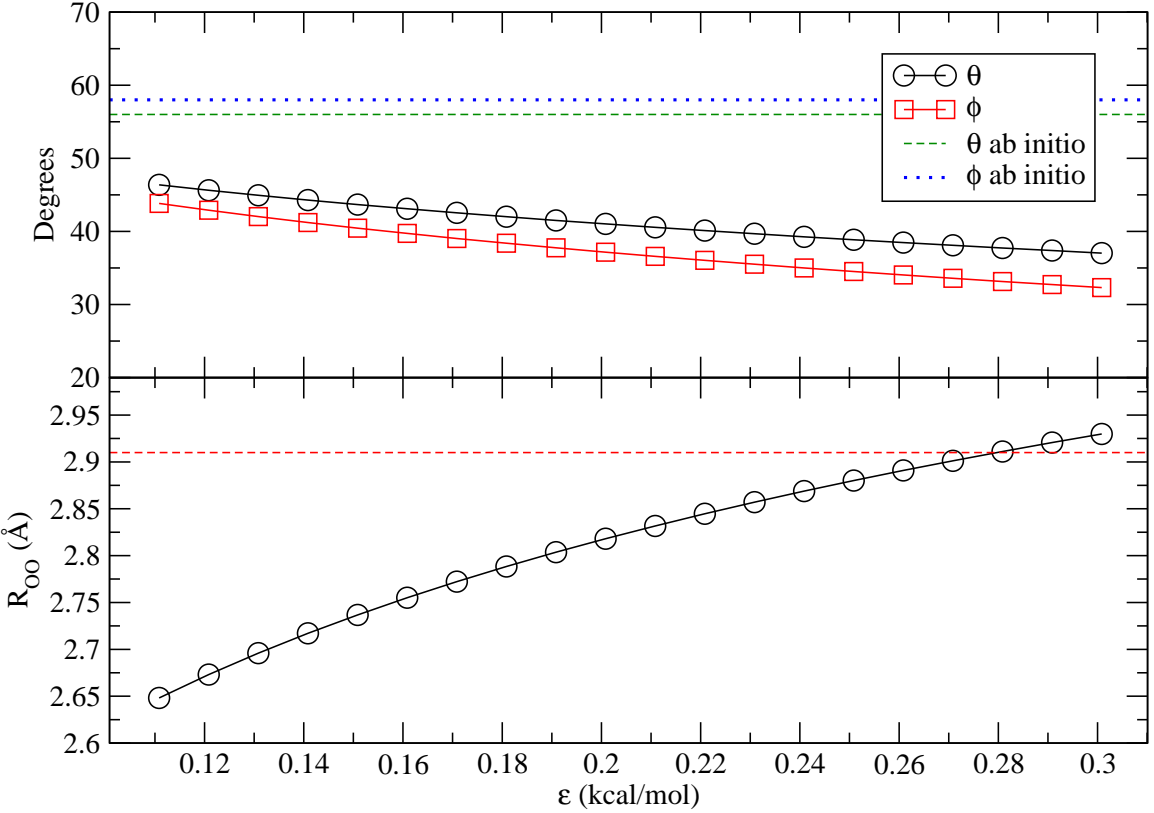


Figure A.6. The Lennard-Jones parameter  $\epsilon$  was varied while holding the other parameters of the TIP1P/Ice model constant.

over the range of damping  $\alpha$  investigated here. After talking with Madan, damping  $\alpha$  values of about  $0.1 \text{ \AA}^{-1}$  are suitable for handling the calculation of dipoles and quadrupoles, which is the value that has been used in all other Tests shown here.

#### A.2.1.4 Varing the Quadrupole: Introduction of $Q_{xx}$

A possible reason we have not been able to capture the correct gas phase water dimer geometry by modifying the Lennard-Jones parameters, may be due to the initial construction of the quadrupole tensor for the TIP1P/Ice model. In this model, as with all planar water models, one of the quadrupole tensor's main diagonal elements will be zero, given intelligent choice of origin for the coordinate system. In our

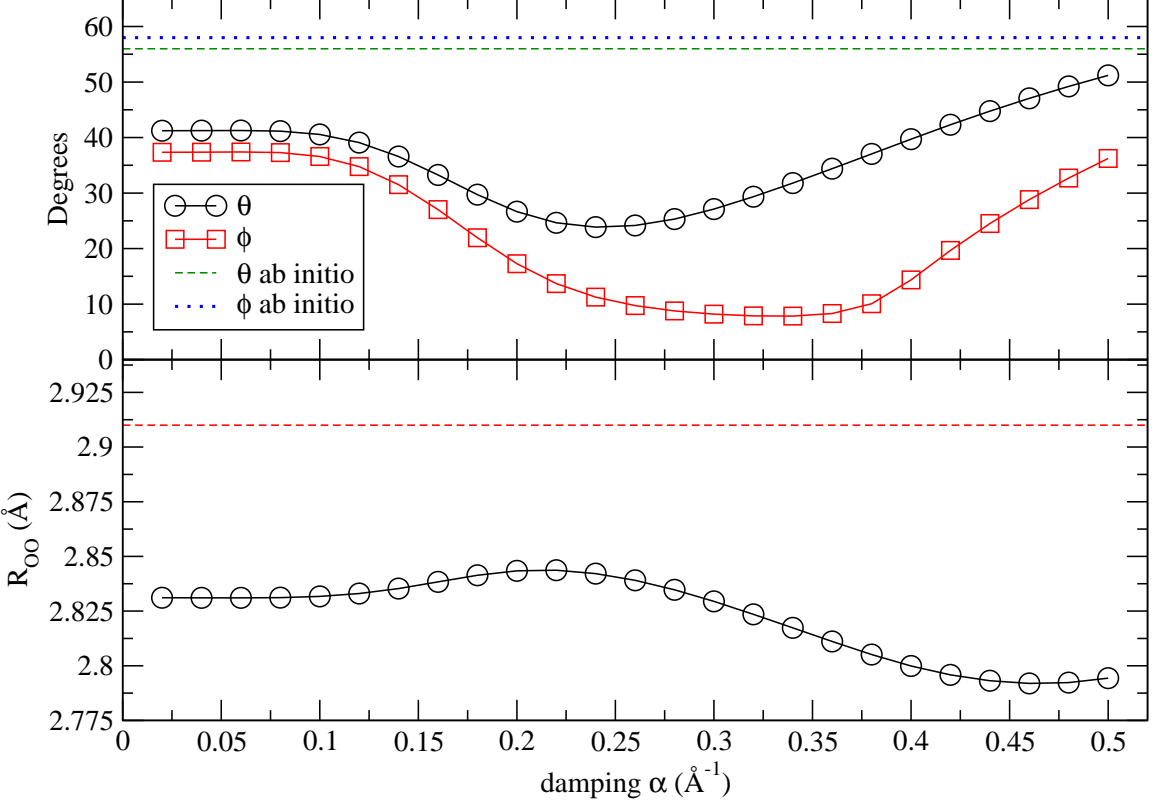


Figure A.7. Damping  $\alpha$  was varied while holding the otherparameters of the TIP1P/Ice model constant.

construction, this is the  $Q_{xx}$  term, as seen in Table A.4. In the following Tests, we will try to incorporate the quadrupole moment of the  $x$ -dimension into our model.

We will consider varying the quadrupole tensor elements of the TIP1P/Ice model while holding all other parameters constant. This requires special consideration though, as we may not want to deviate from TIP1P/Ice's  $Q_T$  or  $TrQ$  initial values. We initially will consider a Test in which  $Q_T$  is conserved while varying  $Q_{xx}$  by the following constraints.

$$Q'_{yy} = Q_{yy} + \lambda \quad (\text{A.8})$$

$$Q'_{xx} = Q_{xx} - \lambda \quad (\text{A.9})$$

While  $Q_T$  is conserved in this Test,  $TrQ$  is not. In Test 4, seen in Figure A.8, a similar behavior is apparent as we vary the value of  $Q_{xx}$ . Here the  $TrQ$  is not conserved, and we have plotted the same data from Figure A.8 by the  $TrQ$  in Figure A.9. In both graphs, However, the angle  $\phi$  is larger than  $\theta$  at negative values of  $Q_{xx}$  here while  $\theta$  was larger than  $\phi$  when we varied  $Q_{zz}$ . Again no value of  $Q_{xx}$  results in the  $R_{OO}$  separation predicted by the ab initio calculations. The angles also cross over one another as seen previously.

In the next Test, we allow  $Q_{xx}$  to vary as in the previous Test, however we now change  $Q_{zz}$  in such a way to keep the  $TrQ$  constant to it's initial value, as well as varying  $Q_{yy}$  in order to conserve  $Q_T$ . In Figure A.10, we see that the dimer separation distance  $R_{OO}$  peaks at a  $Q_{xx}$  value of about  $-0.1 \text{ \AA}$ , and the angles have the right ordering for which is larger at this value. However, neither the  $R_{OO}$  or the angles are the correct numerical values as predicted by the ab initio calculations. Therefore, we will increase the value of  $\sigma$  to  $3.2668 \text{ \AA}$ , determined by the  $R_{OO}$  distance in Figure A.5. The results of doing so are shown in Figure A.11. Here we see that we have overshot the value of  $R_{OO}$ , and that our range of values of  $Q_{xx}$  is still quite large. Thus in the next Test, shown in Figure A.12, we have adapted a  $\sigma$  value of  $3.2268 \text{ \AA}$ . Here we see that we can accurately achieve the correct ordering of the angles, and approximately the correct value for  $R_{OO}$  at  $Q_{xx}$  values of about  $-0.02 \text{ \AA}$ .

It appears that we have achieved as close to the ab initio predicted values as possible without changing some of our fundamental assumptions. From Figure A.12, I believe that by scaling the quadrupole and dipole by the same constant, thus keeping their ratio the same, we may be able to achieve closer agreement with the ab initio predictions. While Abascal and Vega believe that the largest value of  $Q_T$  that will give reasonable  $T_m$  for ice  $I_h$  to be approximately  $2.56 \text{ \AA}$ , this prediction is made from water models which contain point charges located on the Hydrogens. These charges cause a torque on the other water molecule in the dimer structure, resulting

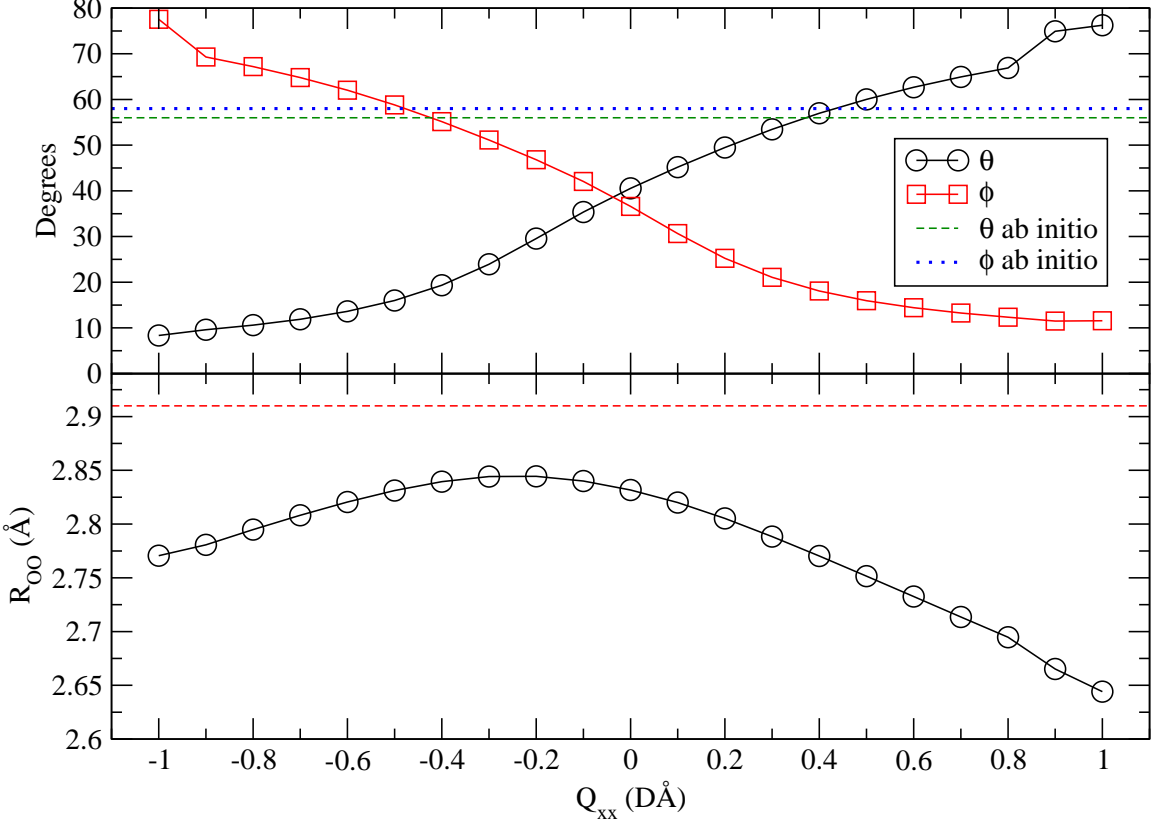


Figure A.8. The  $Q_{xx}$  components of the traced quadrupole tensor were varied while simultaneously adjusting the  $Q_{yy}$  component such that the  $Q_T$  value for the TIP1P/Ice model was held constant. All other parameters were also held constant and equal to the TIP1P/Ice parameters during this test. This means that  $Tr(Q)$  varied since the  $Q_{zz}$  component was not adjusted as  $Q_{xx}$  was varied.

in a change of the magnitude of the angles.

In the following Test,  $Q_{xx}$  was varied while simultaneously varying  $Q_{yy}$  to conserve the value of  $Q_T$ .  $\mu$  was also scaled by  $\mu = 0.996Q_T$  for each  $Q_T$  investigated. The  $TrQ$  was set to 2.365707 D $\text{\AA}$ , and  $\sigma$  was set to 3.2268 Å. In Figure A.13,  $R_{OO}$ ,  $\theta$ , and  $\phi$  are shown as  $Q_{xx}$  and  $Q_{yy}$  are varied.

In the next Test, the dipole moment of the model was varied by some scalar amount ( $\lambda$ ), relative to the  $Q_T$  chosen. The  $Q_{xx}$  component of the quadrupole tensor was set to null, so  $Q_{yy}$  varied for each case of  $Q_T$ .  $Q_{zz}$  was fixed to the TIP1P/Ice

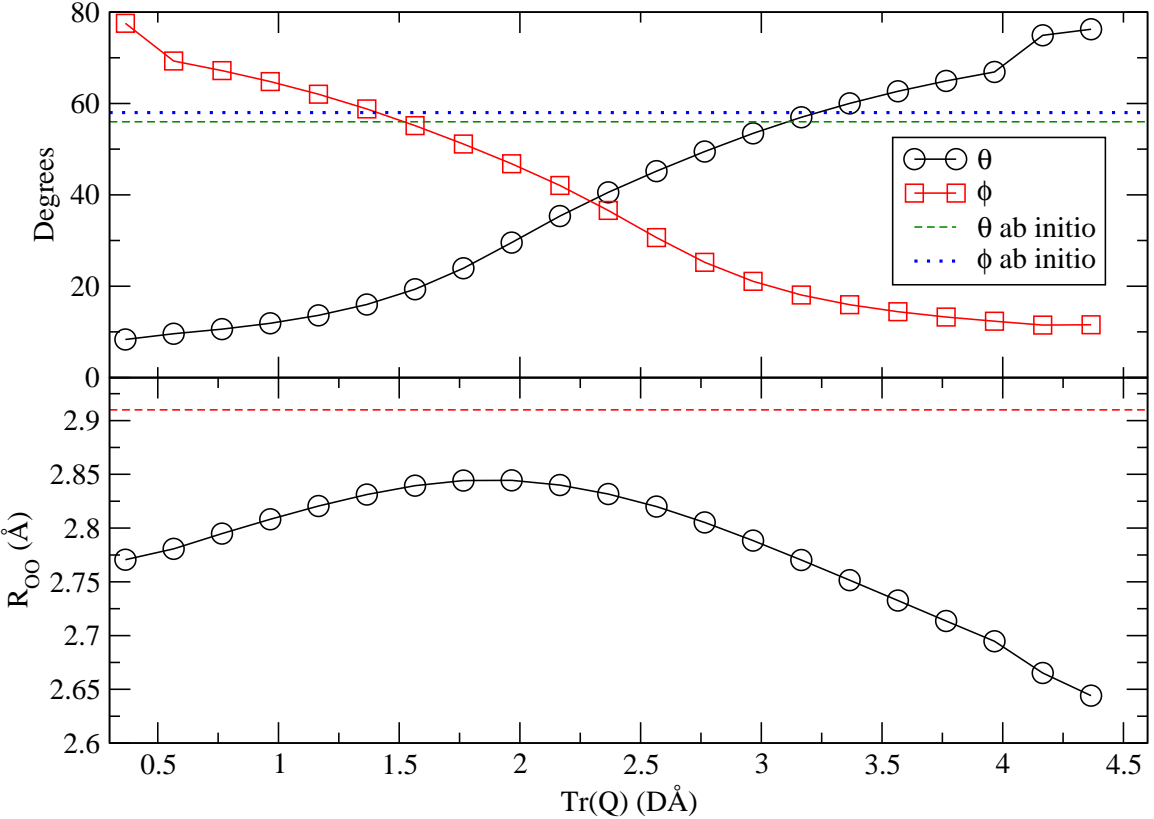


Figure A.9. The same data as plotted in Figure A.8, now plotted as a function of the  $TrQ$ .

model's value. The results of this test can be seen in Figure A.14.

In the next section, I will construct a water model similar to the TIP1P/Ice model, however, it will not be the result of collapsing a many-site model onto a single-site. This model will be derived from the results shown in this section with a larger dipole and quadrupole, in attempts to increase the magnitude of both of the angles without obscuring their ordering or the  $R_{OO}$  values obtained above.

### A.2.2 TIP1P/Ice 2.0

In this section, we will worry less about holding  $Q_T$  constant, and instead hold  $Q_{\bar{B}}$  constant. In Figure A.15, we have the results of varying  $Q_{yy}$  while holding  $Q_{xx}$

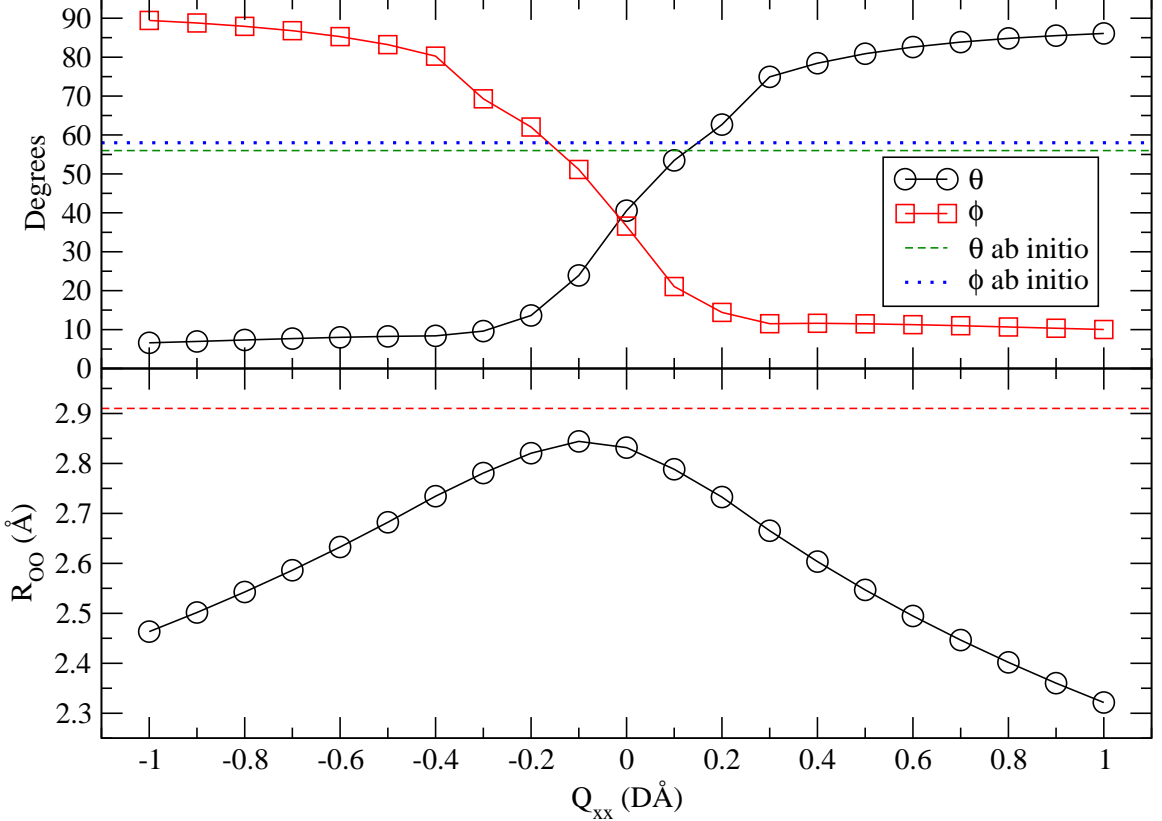


Figure A.10. The  $Q_{xx}$  components of the traced quadrupole tensor were varied while simultaneously adjusting the  $Q_{yy}$  component such that the  $Q_T$  value for the TIP1P/Ice model was held constant. The  $Q_{zz}$  component of the quadrupole tensor was also varied in such a way as to keep the  $Tr(Q)$  held constant to the TIP1P/Ice value. We see here that the angles cross over one another as in Figure A.8.

constant at  $0.1 \text{ D}\text{\AA}$ , and varying  $Q_{zz}$  such that  $Q\bar{\alpha}$  fixed at the TIP4P/Ice value. However, we see that we do not recover the TIP4P/Ice water dimer geometry.

It is interesting to note that the value of  $\phi$  in Figure A.15 is much greater than initially expected from Figure A.8. There, we would predict  $\phi \approx 40$  degrees, while here we have obtained a value of about 76 degrees. Also, there does not appear to be any appreciable change in the values of  $\theta$  as we vary  $Q_{yy}$ . This makes me wonder what controls the value of  $\theta$ , as it appears to not be the value of  $Q_{yy}$  as initially thought. In Figure A.16, we have held  $Q_{yy}$  constant at  $-0.1 \text{ D}\text{\AA}$ , and varied  $Q_{xx}$  to

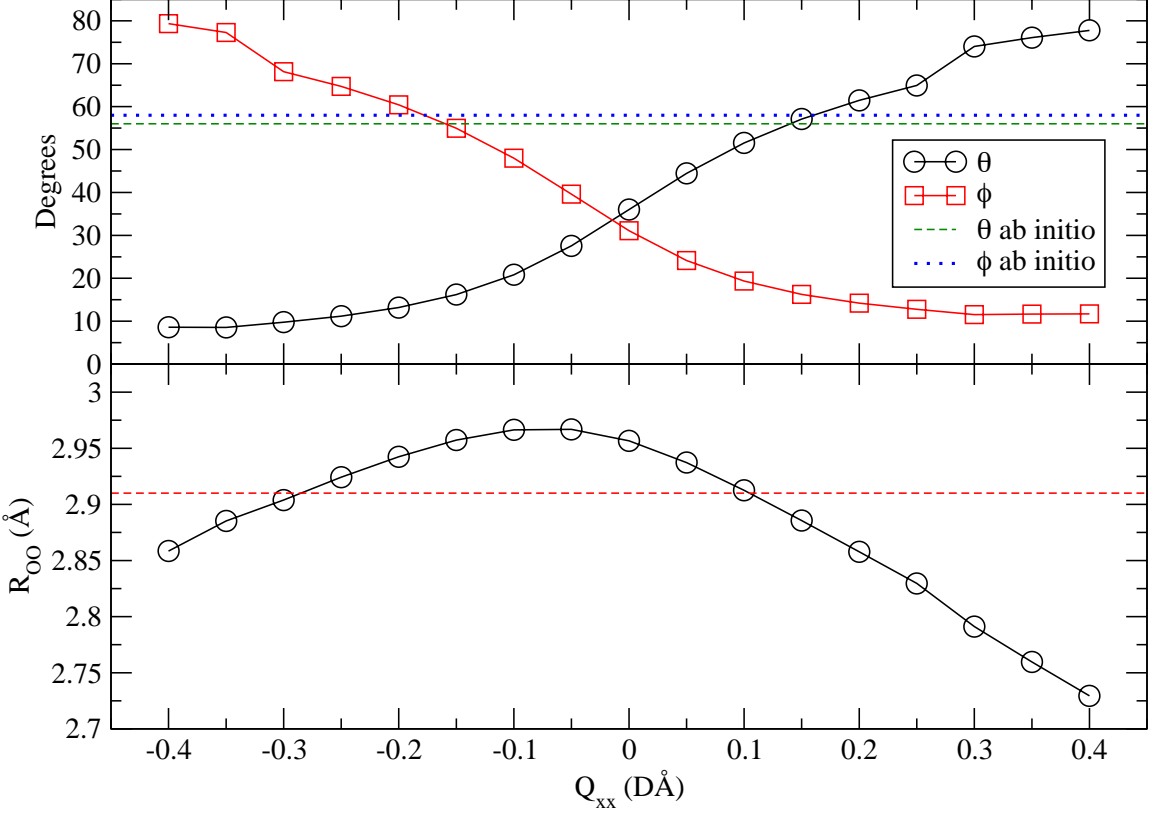


Figure A.11. Setting  $\sigma$  to  $3.2668 \text{ \AA}$ , vary  $Q_{xx}$  while simultaneously adjusting  $Q_{yy}$  and  $Q_{zz}$  to conserve  $Q_T$  and  $TrQ$ .

see if it controls both  $\phi$  and  $\theta$ .

From Figure A.16, we see that while  $R_{OO}$  is slightly sensitive to the value of  $Q_{xx}$ , the angles  $\theta$  and  $\phi$  are both insensitive to it. In order to try and understand if and how the angles are dependent on  $Q_{xx}$ , I have re-plotted the data from Figure A.10 as a function of  $Q_{xx}$ . This can be seen in Figure A.17.

An interesting follow up test will be to set  $Q_{xx}$  and  $Q_{yy}$  to -0.1,  $Q_{zz}$  to 1.3071, and vary  $\mu$  to see if the desired angles can be achieved with a smaller dipole moment. The results of doing so are shown in Figure A.18.

In Figure A.18, we see that as we decrease the value of the dipole moment, the water dimer's separation distance,  $R_{OO}$  gradually becomes larger. The angle

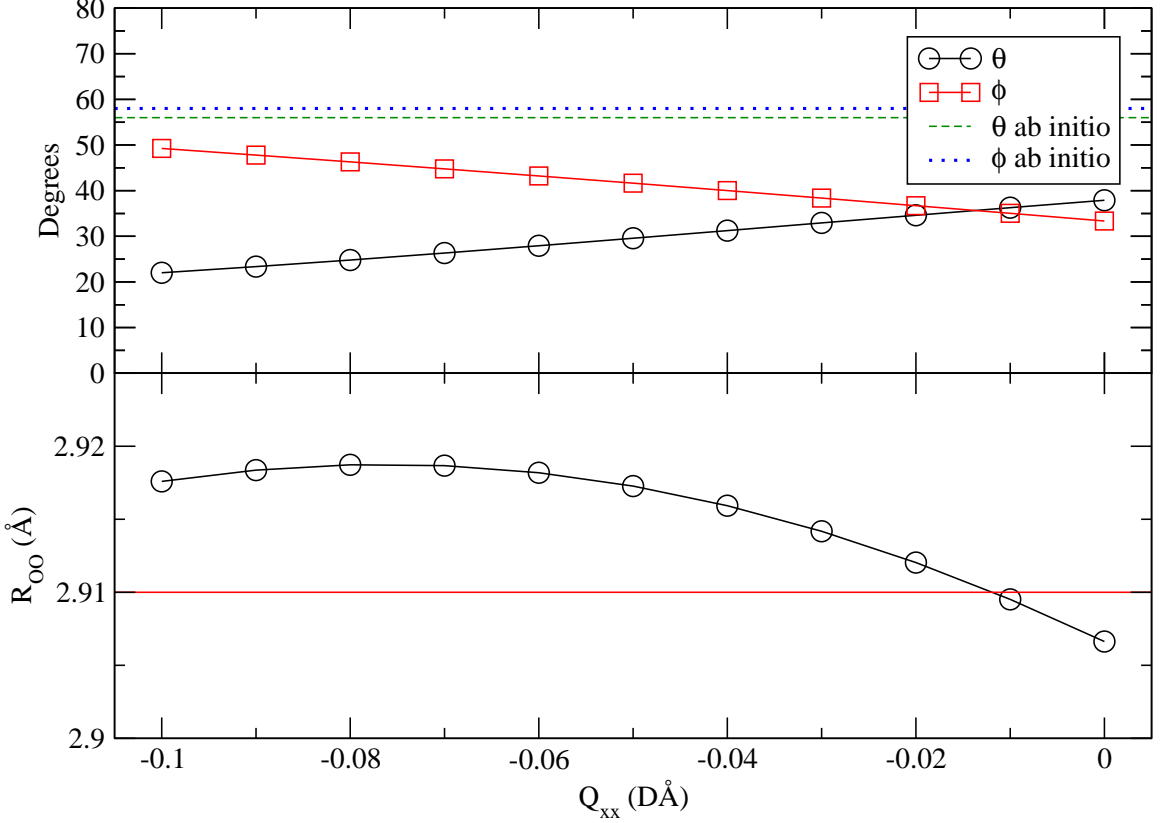


Figure A.12. Setting  $\sigma$  to  $3.2268 \text{\AA}$ , vary  $Q_{xx}$  while simultaneously adjusting  $Q_{yy}$  and  $Q_{zz}$  to conserve  $Q_T$  and  $TrQ$ .

$\phi$  increases slightly with decreasing  $\mu$ , however,  $\theta$  is relatively insensitive to the value of  $\mu$ .

In the next Test, we have set the Lennard-Jones parameters to that of the TIP4P/Ice model, as well as the  $Q_{xx}$  and  $Q_{zz}$  values.  $Q_{yy}$  is allowed to vary, and as such,  $Q_T$  and  $Q_{\bar{T}}$  both vary. In Figure A.19, we see that the angle  $\theta$  is obtained when  $Q_{yy}$  is set to about  $1.87 \text{ D}\text{\AA}$ . However, we see that we miss the dimer separation distance at this value of  $Q_{yy}$ , as well as the angle  $\phi$ , which we believe to be the less important of the two angles.

In a similar way, we have held  $Q_{yy}$  and  $Q_{zz}$  constant while varying  $Q_{xx}$ . The results of doing so can be seen in Figure A.20.

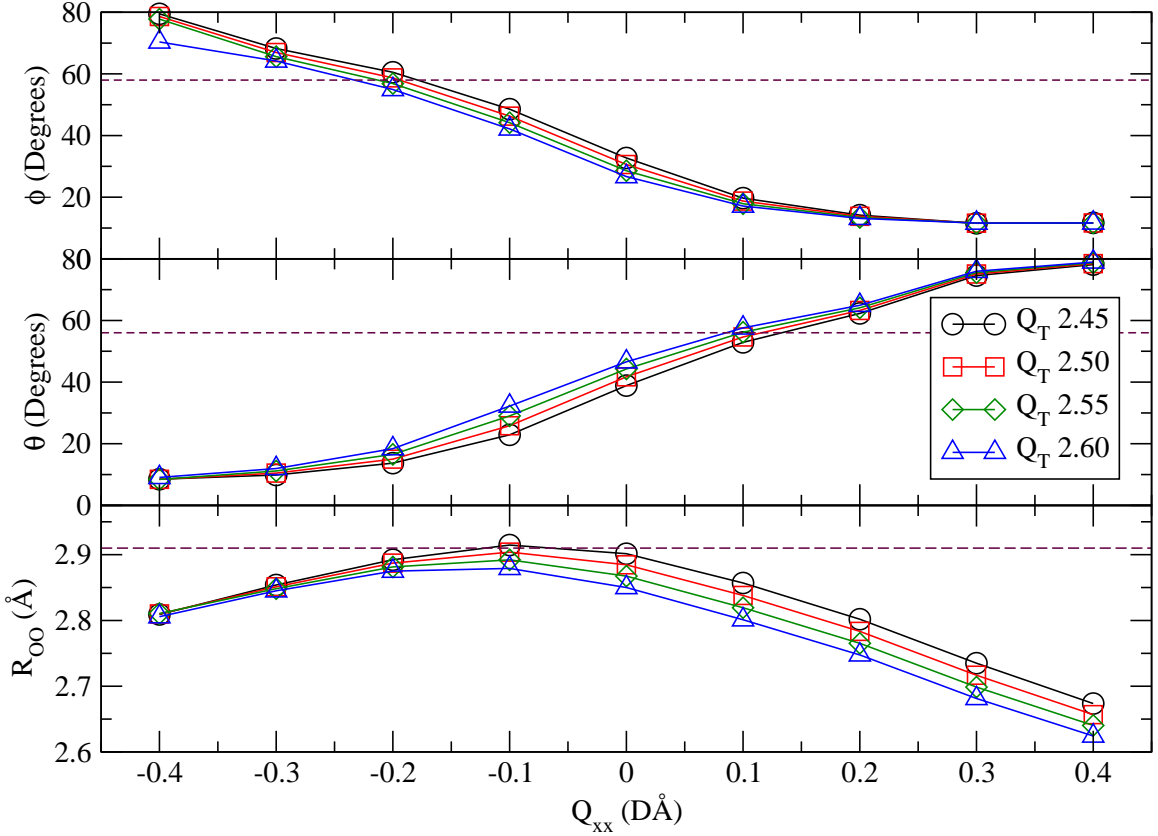


Figure A.13. Here  $Q_{xx}$  and  $Q_{yy}$  are varied simultaneously to conserve the value of  $Q_T$ .  $\mu$  is scaled as  $0.996Q_T$ , thus the ratio of  $\mu$  to  $Q_T$  is conserved for each Test of  $Q_T$ . The  $TrQ$  is fixed to a set value, thus  $Q_{zz}$  varies as the other components do.

Finally, we have finished the permutation by varying  $Q_{zz}$  while holding  $Q_{xx}$  and  $Q_{yy}$  constant at their original TIP4P/Ice values, as seen in Figure A.21.

### A.2.3 Bulk Properties

As an initial test of the bulk phase properties, I have equilibrated two separate water boxes, one containing 1372 molecules, and one containing 4000 molecules. The resulting geometry was a cubic box with side length of  $48.57617 \text{ \AA}$ . The molecules were propagated at 300K for 1 nanosecond, saving coordinates every 0.1 ps for analysis. The three-dimensional diffusion constant was found to be  $5.488 \times 10^{-5} \text{ cm}^2 \text{s}^{-1}$ . This

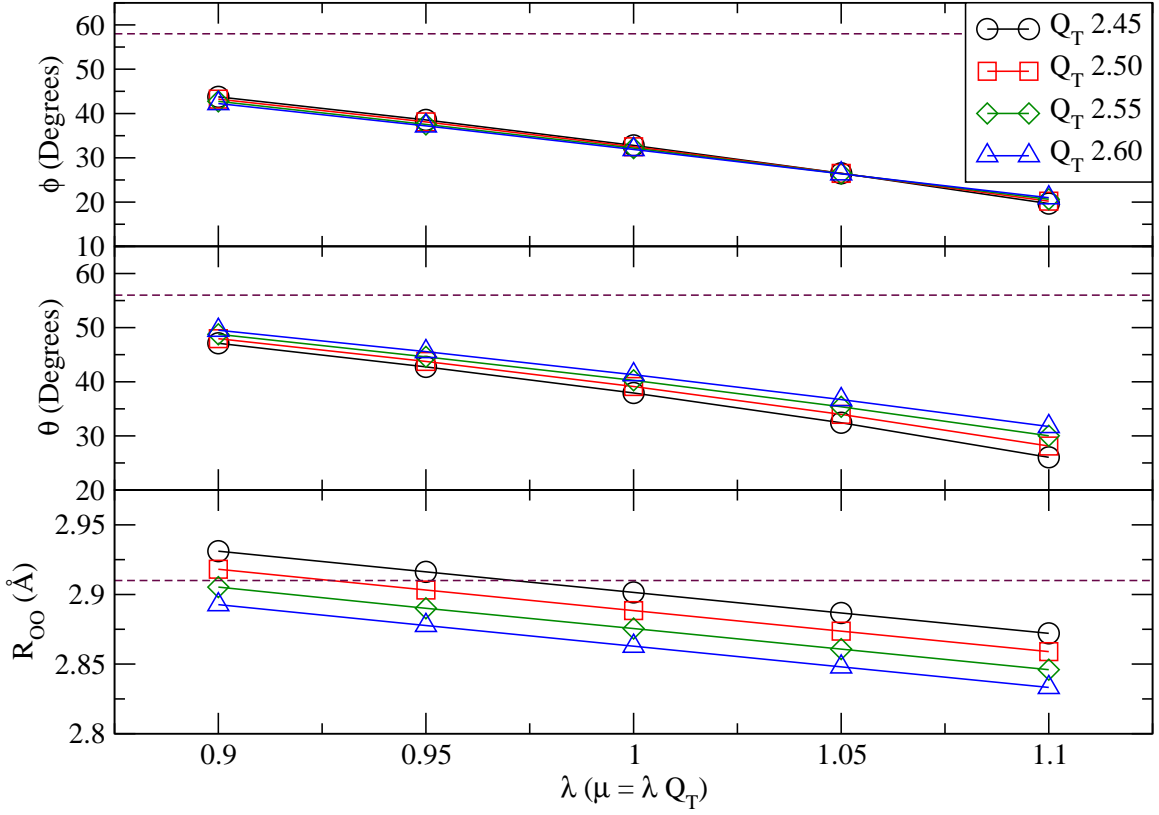


Figure A.14.

is about a factor of two larger than the experimentally reported value of  $2.30 \text{ cm}^2 \text{s}^{-1}$ . We attribute this difference to a lack of strength of hydrogen bonding. Due to this, we will try playing with the dipole strength and the  $Q_{zz}$  values.

#### A.2.4 Basal Ice $I_h$ /water Coexistence

In order to tune the model to the desired observable, I have begun testing the model at the ice  $I_h$ /water interface, exposing a basal plane to bulk water. This system was prepared by constructing a large block of ice from crystallographic coordinates taken from Hirsch and Ojamae structure number 6? . The constructed block is periodic in all three dimensions. The block was positioned in a simulation cell such that the basal face pointed along the positive  $z$ -dimension. The ice block was allowed

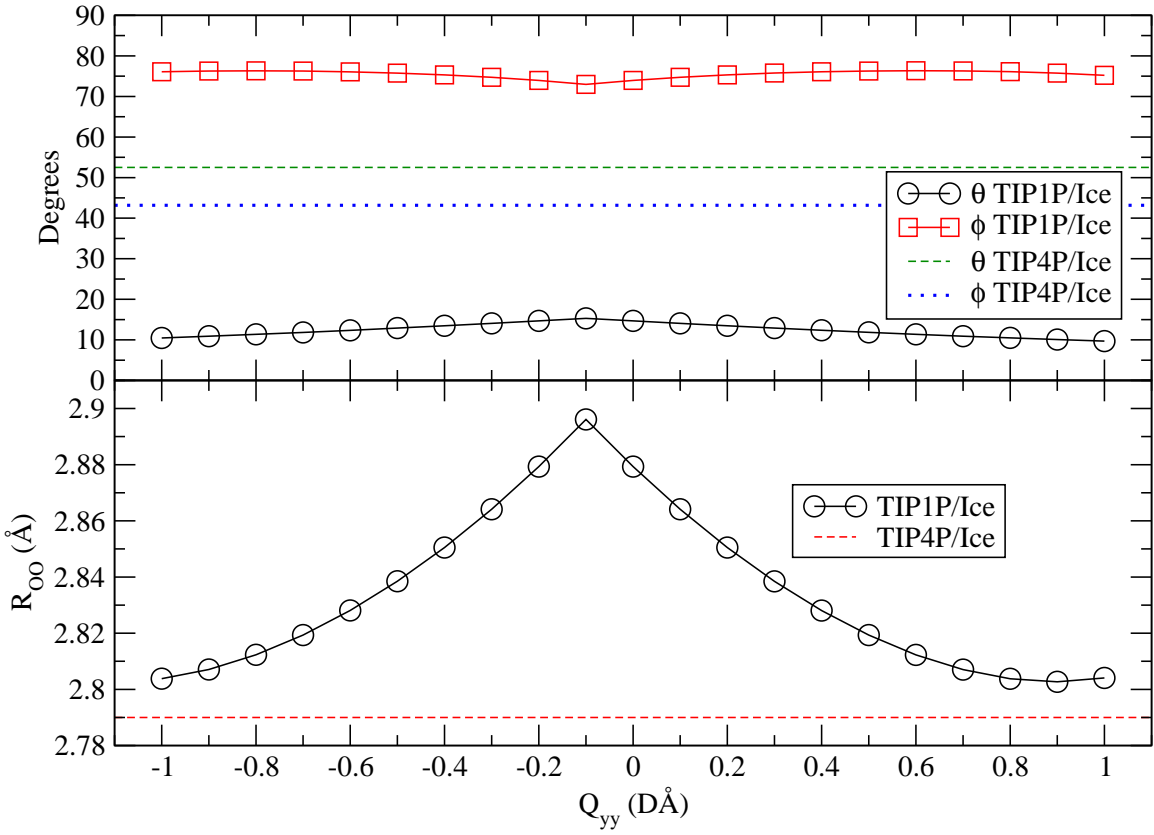


Figure A.15.  $Q_{xx} = -0.1$ , QBar set to the TIP4P/Ice QBar value of 2.8141,  $Q_{zz}$  was modified to keep this constant as  $Q_{yy}$  changed.

to relax and equilibrated to 75 K. Separately, a simulation box of liquid water with a density of  $0.999 \text{ g cm}^{-3}$  was equilibrated to 75 K, with equivalent  $x$  and  $y$  dimensions to the ice block, and twice that in  $z$ . The ice block was then merged with the liquid system by carving out any liquid water molecule within three angstroms of a molecule from the ice system.

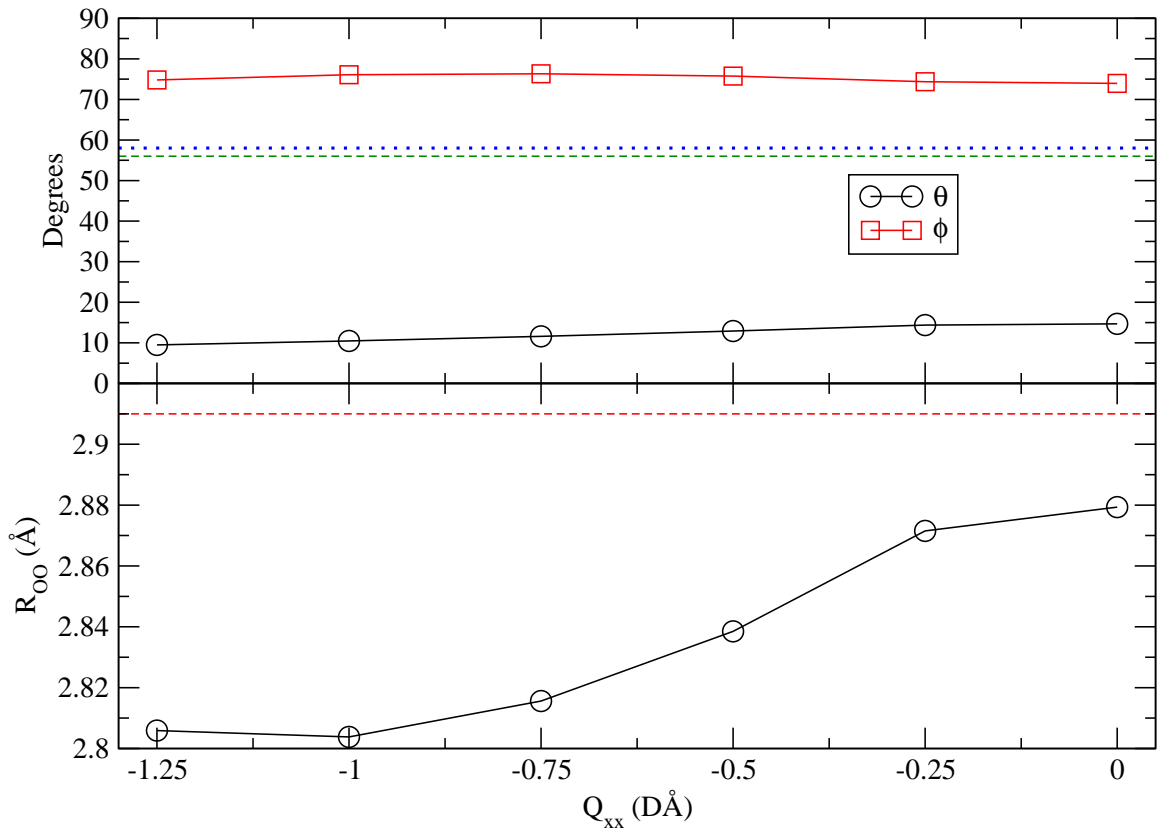


Figure A.16.  $Q_{yy} = -0.1$ ,  $Q_{zz}$  was varied to keep  $Q\bar{a}$  constant and equal to the TIP4P/Ice model's value of 2.8141.

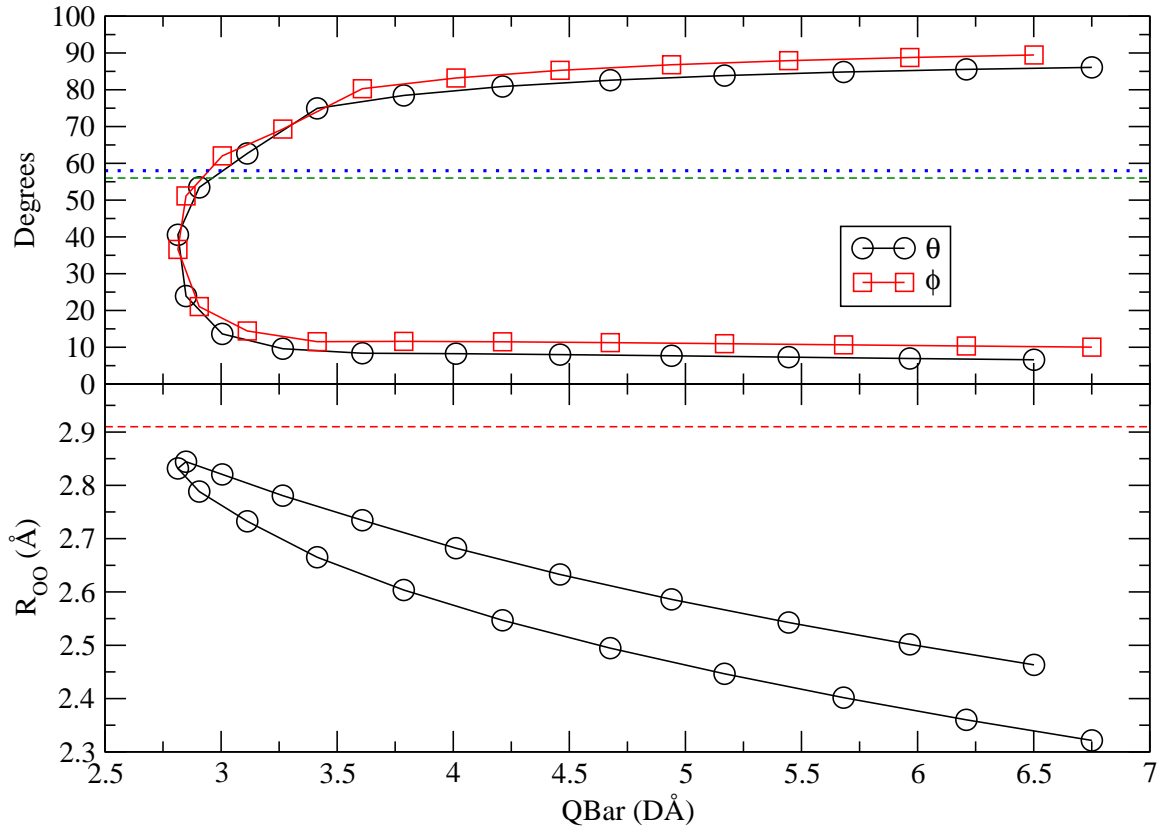


Figure A.17.  $Q_{xx}$  and  $Q_{yy}$  varied while holding  $Q_T$  constant,  $Q_{zz}$  varied in order to keep  $TrQ$  constant. Both  $Q_T$  and  $TrQ$  were set to the TIP4P/Ice model value.

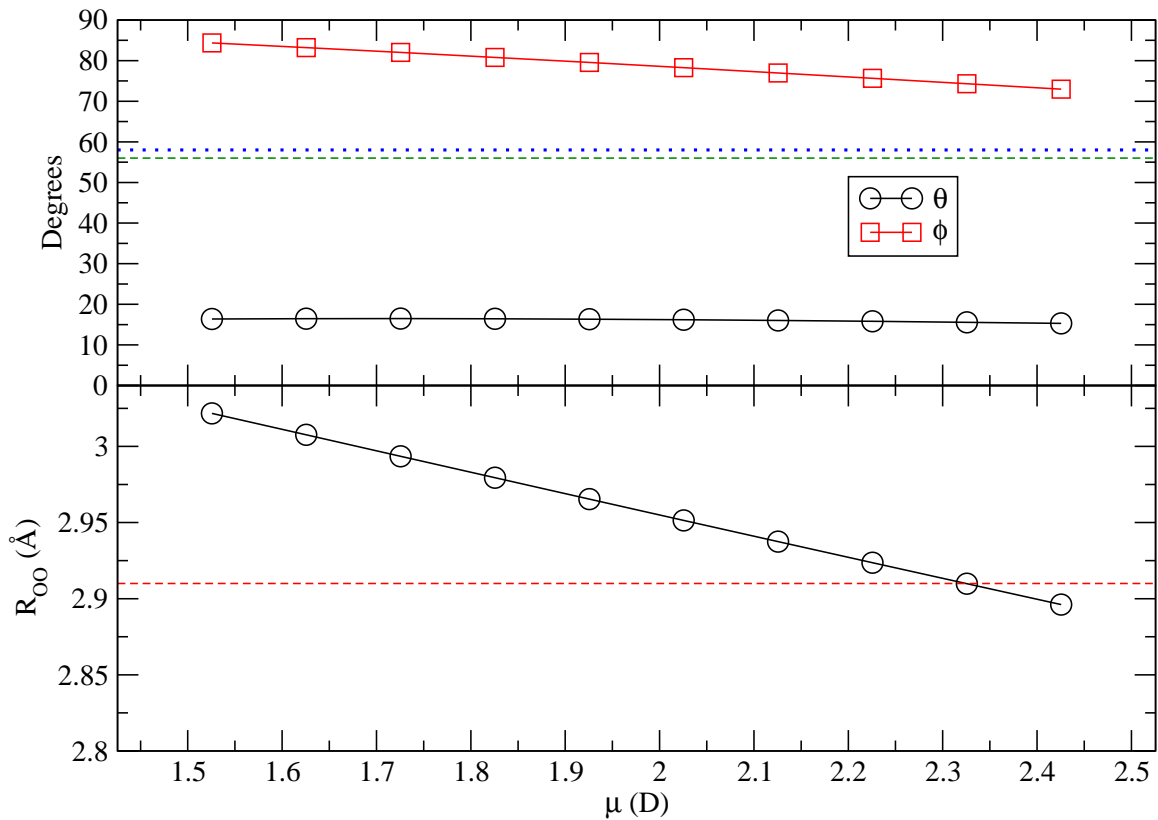


Figure A.18.  $Q_{xx} = -0.1$ ,  $Q_{yy} = -0.1$ ,  $Q_{zz} = 1.3701$  which ensures QBar is set to the TIP4P/Ice model value of  $2.8141 \text{ \AA}$ .

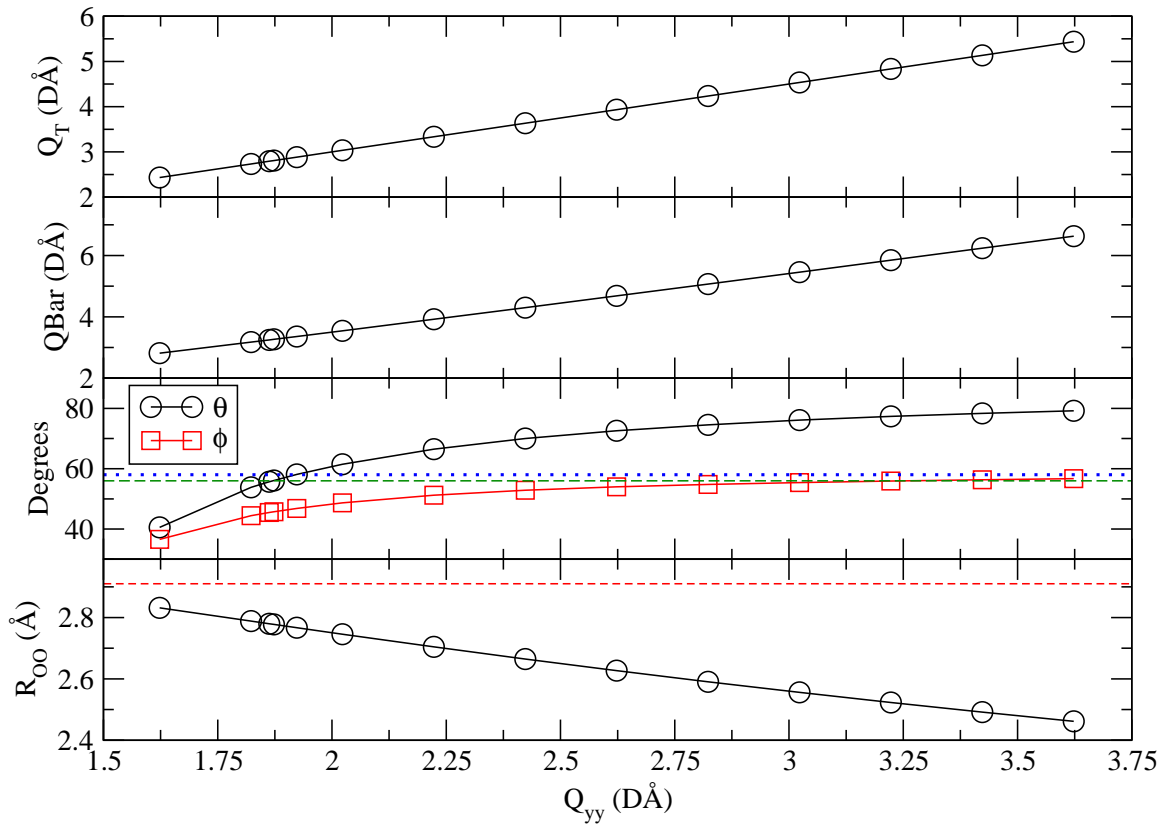


Figure A.19.  $Q_{xx}$  and  $Q_{zz}$  are set to the TIP4P/Ice value, as well as the Lennard-Jones parameters. The left most data point is the parameter set of the TIP4P/Ice model.

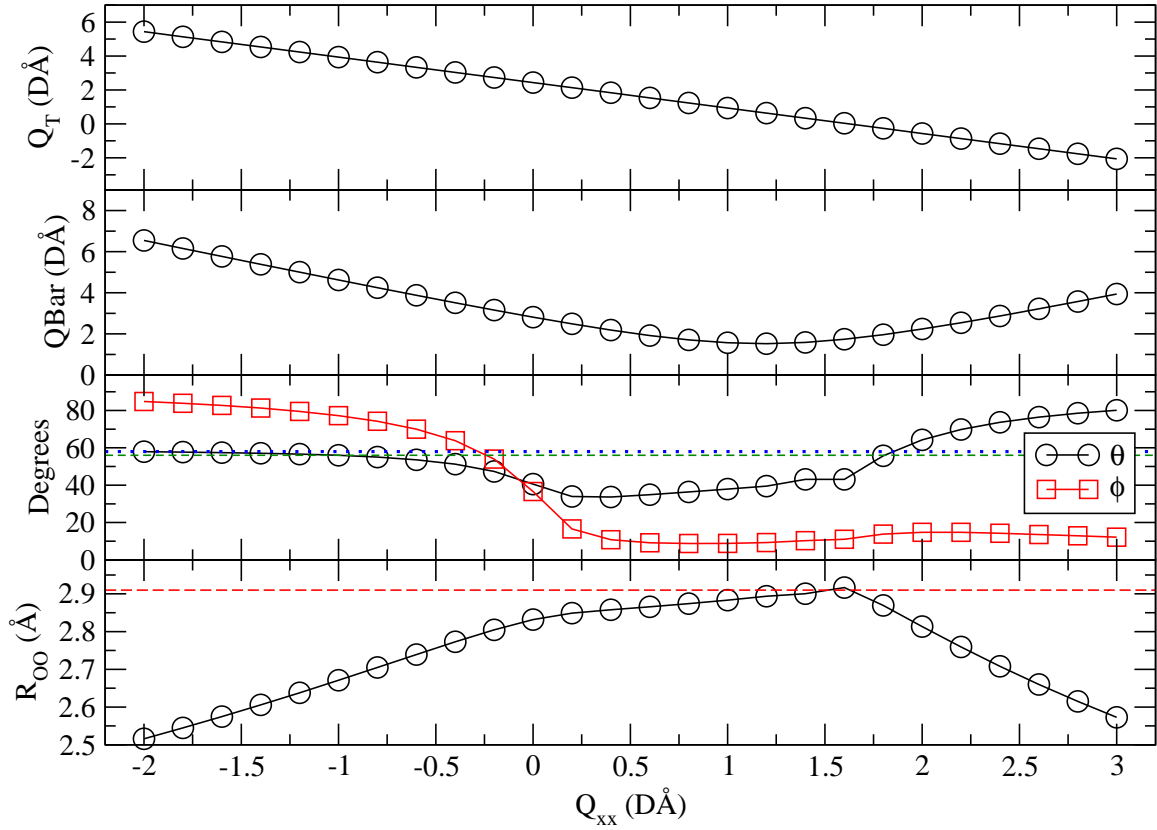


Figure A.20.  $Q_{yy}$  and  $Q_{zz}$  are set to the TIP4P/Ice value, as well as the Lennard-Jones parameters. The left most data point is the parameter set of the TIP4P/Ice model.

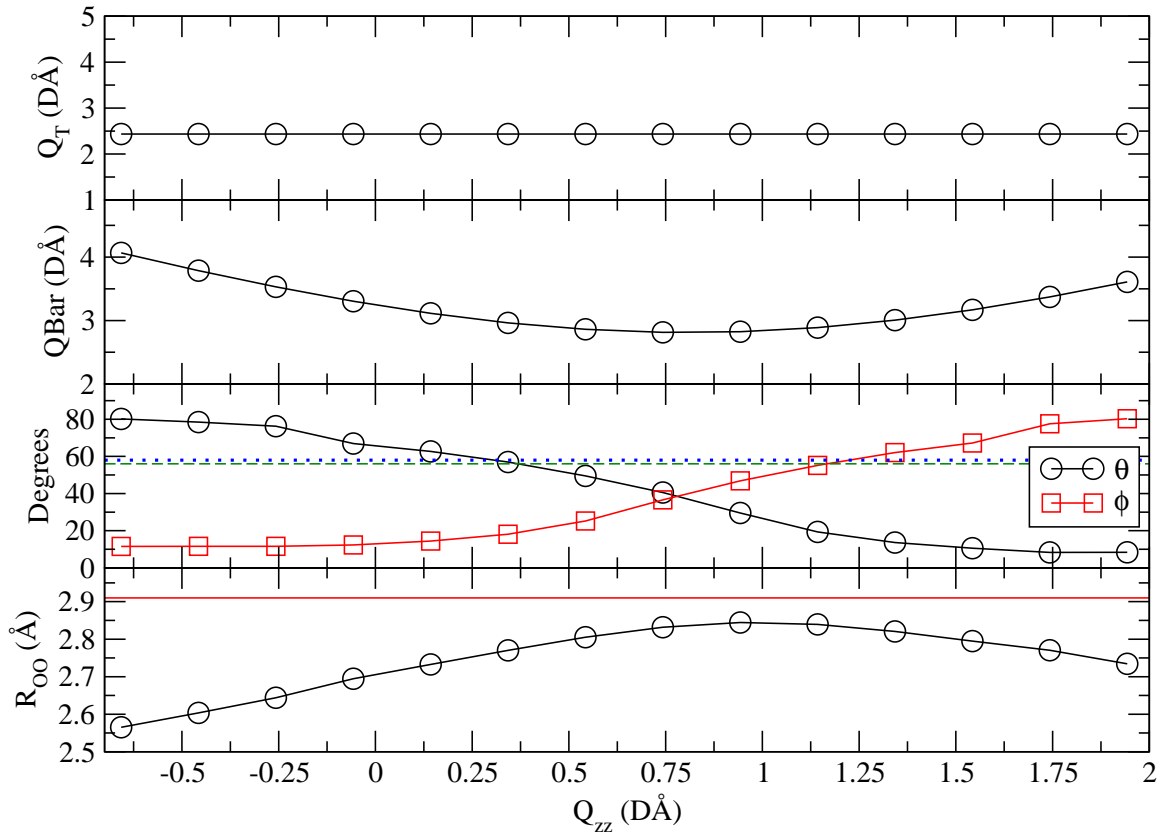


Figure A.21.  $Q_{xx}$  and  $Q_{yy}$  are set to the TIP4P/Ice value, as well as the Lennard-Jones parameters. The left most data point is the parameter set of the TIP4P/Ice model.

## BIBLIOGRAPHY

1. Bowden, F. P.; Hughes, T. P. *P. R. Soc. A* **1939**, *172*, 280–298.
2. Evans, D.; Nye, J.; Cheeseman, K. *Proc. R. Soc. Lond. A* **1976**, *347*, 493–512.
3. Roberts, A. D.; Richardson, J. C. *Wear* **1981**, *67*, 55–69.
4. Derjaguin, B. V. *Wear* **1988**, *128*, 19–27.
5. Liang, H.; Martin, J. M.; Mogne, T. L. *Acta Mater.* **2003**, *51*, 2639–2646.
6. Higgins, D. D.; Marmo, B. A.; Jeffree, C. E.; Koutsos, V.; Blackford, J. R. *Wear* **2008**, *265*, 634–644.
7. Oksanen, P.; Keinonen, J. *Wear* **1982**, *78*, 315–324.
8. Buhl, D.; Fauve, M.; Rhyner, H. *Cold Reg. Sci. Technol.* **2001**, *33*, 133–140.
9. Bäurle, L.; Szabó, D.; Fauve, M.; Rhyner, H.; Spencer, N. D. *Tribol. Lett.* **2006**, *24*, 77–84.
10. Bäurle, L.; Kaempfer, T. U.; Szabó, D.; Spencer, N. D. *Cold Reg. Sci. Technol.* **2007**, *47*, 276–289.
11. Calabrese, S. *Lubr. Eng.* **1980**, *36*, 283.
12. Kietzig, A. M.; Hatzikiriakos, S. G.; Englezos, P. *J. Appl. Phys.* **2009**, *106*, 024303.
13. Liang, H.; Martin, J. M.; Le Mogne, T. *J. Appl. Phys.* **2005**, *97*, 043525.
14. Kietzig, A. M.; Hatzikiriakos, S. G.; Englezos, P. *J. Appl. Phys.* **2010**, *107*, 081101.
15. Kennedy, F. E.; Schulson, E. M.; Jones, D. E. *Philos. Mag. A* **2000**, *80*, 1093–1110.
16. Maeno, N.; Arakawa, M. *J. Appl. Phys.* **2004**, *95*, 134–139.
17. Fortt, A.; Schulson, E. *Acta Mater.* **2007**, *55*, 2253–2264.
18. Fortt, A. L.; Schulson, E. M. *J. Geophys. Res.-Oceans* **2011**, *116*, 1–13.

19. Lishman, B.; Sammonds, P.; Feltham, D. *J. Geophys. Res.-Oceans* **2011**, *116*, 1–13.
20. Samadashvili, N.; Reischl, B.; Hynninen, T.; Ala-Nissilä, T.; Foster, A. S. *Friction* **2013**, *1*, 242–251.
21. Kroes, G. J. *Surf. Sci.* **1992**, *275*, 365–382.
22. Ikeda-Fukazawa, T.; Kawamura, K. *J. Chem. Phys.* **2004**, *120*, 1395–1401.
23. Picaud, S. *J. Chem. Phys.* **2006**, *125*, 174712.
24. Conde, M. M.; Vega, C.; Patrykiejew, A. *J. Chem. Phys.* **2008**, *129*, 014702.
25. Bartels-Rausch, T. et al. *Atmos. Chem. Phys.* **2014**, *14*, 1587–1633.
26. Sánchez, M. A. et al. *Proc. Natl. Acad. Sci. U.S.A.* **2017**, *114*, 227–232.
27. Pfalzgraff, W.; Neshyba, S.; Roeselova, M. *J. Phys. Chem. A* **2011**, *115*, 6184–6193.
28. Dash, J. G.; Fu, H.; Wetzlaufer, J. S. *Rep. Prog. Phys.* **1995**, *58*, 115–167.
29. Rosenberg, R. *Phys. Today* **2005**, *58*, 50–55.
30. Dash, J. G.; Rempel, A. W.; Wetzlaufer, J. S. *Rev. Mod. Phys.* **2006**, *78*, 695–741.
31. Malenkov, G. *J. Phys.-Condensed Matter* **2009**, *21*, 283101.
32. Bhushan, B. *Introduction to Tribology*; John Wiley & Sons: New York, 2002.
33. Persson, B. N. J. *J. Chem. Phys.* **2015**, *143*, 224701.
34. Tuononen, A. J.; Kriston, A.; Persson, B.; Tuononen, A. J.; Kriston, A.; Persson, B. *J. Chem. Phys.* **2016**, *145*, 114703.
35. Louden, P.; Schoenborn, R.; Lawrence, C. P. *Fluid Phase Equilibr.* **2013**, *349*, 83–86.
36. Buch, V.; Groenzin, H.; Li, I.; Shultz, M. J.; Tosatti, E. *Proc. Natl. Acad. Sci. U.S.A.* **2008**, *105*, 5969–5974.
37. Groenzin, H.; Li, I.; Buch, V.; Shultz, M. J. *J. Chem. Phys.* **2007**, *127*, 214502.
38. Hirsch, T. K.; Ojamäe, L. *J. Phys. Chem. B* **2004**, *108*, 15856–15864.
39. Bryk, T.; Haymet, A. D. J. *J. Chem. Phys.* **2002**, *117*, 10258–10268.
40. Berendsen, H. J. C.; Grigera, J. R.; Straatsma, T. P. *J. Phys. Chem.* **1987**, *91*, 6269–6271.
41. Arbuckle, B. W.; Clancy, P. *J. Chem. Phys.* **2002**, *116*, 5090–5098.

42. Kuang, S.; Gezelter, J. D. *Mol. Phys.* **2012**, *110*, 691–701.
43. Báez, L. A.; Clancy, P. *J. Chem. Phys.* **1995**, *103*, 9744–9755.
44. Bryk, T.; Haymet, A. D. *J. Mol. Simulat.* **2004**, *30*, 131–135.
45. Sanz, E.; Vega, C.; Abascal, J. L. F.; MacDowell, L. G. *Phys. Rev. Lett.* **2004**, *92*, 255701.
46. Fennell, C. J.; Gezelter, J. D. *J. Chem. Theory Comput.* **2005**, *1*, 662–667.
47. Gay, S. C.; Smith, E. J.; Haymet, A. D. J. *J. Chem. Phys.* **2002**, *116*, 8876–8880.
48. García Fernández, R.; Abascal, J. L. F.; Vega, C. *J. Chem. Phys.* **2006**, *124*, 144506.
49. Abascal, J. L. F.; García Fernández, R.; MacDowell, L. G.; Sanz, E.; Vega, C. *J. Mol. Liq.* **2007**, *136*, 214–220.
50. Vrbka, L.; Jungwirth, P. *J. Mol. Liq.* **2007**, *134*, 64–70.
51. Meineke, M. A.; Vardeman, C. F.; Lin, T.; Fennell, C. J.; Gezelter, J. D. *J. Comput. Chem.* **2005**, *26*, 252–271.
52. Gezelter, J. D. et al. OpenMD, an Open Source Engine for Molecular Dynamics. 2016; <http://openmd.org>.
53. Fennell, C. J.; Gezelter, J. D. *J. Chem. Phys.* **2006**, *124*, 234104.
54. Karim, O. A.; Haymet, A. D. J. *J. Chem. Phys.* **1988**, *89*, 6889–6896.
55. Karim, O. A.; Kay, P. A.; Haymet, A. D. J. *J. Chem. Phys.* **1990**, *92*, 4634.
56. Hayward, J. A.; Haymet, A. D. J. *J. Chem. Phys.* **2001**, *114*, 3713–3726.
57. Hayward, J. A.; Haymet, A. D. J. *Phys. Chem. Chem. Phys.* **2002**, *4*, 3712–3719.
58. Chau, P.-L.; Hardwick, A. J. *Mol. Phys.* **1998**, *93*, 511–518.
59. Errington, J.; Debenedetti, P. *Nature* **2001**, *409*, 318–321.
60. Kumar, P.; Buldyrev, S. V.; Stanley, H. E. *Proc. Natl. Acad. Sci. U.S.A.* **2009**, *106*, 22130–22134.
61. Balasubramanian, S.; Mundy, C. J. *Bull. Mater. Sci.* **1999**, *22*, 873–876.
62. Laage, D.; Hynes, J. T. *Science* **2006**, *311*, 832–835.
63. Laage, D.; Hynes, J. T. *J. Phys. Chem. B* **2008**, *112*, 14230–14242.
64. Laage, D.; Hynes, J. T. *Proc. Natl. Acad. Sci. U.S.A.* **2007**, *104*, 11167–11172.

65. Laage, D.; Hynes, J. T. *J. Phys. Chem. B* **2008**, *112*, 7697–7701.
66. Stirnemann, G.; Sterpone, F.; Laage, D. *J. Phys. Chem. B* **2011**, *115*, 3254–3262.
67. Laage, D.; Stirnemann, G.; Sterpone, F.; Rey, R.; Hynes, J. T. *Annu. Rev. Phys. Chem.* **2011**, *62*, 395–416.
68. Duboué-Dijon, E.; Laage, D. *J. Chem. Phys.* **2014**, *141*, 22D529.
69. Laage, D.; Thompson, W. H. *J. Chem. Phys.* **2012**, *136*, 044513.
70. Fogarty, A. C.; Coudert, F. X.; Boutin, A.; Laage, D. *Chem. Phys. Chem.* **2014**, *15*, 521–529.
71. Laage, D.; Hynes, J. T. *Chem. Phys. Lett.* **2006**, *433*, 80–85.
72. Luzar, A.; Chandler, D. *Nature* **1996**, *379*, 55.
73. Beaglehole, D.; Wilson, P. *J. Phys. Chem.* **1993**, *97*, 11053–11055.